Journal of the Mississippi
Academy of Sciences

Volume 67, Number 1 January, 2022

Special Edition
Physics, Engineering & Technology

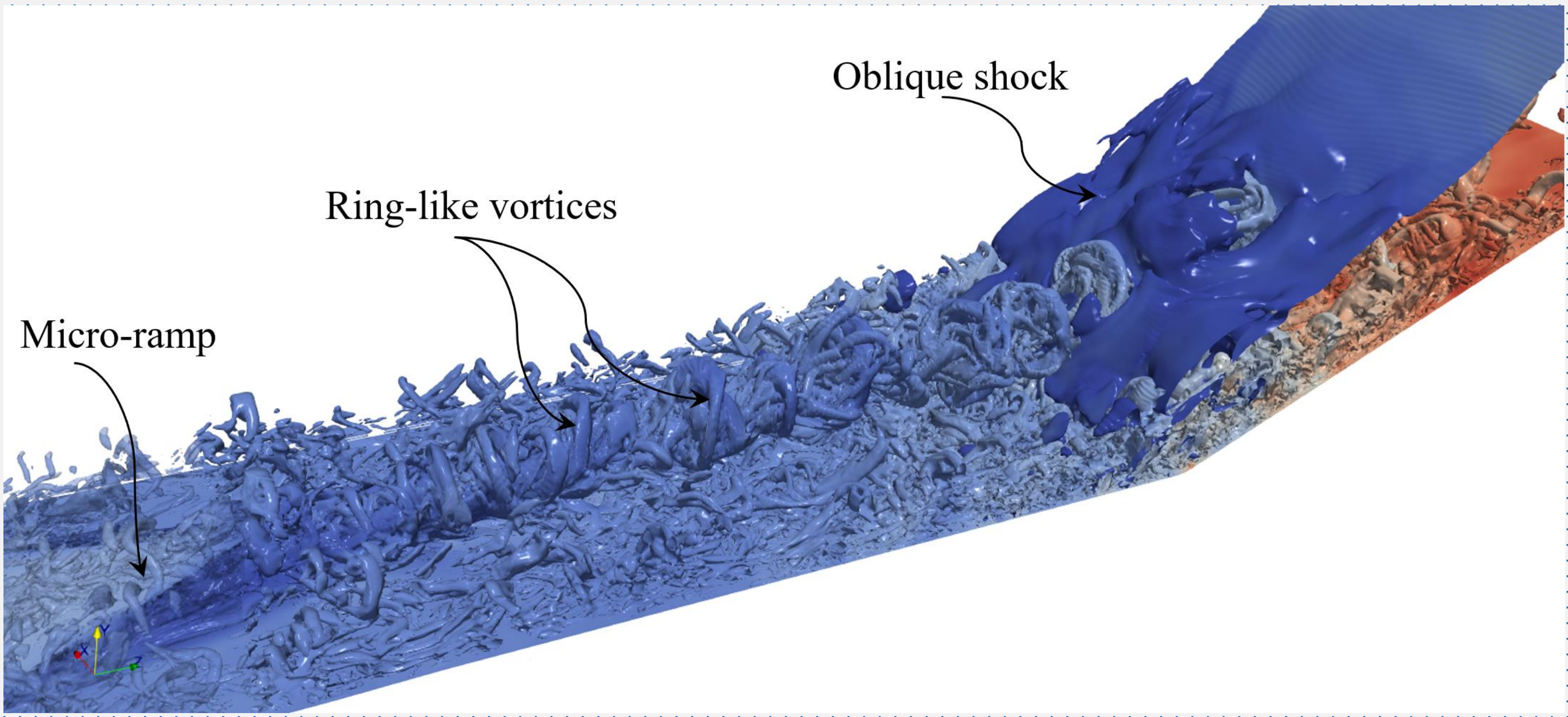

Guest Editors:
Dr. Pradip Biswas (Tougaloo College) and Dr. Shanti Bhushan (Mississippi State University)

Journal of the Mississippi Academy of Sciences
ISSN 0076-9436

Editorial policy:
General. The Editorial Board publishes articles on all aspects of science that are of general interest to the Mississippi scientific community. General articles include short reviews of general interest, reports of recent advances in a particular area of science, current events of interest to researchers and science educators, etc. Research papers of sufficiently broad scope to be of interest to many Academy members are also considered. Articles of particular interest in Mississippi are especially encouraged. Research papers are reports of original research. Descriptions of laboratory or field exercises suitable for high school or college teaching laboratories are accepted. Brief communications not exceeding two pages are accepted. Submission of any manuscript implies that the paper has not been published and is not being considered for publication elsewhere.
Copyright. Copyright protection is secured automatically for contributing authors through publication of this journal. The Board of the Mississippi Academy of Sciences recognizes ownership of this published material belongs solely to the author(s) of individual articles.
Review. All papers submitted for publication will be peer-reviewed. You are encouraged to have one or more of your colleagues review the manuscript before submitting it for formal review.
Proofs and reprints. When a manuscript is accepted for publication the author of correspondence will receive a PDF file in lieu of reprints.
Page charges. Authors or their institutions must pay page charges of $150.00 for manuscript. For individuals that can not pay for their manuscript please let us know in advance and we will work to help to find a sponsor.
Letters policy. We welcome reader's opinions and comments about the journal and about science in general. Send you letters to the editor. Include full name, address, and daytime telephone number. Letters may be edited.

All correspondence concerning publication should be directed to:

Dr. Michelle Tucci
Mississippi Academy of Sciences
Post Office Box 55907
Jackson, MS 39296-5907

msacademyofscience@comcast.net
601-366-2995

Administrative policy:
Membership. Membership is open to anyone interested in science in Mississippi. The basic annual membership fee is $50; students may join for $20. Information about other membership categories is available through the MAS office.
Advertising. The Journal of the Mississippi Academy of Sciences accepts paid advertising. Contact the editor or the MAS Office for current rates.

Direct correspondence concerning administration of the Mississippi Academy of Sciences and its journal to:

Dr. Michelle Tucci
Mississippi Academy of Sciences
Post Office Box 55907
Jackson, MS 39296-5907

msacademyofscience@gmail.com
601-366-2995
The Mississippi Academy of Sciences operates a web site: http://www.msacad.org/

On the cover: Interaction of ring-like vortices generated by a micro-ramp with oblique shock generated from a ramp corner for supersonic inflow at Mach number 2.5. The figure is from the paper "Aeroelastic Flutter Control using Micro-Vortex Generators" Zope et al. in this special issue. The figure was generated by the co-author Dr. Yonghua Yan @ Jackson State University using his LES solver. The simulations were performed on Mississippi State University HPC system Shadow.

Journal of the Mississippi Academy of Sciences

Volume 67 January 2022 Number 1

The Journal of the Mississippi Academy of Sciences (ISSN 0076-9436) is published in January (annual meeting abstracts), April, July, and October, by the Mississippi Academy of Sciences. Members of the Academy receive the journal as part of their regular (nonstudent) membership. Inquiries regarding subscriptions, availability of back issues, and address changes should be addressed to The Mississippi Academy of Sciences, Post Office Box 55709, Jackson, MS 39296-5709, telephone 601-977-0627, or email msacademyofscience@comcast.net.

TABLE OF CONTENTS

Research Articles

Departments

Aeroelastic Flutter Control using Micro-Vortex Generators

Anup Zope[1], Seshendra Palakurthy[1], Eric Collins[1], Yonghua Yan[2] and Shanti Bhushan[1]

[1]Mississippi State University, Starkville, MS 39762 and [2]Jackson State University, Jackson, MS 39217

Corresponding Author: Shanti Bhushan
E-mail:bhushan@me.msstate.edu
https://doi.org/10.31753/IJRD28760101

ABSTRACT

Previous research has demonstrated that a non-linear coupling between the fluid and structural instabilities plays a key role in onset of chaotic flutter even for low-speed flows; and micro-vortex generators (MVGs) placed upstream of the shock energizes the boundary layer flow and significantly reduces SBLI induced flow separation. Based on the above studies this study proposes a passive flow control hypothesis for flutter suppression - micro-vortex generators placed upstream of the shock boundary layer interaction can introduce high frequency coherent structures in the flow resulting in a scale-gap between the fluid and structural instabilities, thereby alleviating flutter even for strong shock impingements. This study provides a preliminary validation of the hypothesis for 2D laminar flow with oblique shock impinging at center of a semi-infinite flexible panel with and without MVG. The test case is selected such that the flow without upstream MVG results in chaotic panel flutter. A MVG as high as half of the boundary layer thickness energizes the boundary layer flow and reduces the panel flutter frequency by around 5x, but the deflection amplitude is increased. The results demonstrate the MVG has the potential to modulate the flutter behavior. However, further research using 3D MVG and 2D panel, which can capture the ring vortex generation from the MVG edges is required to validate the hypothesis.

Keywords:

INTRODUCTION

Recent trends in air vehicle technology development include a renewed interest in supersonic flight vehicles and the use of lightweight aerostructures in their construction. Supersonic flight trajectories may involve segments of transonic flow regimes with mixed supersonic/subsonic flow and shock-boundary layer interactions (SBLI) over the surface of the vehicle. Such flows involve complex fluid-structure interactions (FSI), wherein the aerodynamic forces on the vehicle can generate strong elastic stresses on the structures, and when combined with the inertial forces they result in wide range of physical phenomenon or engineering problems. As depicted in Fig. 1, the combination of the inertial and aerodynamic forces results in rigid-body aerodynamics or loading problems; inertial and elastic forces result in structural dynamics or impact or vibration problems; and the aerodynamic and elastic forces result in static aeroelasticity or surface deformation problem. The combination of all these forces results in a complex problem involving dynamic aeroelasticity, such as flutter and buffeting [1,2], which results in sustained instability or structural vibration.

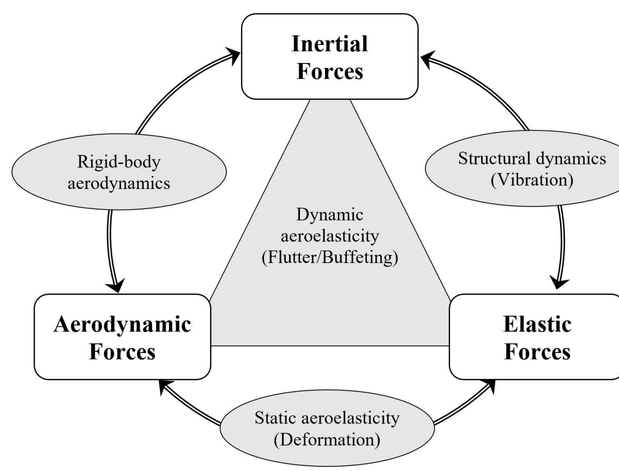

Figure 1: Schematic diagram showing forces, namely aerodynamic, inertial and elastic, observed for fluid-structure interactions (FSI), and the classes of physical phenomenon (or engineering problems) obtained using combination of the forces. The diagram is inspired from [1,2].

Flutter occurs when the structure absorbs energy from the surrounding fluid and triggers structural vibration. If the structure is disturbed at speeds below flutter speed, the resulting oscillatory motions decay. However, when the structure is disturbed at speeds above flutter speed, the oscillatory motions abruptly increase in amplitude and can rapidly lead to catastrophic structural failure. Buffet is a randomly varying structural response often triggered by intense and chaotic aerodynamic forcing functions associated with stalled or separated flow conditions. These unsteady structural responses can lead to material fatigue and premature failure of the structural members and poses significant design challenge [3].

Immense progress has been made in aeroelastic experimentation, analyses, and computational accomplishments for flutter suppression and buffet alleviation developments [3-8]. The traditional passive solution to these aeroelastic issues has been primarily to stiffen the airframe structure, thereby either eliminating undesirable excitation of structural characteristics, or ensuring that the undesirable phenomena occur only at conditions beyond the flight envelope. Unfortunately, these "passive" approach involves adding additional structure resulting in weight penalties and subsequently operational costs. Efforts have also been made to develop light-weight composite material to alleviate the wight penalties [9]. In the past four decades significant research has been performed to develop active flutter suppression systems. An active system offers a means of artificially stiffening and thereby damping the aircraft structure to increase the flutter speed by using aerodynamic control surfaces which are activated by control surface actuators through a feedback system control law (feedback gains) which receives structural motion information from dynamic motion sensors [4-8]. However, the understanding of the structural response from the small deformation linear range to nonlinearities due to very large deformation in presence of aerodynamic nonlinearities such as shock boundary layer interactions, and flow separation remains an active area of research [4].

A review of the literature shows that numerous efforts has been done over the past decade to improve the fidelity of fluid-structure interaction (FSI) solvers for dynamic aeroelasticity applications [10-15]. The solvers have been applied mostly for inviscid or laminar flow conditions and have focused on prediction of the flutter onset. Limited effort has been made in understanding the role of coupled boundary layer and structural instabilities on the flutter onset and its characteristics especially for shock-boundary layer interactions. In a previous research [16,17] authors developed and validated a FSI solver by coupling finite-volume fluids solver and finite- element structural solver, and the solver was applied for an exploratory study to understand the effect of shock boundary layer interaction on panel deformation. The study showed that shock induced flow separation induces low-frequency instabilities which are of the same order as that of the structural instabilities, and the non-linear coupling between the fluid and structural instabilities result in a chaotic panel flutter even for low-speed flows. Further it was observed that low- frequency instabilities associated with coherent turbulent flows do not result in sufficiently large elastic stresses that can induce flutter. The summary of the previous research is provided in the following section. Authors have also investigated micro-vortex generators (MVGs) as a passive control approach to alleviate or overcome the adverse effects of shock boundary layer interaction [23-25]. The study demonstrated that MVGs introduce ring-like vortices which energizes the boundary layer flow and reduces the separation length induced by the SBLI by 40% without introducing additional friction drag. A review of the work is provided in Section 3. The objective of the research is to perform high-fidelity FSI to investigate MVGs as a flow control strategy to alleviate and/or reduce structure flutter. The research builds on the above research and proposes the hypothesis that MVGs placed upstream of the SBLI can introduce high frequency coherent structures in the flow resulting in a scale-gap between the fluid and structural instabilities, thereby alleviating flutter even for strong shock impingements. The hypothesis is validated herein using FSI simulations for oblique shock impingement over a flexible semi-infinite 2D panel over a range of inflow dynamic pressures. The results of the study are shown in Section 4. Finally, some key conclusions have been drawn and expected future research directions are discussed in section 5.

Shock Boundary Layer Interaction Induced Flutter

Zope et al. [16,17] focused on development and validation of an FSI solver and application of the solver for an exploratory study to understand the effect of shock boundary layer interaction (SBLI) on panel deformation, as depicted in Fig. 2(a). The simulation setup consists of an incident shock with wave angle β that impinges on a flat plate of length L and thickness H at mid-point. The shock reflects from the impingement location, x_{imp}, and produces the reflected shock. As a result, the flow field is partitioned in three regions. In region 1, the free-stream conditions prevail, that is, the flow is parallel to the plate with Mach number: M_1, pressure: P_1 and temperature: T_1. From the oblique shock relations, fluid properties of the flow in the region 2 and 3 can be computed for a given wave angle β. For viscous flow, the incident shock interacts with the boundary layer on the plate to produce a bulge in case of a weak interaction or a separation bubble in case of a strong interaction as shown in Figures 2(b,c). Factors that determine strength of the SBLI, and hence whether the separation occurs or not include: (1) the ratio of pressure in region 3 and 1, simply called pressure ratio P_3/P_1, and (2) the type of boundary layer (e.g. laminar or turbulent). When the flat plate on which the incident shock impinges is not perfectly rigid, the shock interaction causes the plate to undergo deformation that results in either the panel taking a deflected but stationary position or undergo oscillations.

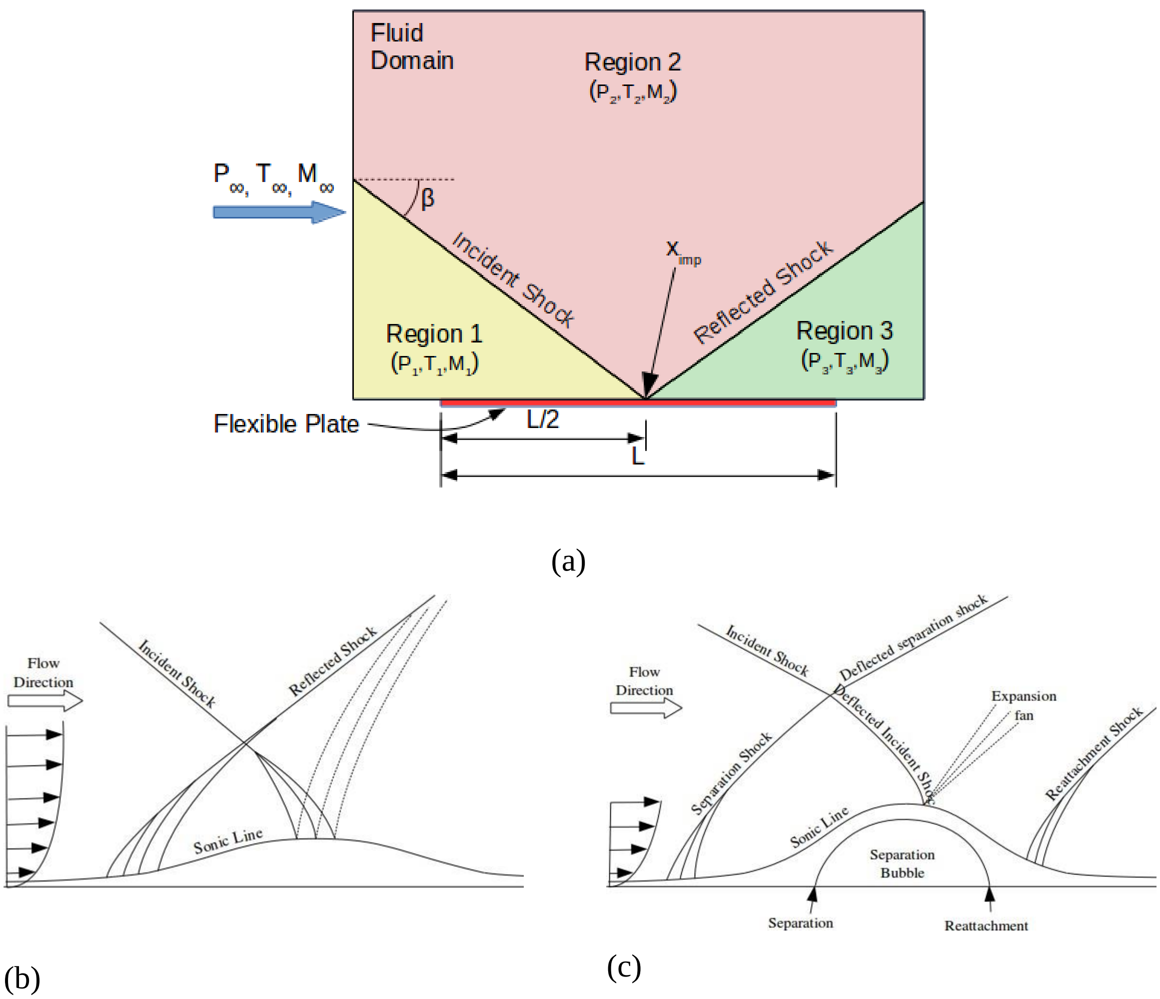

Figure 2. (a) Schematic of the shock impingement case. (b) Weak and (c) strong shock boundary layer interaction.

In this study, the fluid is assumed to be ideal gas with isentropic index γ and specific gas constant R. If the plate material has Young's modulus of elasticity E_s, Poisson's ratio ν_s, and density ρ_s, the plate flexural rigidity is:

$$D = \frac{E_s H^3}{12(1-\nu_s{}^2)} \tag{1}$$

The fluid-structure interaction problem is characterized by three non-dimensional parameters: non-dimensional dynamic pressure λ, mass ratio m_r, and pressure ratio P_3/P_1.

$$\lambda = \frac{\rho_1 \|u_1\|^2 L^3}{D} = \frac{\gamma {M_1}^2 P_1 L^3}{D} \tag{2}$$

$$m_r = \frac{\rho_1 L}{\rho_s H} \tag{3}$$

For given P_3/P_1, m_r, and λ, the fluid pressure, density, and temperature in region 1 is calculated by following equations.

$$P_1 = \frac{\lambda D}{\gamma {M_1}^2 L^3} \tag{4a}$$

$$\rho_1 = \frac{\rho_s m_r H}{L} \tag{4b}$$

$$T_1 = \frac{P_1}{\rho_1 R} \tag{4c}$$

The pressure on non-wetting side of the plate, called cavity pressure, is set to:

$$P_c = (P_3 + P_1)/2.$$

The FSI solver was validated for the predictions of bifurcation point, panel deformation amplitude and frequency for inviscid and laminar uniform flows, and flows with oblique shock with varying shock strengths $P3/P1$ = 1.2, 1.4 and 1.8 impinging on a semi-infinite 2D panel with a flexural rigidity of D = 1.42, and the results were validated [26, 27] against available benchmark results [10-11,13,15]. The exploratory study focused on inviscid, laminar and turbulent flow simulations for the medium strength ($P3/P1$ = 1.4) oblique shock impinging on a 2D panel. The simulations were mostly performed using a 2D domain consisting of around 200K fluid cells and 50 structural elements. The simulation domain, boundary condition and grid design are shown in Fig. 3.

The exploratory study showed that impinging oblique shocks induce a sharp adverse pressure gradient on the panel across the impingement location, which makes the boundary layer susceptible to separation and instabilities. The inviscid flows do not have any boundary layer and are least susceptible to separation. The laminar flow involves lower fluid momentum than the turbulent flows and are most susceptible to separation. The results demonstrated that the structural deformation can be categorized into three distinct regimes depending on the fluid- structural instability (Fig. 4).

Regime 1 is observed for low dynamic pressures (Fig. 5), wherein the panel shows steady deflection, and neither structural or fluid instability is triggered. In this regime, inviscid flow shows almost equal positive and negative deflections upstream and downstream of the shock, respectively. Both turbulent and laminar flows show higher pressure throughout the panel compared to the inviscid flow, because of the no-slip condition, resulting in higher downward deflection of the panel. However, the surface pressure is significantly modulated for the laminar case due to the presence of separation bubble over most of the panel.

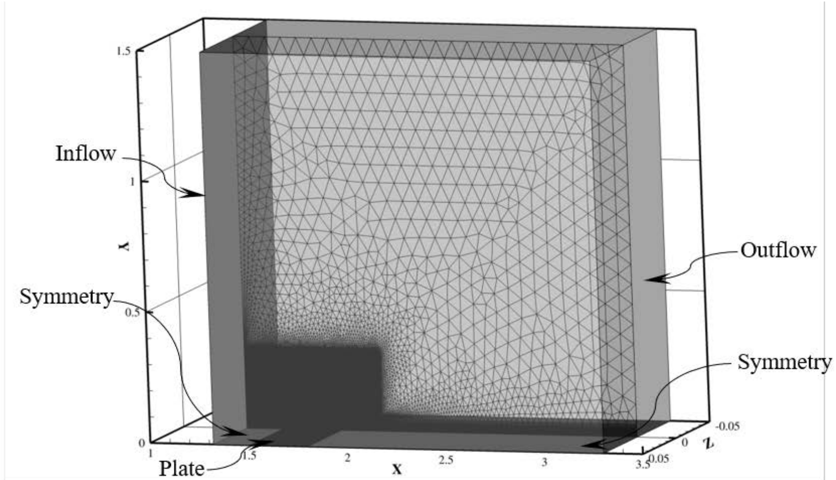

(a)

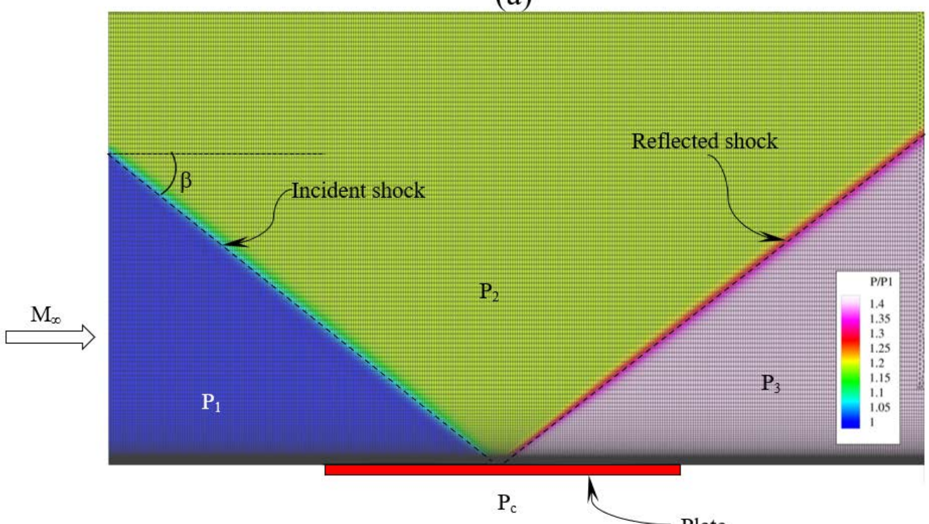

(b)

Figure 3. (a) Fluid domain containing 156,000 grid cells with dimensional units (*m*) and a volume slice along *z = 0*. The boundary condition used for the simulations are marked. (b) Zoomed-in view of near plate region shows stretched Cartesian mesh suitable for boundary layer capturing. Pressure contour shows how cell density has appropriately captured the incoming and reflected shock near the panel surface. The figure also shows the initial shock impingement characteristics.

Regime 2 is observed for very high dynamic pressures (λ = 875 for the flow condition used in the study), where the panel deflection shows limit cycle oscillation. Similar to the regime 1, the averaged panel displacement is lower for the turbulent case and even lower for the laminar case because of the no-slip condition. In this regime the inviscid and turbulent flow shows very similar amplitude and Strouhal number for the dominant components of the frequency spectrum, as flow remains attached in both the cases. Laminar flow shows 8% higher frequency, but similar amplitude compared to the inviscid/turbulent case. The separation bubble in the laminar flow shows breathing mode instability, where the bubble is enlarged when the panel is deflected downwards and is shrunk when the panel moves upwards. Considering that all the flows show similar dominant frequency and LCO pattern, the instabilities in this regime is primarily due to those of the structure.

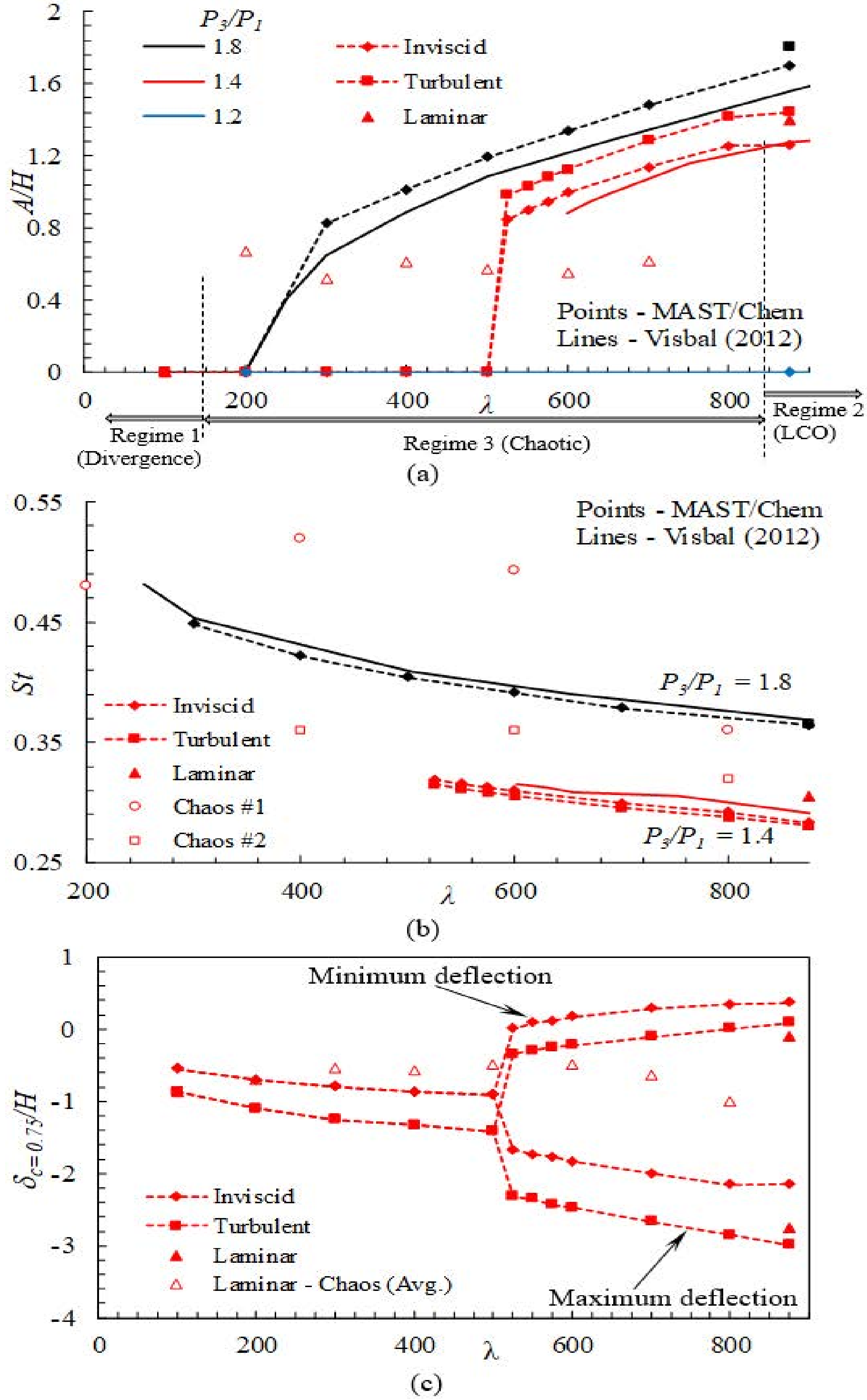

Figure 4. Panel deformation characteristics obtained for oblique shock impinging on a 2D semi-infinite plate for inviscid, turbulent and laminar flow simulations over the range $\lambda = 100 - 875$ at $M = 2$. (a) Deformation amplitude, dominant frequency and (b) averaged minimum and maximum deflection at ¾-chord length (shown only for $P3/P1 = 1.4$) domain. Solid lines correspond to benchmark results of Visbal [13]. Diamonds, squares, and triangles represent MAST/Chem predictions for inviscid, turbulent, and laminar, respectively. The open red symbols in subfigures show average amplitude and plate deflection or dominant frequencies obtained in the laminar simulations in the chaotic region.

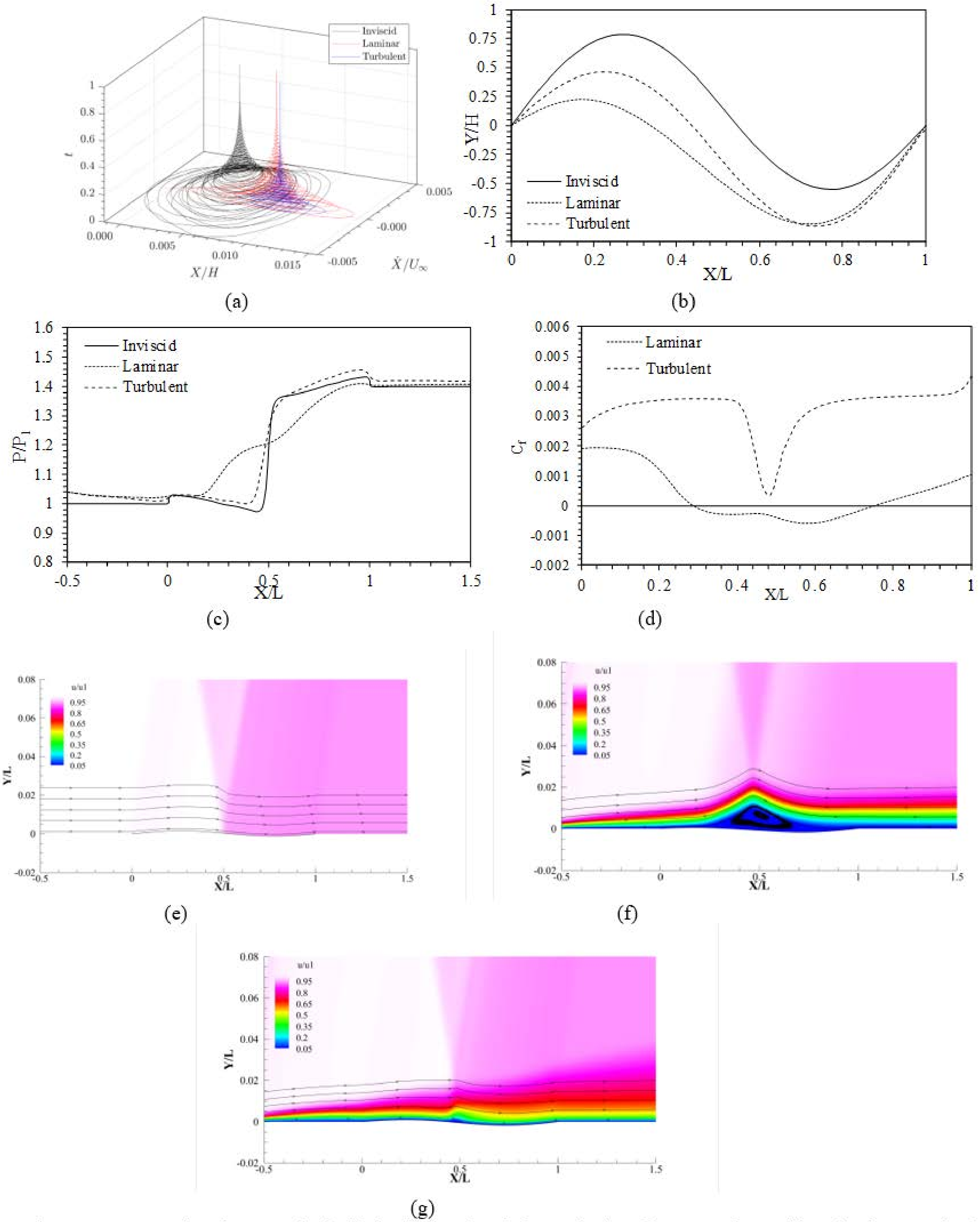

Figure 5. Comparison between inviscid, laminar and turbulent solutions for $M = 2$ flow with a shock strength of $P3/P1 = 1.4$ for $\lambda = 100$. (a) 3D phase trajectory of the ¾-chord deflection, (b) steady panel deformation, (d) skin friction coefficient, and (c) surface pressure predicted for inviscid, laminar and turbulent cases ($\Delta BL = 0.0156L$) are compared. Instantaneous $u/u1$ contours obtained for: (e) inviscid, (f) laminar and (g) turbulent flows.

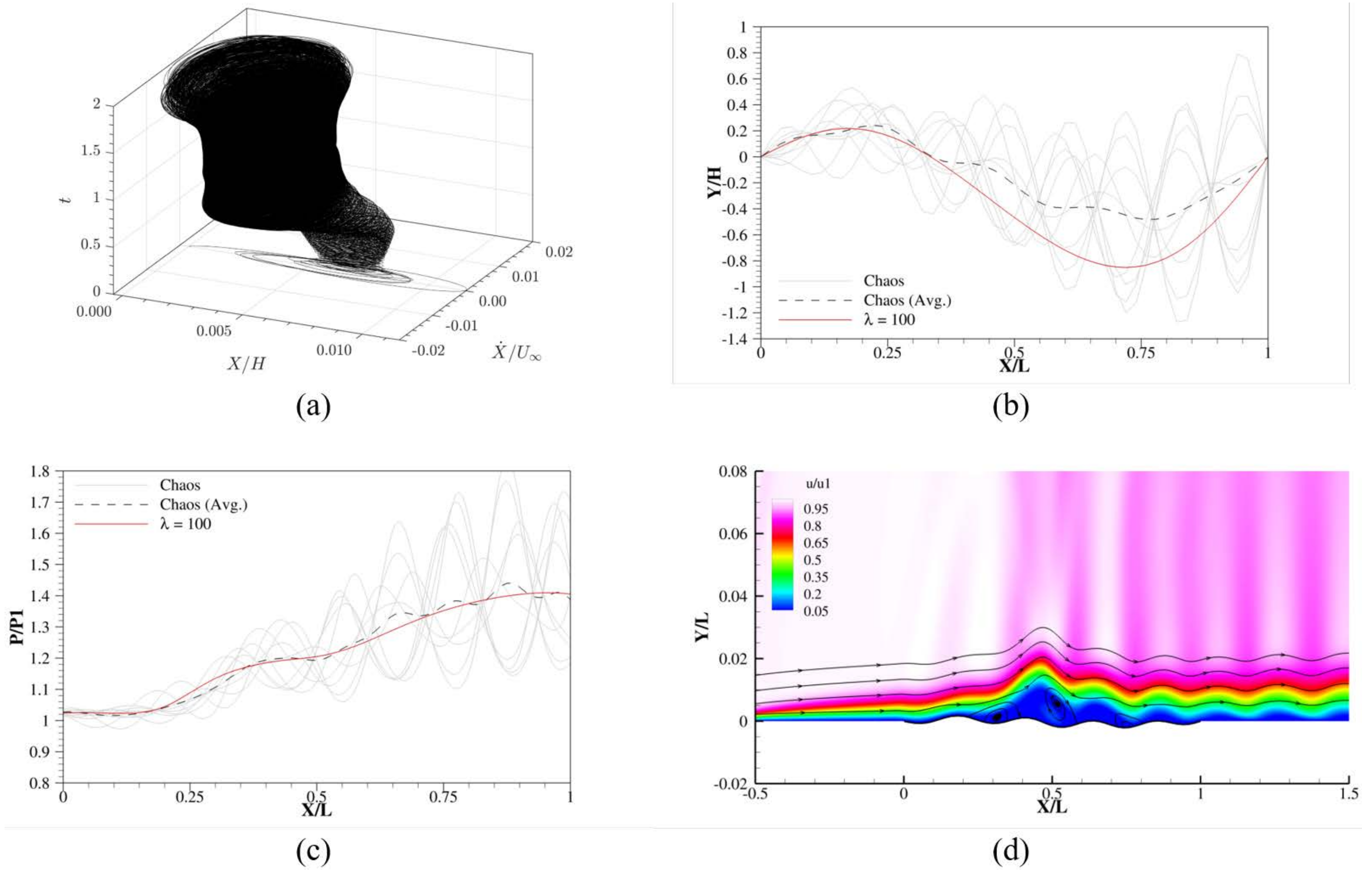

Figure 6. Chaotic flow predictions obtained for laminar flow ($\Delta_{BL} = 0.0156L$) for $M = 2$ flow with a shock strength of $P_3/P_1 = 1.4$ and $\lambda = 800$. (a) 3D phase trajectory of the ¾-chord deflection, (b) instantaneous panel deformation, (c) surface pressure and (d) instantaneous u/u_1 contour.

A chaotic regime 3 is obtained for laminar solution in the range λ = 200 to 800, wherein the structural deformation changes from either steady state equilibrium to LCO to chaos (usually for lower λ range) or from primary LCO to secondary LCO to chaos (for higher λ range as shown in Fig. 5). Results show that although the flow is chaotic, the phase averaged solution is similar to the steady-state behavior in regime 1. The spectra of the panel deflection show that the chaotic pattern amplitude increases with λ, and the frequency spectra shows a dual peak pattern. The two peak frequencies get closer with increase in λ. For λ = 800 the dominant frequency of St = 0.31 is close to 0.29 observed in laminar and turbulent LCO.

Overall, the results suggest that for flows involving separation, panel shows chaotic deflection even for low λ due to the coupling of fluid and structural instabilities. The fluid instabilities are because of high frequency shear-layer instability (St = 0.5), whereas structural instabilities involve low frequency (St = 0.3). As λ increases, the low-frequency structural instabilities start to dominant over the fluid instability, and eventually the shear-layer instability in the flow is suppressed, and the separation bubble shows breathing mode instability with St resonant with the structural instability.

Effect of Micro-Vortex Generator on Shock Boundary Layer Interaction

SBLI induced boundary layer separation and associated adverse pressure gradients is the prominent problem faced by the air breathing propulsion system of high-speed aerovehicles. An improved understanding of SBLI and flow control technologies is expected directly benefit many engineering applications, including aerodynamics, industrial flows and combustion systems. Micro-vortex generators (MVGs) are a potentially new device which can alleviate or overcome the adverse effects of SBLI and, therefore, to improve the profile of the boundary layer [19,20].

To reveal the effect of MVGs of the flow separation, high-fidelity simulations were performed using MVG installed on the wall boundary upstream of a ramp. When the ramp interacts with a supersonic inflow it results in an oblique shock and flow separation as shown in Fig. 7(a). The turbulent flow generated from the MVGs are expected to interact with the shock affecting the SBLI characteristics. Large Eddy Simulations (LES) are performed using constant coefficient Smagorinsky model using a 5th order bandwidth optimized WENO scheme [21]. A fully developed turbulent inflow is generated upstream of the MVG such that boundary layer thickness is twice the height of MVG. The dimensions and location of the MVG with respect to the ramp is shown in Fig. 7(b). The simulation domain is discretized using a structured grid consisting of 137 × 192 × 1600 points along the spanwise, wall-normal and streamwise directions. The detailed dimensions of MVG and the computational domain can be found in [25]. An explicit third- order TVD-type Runge-Kutta scheme is employed in time marching. The wall boundary adopts the adiabatic, zero-gradient of pressure and non-slipping conditions and non-reflecting boundary conditions are applied at the upper boundary to avoid possible wave reflection. The conditions of front and rear boundary surfaces in the spanwise direction are set as periodic conditions, thus the simulation mimics simulations using MVG array. Simulations are performed for inflow Mach Number Ma = 1.5, 2.0 and 2.5. The results for Ma = 2.5 are shown herein.

To better capture and understand the vortex structures in the flow field, a novel vortex identification method – Rortex/Liutex [22], which can capture both axes and the magnitude of local fluid rotation is used in this study. Figure 8(a) shows the complex vortex structure in the supersonic flow with Ma 2.5 using the iso-surface of Rortex (R)=0.3 [22]. The ramp shock wave is also presented using the iso-surfaces of pressure. One can observe that large-scale ring-like vortices are generated at the boundary of a cylindrical momentum deficit shortly downstream of the MVG. In previous studies [23-25] it has been reported that these ring-like vortices are quite robust, travel downstream and interact with the strong ramp shock. It can be observed that the iso- surfaces of gradient pressure are discontinuous where the ring-like vortices interact with the ramp shock wave. Moreover, the 3-D ramp shock waves are irregular close to the upper boundary layer, which indicates that the ramp shock wave is distorted and weakened substantially due to the interaction with the ring-like vortices. Figure 8(b) shows the separation zone for the flow using the contour of the streamwise velocity gradient along the wall normal direction on the wall. Note that the separation zone at the wall boundary is eliminated at locations where the ring-like vortices and the shock interacts. Thus, the large-scale ring-like vortices produced by MVG are proven to effectively control SBLI induces separation zone and control the low frequency noises.

(a)

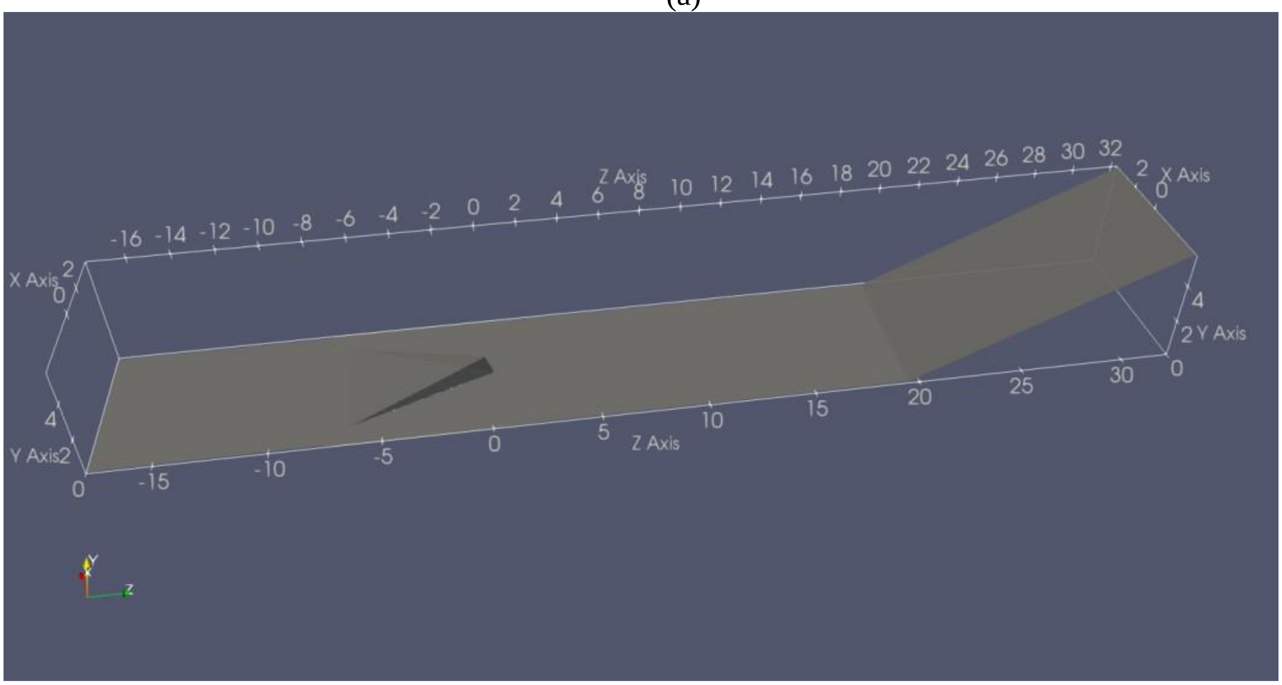

(b)

Figure 7. (a) Schematic description of the flow simulated in the study. (b) The dimensions of the MVG and the flow domain.

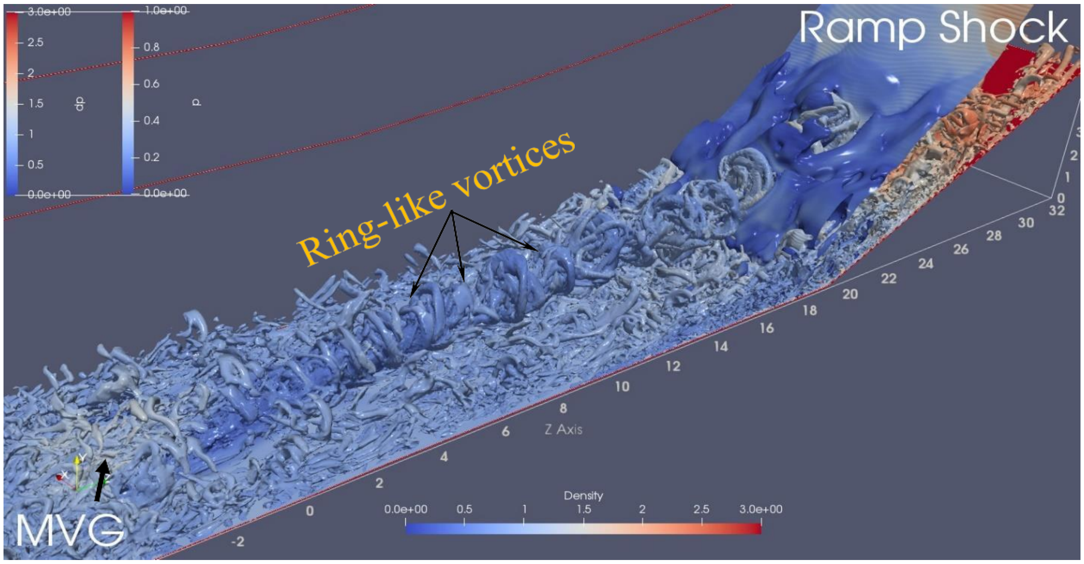

(a)

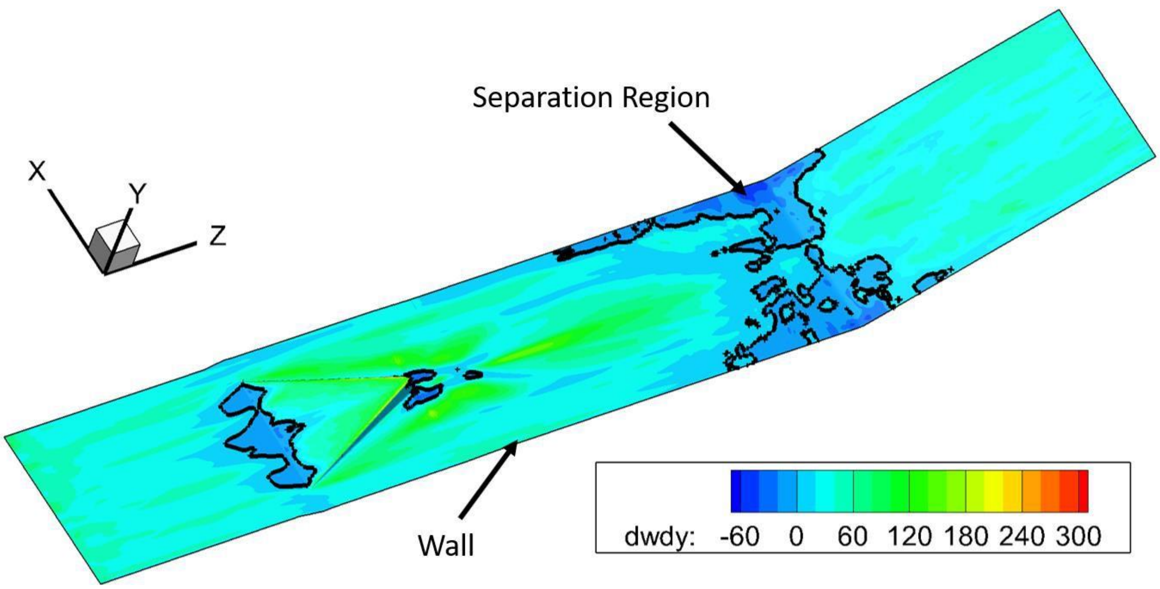

(b)

Figure 8. (a) Vortex structure and ramp shock wave obtained for Ma =2.5. The vortical structures are shown using iso-surface of Rortex (R)=0.3. The ramp shock is shown using isosurface of pressure. (b) Separation region on the bottom wall shown for Ma = 2.5 using contours of wall- normal gradient of the streamwise velocity (*dw/dy*).

Effect of Micro-Vortex Generator on Flutter

This section presents preliminary analysis of the effect of the micro-vortex generator on the panel flutter. The analysis was performed for free-stream Mach number $M_1 = 2.0$, shock pressure ratio $P_3/P_1 = 1.4$, mass ratio $m_r = 0.1$, and non-dimensional pressure of $\lambda = 800$. The pressure ratio sets the incident shock angle to $\beta = 32.58°$ corresponding to the flow deflection angle of $\theta = 3.0895°$. As discussed in section 2, $\lambda = 800$ results chaotic flutter for the laminar flow case, thus this case is selected for the analysis of the role of MVG.

The single-cell wide computational grid was used for the simulations along with the boundary conditions is shown in Figure 9(a). The rectangular portion of the domain extends from [-1.5, 1.5] m in the streamwise direction and [0, 0.8] m in the wall normal direction. The flexible panel extends from [-0.15, 0.15] m so that the midpoint of the panel is at the origin. The grid has structured mesh in the rectangular region of the domain with 600 × 470 cells in the spanwise and wall normal directions. The streamwise direction has uniform grid spacing that makes Δx = 0.005m. The wall normal direction has stretched grid with hyperbolic tangent distribution using 351 mesh points and wall normal spacing of $\Delta y_{\mathrm{wall}} = 2.5 \times 10^{-6}$ m up to a distance of 0.2 m, and uniform spacing of 0.005 m from 0.2 m to 0.8 m using 121 grid points. Thus, the grid has 282 K cells in the rectangular region. The left and top boundary are split for application of region 1 and region 2 boundary conditions listed in Table 1 so that the incident shock impinges on the panel at midpoint. The flow properties listed in Table 1 are for λ = 800. Note that, the flow velocity for region 1 boundary is parallel to the wall in the positive x-axis, whereas that at the region 2 boundary is at an angle of −3.0895° with respect to the positive x-axis. Symmetry boundary conditions are applied in the spanwise direction to simulate the 2D flow. The cavity pressure is 9042.5 Pa.

Table 1: Boundary conditions for $\lambda = 800$

Fluid Property	Region 1	Region 2
Pressure [Pa]	7537.322	8942.45
Temperature [K]	48.6	51.05
Mach Number	2.0	1.8892

The flow is assumed laminar with the flexible plate leading edge boundary layer thickness of δ/L = 0.00633, which is around 40% of the BL thickness considered for the laminar cases in Section 2. Time accurate simulations are performed using implicit time integration and time step of $\Delta t = 1 \times 10^{-5}$ s. For each λ , fluid only simulation is conducted to obtained steady state solution, which is then used for starting the unsteady FSI simulation.

For MVG simulations, the MVG shown in Figure 9(b) is used. Though the figure shows full 3D dimensions of the MVG, only the 2D projection of the MVG is used for the 2D simulations in this analysis. The MVG starts at $x = -0.4$ m and has a height of h = 0.00053 m, which is around half of the boundary layer thickness at $x = -0.4$ m. The length of the MVG is l = 0.003486 m, which is around 3.28 times the boundary layer thickness. To capture the flow near the vortex generator accurately, grid in the region is refined as shown in Figure 9(c). As a result, the total number of cells in the grid for the MVG analysis is 461 K.

For the flow configuration without the MVG, Figure 10(a) shows color plot of $\|U\|/\|U_\infty\|$ which is superimposed with line integral convolution of the velocity field for visualization of the vortices. The color plot is scaled by the panel length L in the streamwise direction and by 50 × in the wall normal direction for better visualization of the panel modes and vortex structure near the deformed panel. The inset figure shows the time history of the displacement at ¾$^{\text{th}}$ chord location on the plate. As expected, the panel displays chaotic flutter consisting of many superimposed waves that have varied frequencies and amplitudes.

For λ = 800, FSI analysis with the MVG is carried out to understand the effect of the MVG on the panel response. As shown in Fig. 11, the cusp of the MVG creates an expansion fan from the corner, that accelerates the flow and reduces pressure. However, a compression wave generates due to the vortices in the backward facing step, which causes continuous vortex shedding in the boundary layer downstream of the MVG. This flow modification influences the panel flutter and the panel deflection shows a more reduced frequency oscillations as shown in Fig. 10(b).

FFT analysis of the 3/4$^{\text{th}}$ chord deflection time history in Fig. 12 shows that addition of MVG upstream of the shock impingement modulates the panel response significantly. Fig. 12(a) shows the 3/4$^{\text{th}}$ chord displacement in the left panel and its FFT in the right panel. The FFT plot additionally shows the fundamental frequencies of the panel according to Rayleigh estimates, where f_i is the fundamental frequency of i^{th} mode. Similarly, Fig. 12(b) shows the 3/4$^{\text{th}}$ cord deflection and its FFT for the case with MVG. These graphs show that for the no-MVG case, the panel exhibits a number of frequencies, primarily concentrated around 6$^{\text{th}}$ and 7$^{\text{th}}$ mode, and some low intensity signals around the third mode of vibration. These correspond to Strouhal numbers of around 2 and 0.4, respectively. With the introduction of MVG, the panel exhibits much lower frequencies as shown in Fig. 12(b). These correspond primarily with the third mode of vibration and secondarily with the first and second mode of vibration. The corresponding Strouhal numbers are around 0.42 and 0.11, respectively. However, the amplitude of panel flutter has increased from $\Delta y/H$ = 0.038 to $\Delta y/H$ =1.15 due to the MVG effect.

In contrast to the 2D ramp considered in this study, a 3D MVG does not involve the backward facing step geometry, which would avoid formation of a compression wave. Thus, better mixing of momentum with the boundary layer flow is expected, and that would help reduce the separation on the flexible panel due to shock impingement and delay the onset of panel flutter. In addition, 3D MVG generate ring vortices from the corners which play a key role in energizing the boundary layer flow. Further analysis is required to confirm the hypothesis.

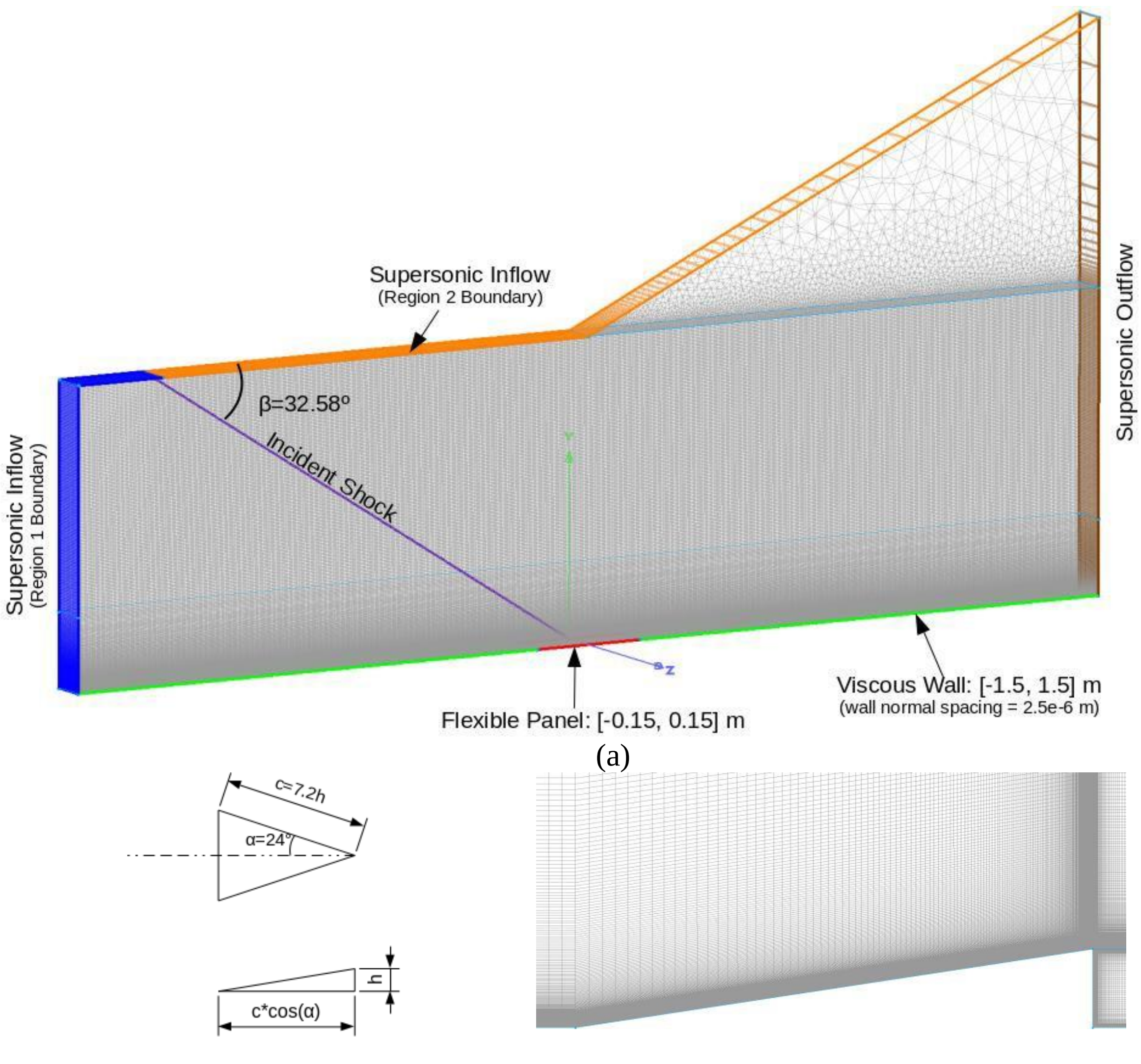

Figure 9. (a) Grid and boundary conditions used for 2D analysis. (b) MVG design and (c) refined grid near the MVG.

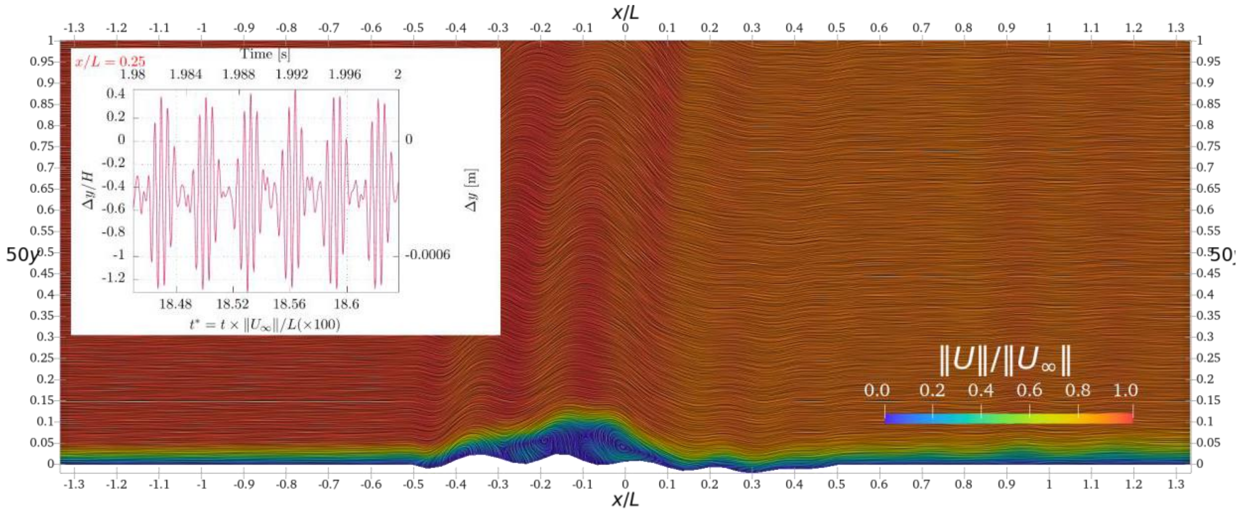

(a)

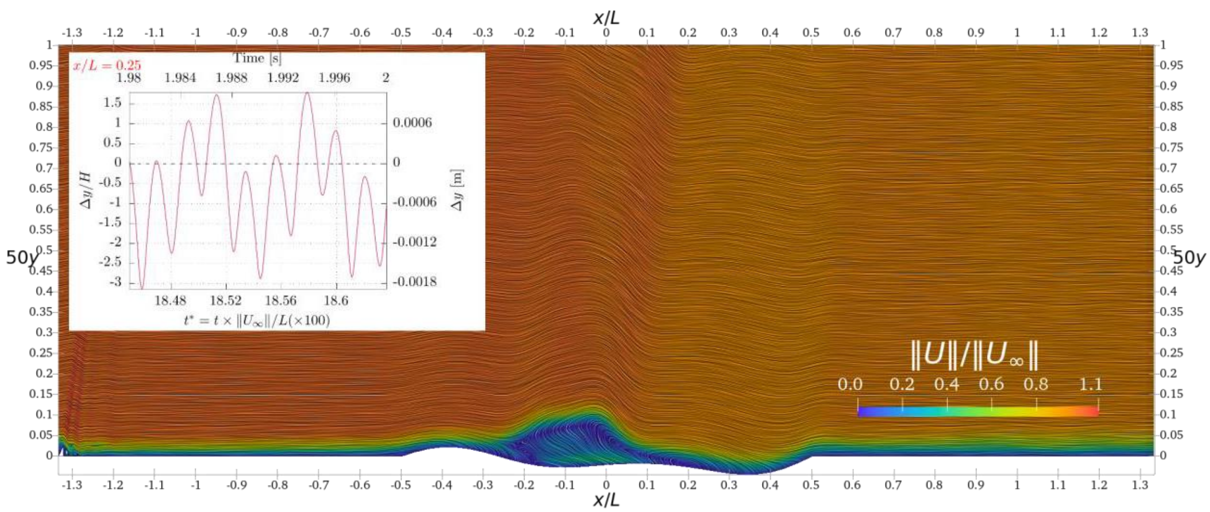

(b)

Figure 10. Color plot of the non-dimensional velocity magnitude along with the associated velocity field line integral convolution for identification of vortices obtained for $\lambda = 800$. The inset figures show the time history of the non-dimensional displacement $\Delta y/H$ at $x/L = 0.25$. Predictions for (a) the cases without MVG, and (b) with MVG. Note that the plot is using 1:50 scale, i.e., vertical axis has been stretched 50 times for better visualization of the flow.

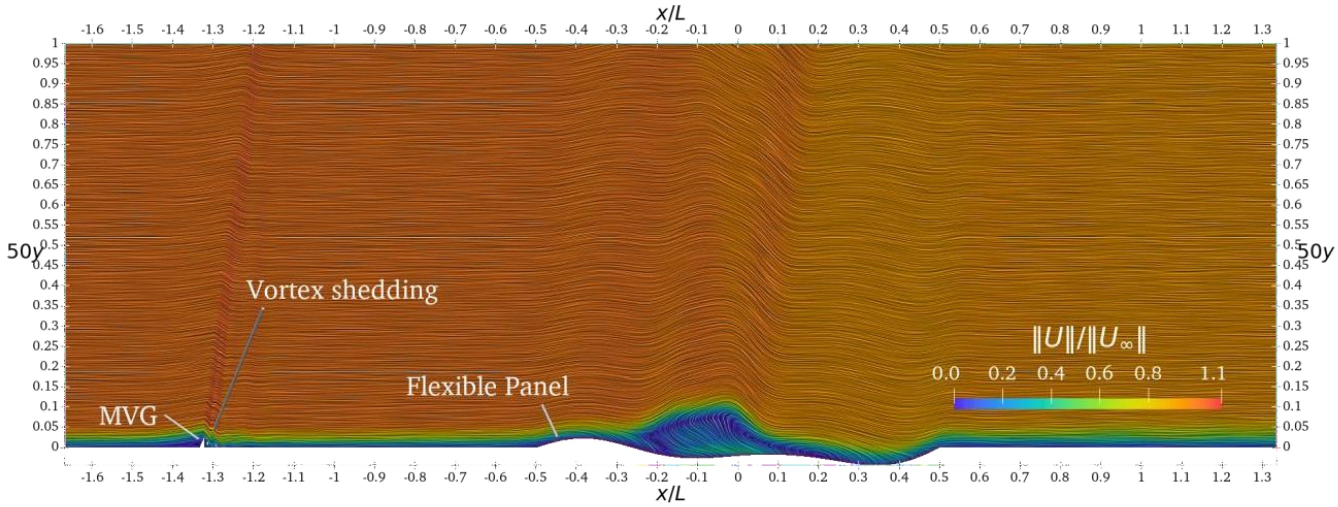

Figure 11. Color plot of pressure for $\lambda = 800$ flow over flexible panel with MVG.

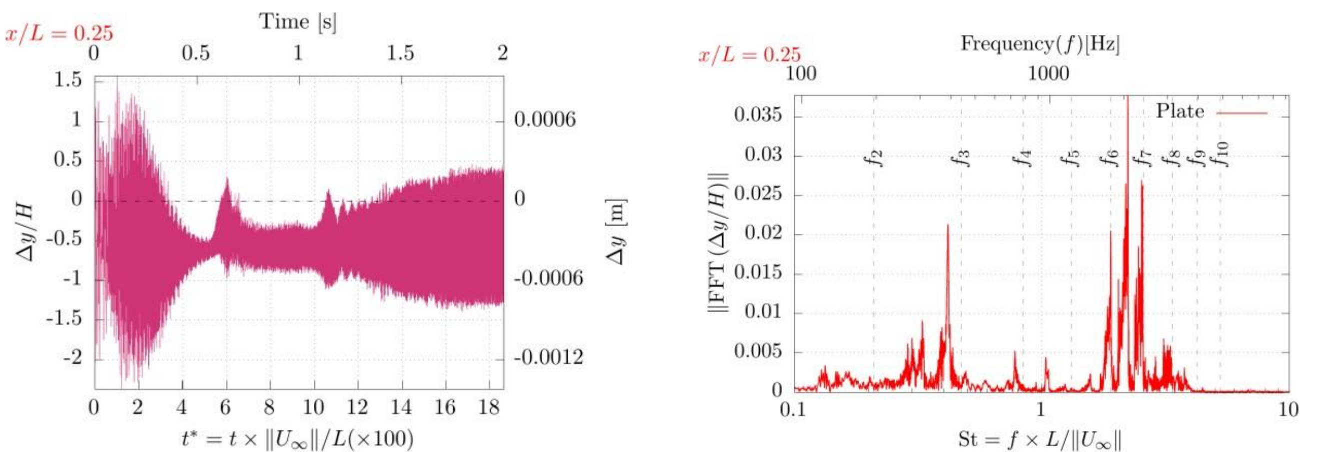

(a)

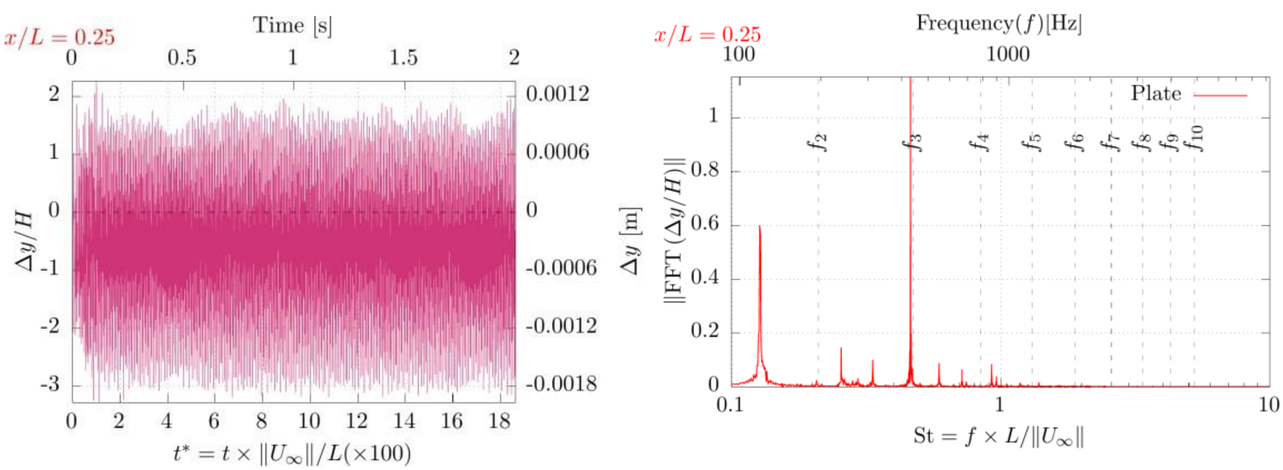

(b)

Figure 12. Time history of 3/4[th] chord displacement of the flexible panel for $\lambda = 800$ (left panel) and associated frequency spectra (right panel) for (a) without MVG and (b) with MVG. The dashed vertical lines show the fundamental natural frequencies of the panel according to the Rayleigh estimate

CONCLUSIONS AND FUTURE WORK

This study proposes a passive flow control hypothesis for flutter suppression, which is micro-vortex generators placed upstream of the shock boundary layer interaction can introduce high frequency coherent structures in the flow resulting in a scale-gap between the fluid and structural instabilities, thereby alleviating flutter even for strong shock impingements. The hypothesis builds on authors' previous research where it was demonstrated that: (a) a non-linear coupling between the fluid and structural instabilities plays a key role in onset of chaotic flutter even for low-speed flows; and (b) micro-vortex generators (MVGs) placed upstream of the shock energizes the boundary layer flow and significantly reduces SBLI induced flow separation.

The hypothesis was tested for a 2D laminar flow with oblique shock impinging at center of a semi- infinite flexible panel with and without MVG upstream of the panel. Note that, for the 2D case, the MVG is a 2D ramp. The MVG height and length were about 0.5 and 3.28 times the boundary layer thickness. The dynamic pressure for the flow was selected based on previous study such that the panel undergoes chaotic flutter. The flow over MVG creates expansion wave from the tip which results in flow acceleration and reduction in boundary layer thickness. However, the compression wave from the corner and resulting vortex shedding somewhat decelerates the flow. This presence of MVG causes around 4.8x reduction in the panel flutter frequency, but the deflection amplitude is increased by around 3x.

Overall, the results demonstrate the MVG has the potential to modulate the flutter behavior. However, the 2D study does not accurately capture the ring vortex generation from the MVG edges, which are the key for energizing the boundary layer. Further research is required to validate the hypothesis using 3D MVG and 2D panel.

ACKNOWLEDGMENTS

The research at Mississippi State University was funded by NASA EPSCoR under grant number 80NSSC17M0039. All the simulations were performed using MSU HPCC systems.

REFERENCES

1. Collar, A. "The expanding domain of aeroelasticity", The Aeronautical Journal 50, 613– 636, 1946.
2. Costanzo, A., "Experimental investigation of shock wave-boundary layer interaction on a generic oscillating bump", MS Thesis, KTH Industrial Engineering and Management, 2014.
3. Chambers , Joseph R., "Innovation in Flight: Research of the NASA Langley Research Center on Revolutionary Advanced Concepts for Aeronautics", 2005, 389 pages. https://history.nasa.gov/monograph39/mon39_b.pdf
4. Mukhopadhyay, V., "Historical Perspective on Analysis and Control of Aeroelastic Responses", Journal of Guidance, Control, and Dynamics, vol. 26, no. 5, pp. 673–684, 2003.
5. Zhao Y. H., "Flutter suppression of a high aspect-ratio wing with multiple control surfaces", *Journal of Sound and Vibration*, vol. 324, no. 3–5, pp. 490–513, 2009.
6. Zeng, J., Kukreja, S. L., and Moulin, B., "Experimental model based aeroelastic control for flutter suppression and gust-load alleviation," *Journal of Guidance, Control, and Dynamics*, vol. 35, no. 5, pp. 1377–1390, 2012.
7. Liu , H., Zhao, Y., and Hu H., "Adaptive Flutter Suppression for a Fighter Wing via Recurrent Neural Networks over a Wide Transonic Range", *International Journal of Aerospace Engineering* Volume 2016, Article ID 7673146, 9 pages
8. Livne E., "Aircraft Active Flutter Suppression: State of the Art and Technology Maturation Needs", *Journal of Aircraft*, Vol. 55, No. 1, January–February 2018
9. Dillinger, J.K.S.; Klimmek, T.; Abdalla, M.M.; Gürdal, Z. "Stiffness Optimization of Composite Wings with Aeroelastic Constraints". *Journal of Aircraft*. 2013, 50, 1159–1168.
10. Gordnier, R.E., Visbal, M.R., "Computation of three-dimensional nonlinear panel flutter". *Journal of Aerospace Engineering*, 2003, 16, 155–166.
11. Li, Y., Luo, H., Chen, X., Xu, J., "Laminar boundary layer separation over a fluttering panel induced by an oblique shock wave". *Journal of Fluids and Structures* 2019 90, 90– 109.
12. Vedeneev, V., "Interaction of panel flutter with inviscid boundary layer instability in supersonic flow", *Journal of Fluid Mechanics*, 2013, 736, 216–249.

13. Visbal, M. ‘On the interaction of an oblique shock with a flexible panel”. *Journal of Fluids and Structures*, 2012 30, 219–225.
14. Shinde, V., McNamara, J.J., Gaitonde, D.V., Barnes, C.J., Visbal, M. R., “Panel Flutter Induced by Transitional Shock Wave Boundary Layer Interaction”, in 2018 Fluid Dynamics Conference, p. 3548.
15. Ostoich, C.M., Bodony, D.J., Geubelle, P.H. “Interaction of a Mach 2.25 Turbulent Boundary Layer with a Fluttering Panel using Direct Numerical Simulation”. *Physics of Fluids*, 2013, 25, 110806.
16. Zope, A., Horner, C., Collins, E.M., Bhushan, S., Bhatia, M., “Investigation of Flexible Panel Dynamic Response Induced by Coherent Turbulent Vortical Structures”, in *AIAA Scitech 2021 Forum*, 2021, p. 0251. doi:10.2514/6.2021-0251.
17. Zope, A.D., Schemmel, A., Bhatia, M., Bhushan, S., Collins, E.,. “Development and Validation of Fluid-Thermal Interaction Solver for High Fidelity Transient Simulations”, in *AIAA AVIATION 2020 FORUM*, 2020, p. 3006.
18. Bhatia, M., Beran, P., “Transonic Panel Flutter Predictions using a Linearized Stability Formulation”. *AIAA Journal*, 2017, 3499–3516.
19. Babinsky, H., Li, Y., and Ford, C.W.P., "Microramp Control of Supersonic Oblique Shock- Wave/Boundary-Layer Interactions", AIAA J., Vol. 47(3), pp.668-675(2009).
20. Estruch-Samper, D., Vanstone, L., Hillier, R., Ganapathisubramani, B. “Micro Vortex Generator Control of Axisymmetric High-Speed Laminar Boundary Layer Separation”. *Shock Waves* 25(5), 521-533 (2015).
21. M.P. Martın , E.M. Taylor, M. Wu and , V.G. Weirs. “A Bandwidth-Optimized WENO Scheme for the Effective Direct Numerical Simulation of Compressible Turbulence”. *Journal of Computational Physics*, Vol 220, pp 270-289, 2006.
22. Chaoqun Liu, Yi-sheng Gao, Xiang-rui Dong, Yi-qian Wang, Jian-ming Liu, Yu-ning Zhang, Xiao-shu Cai and Nan Gui. “Third Generation of Vortex Identification Methods: Omega and Liutex/Rortex Based Systems”. *Journal of Hydrodynamics*, Vol 31(2), pp 774- 781, 2019.

Study of Soil Surface Sealing and Crusting using a Seismic Surface Wave Method

Zhiqu Lu and G. V. Wilson

[1]National Center for Physical Acoustics, The University of Mississippi, University, MS, 38677 and [2]USDA-ARS National Sedimentation Laboratory, Oxford, 38655, MS

Corresponding author : Zhiqu Lu

Phone : 662-915-5660

Fax: 662-915-3949

Email: zhiqulu@olemiss.edu

https://doi.org/10.31753/IJRD2876018

ABSTRACT

Soil surface sealing and crusting are formed through the processes of raindrop impact, drying, and clogging of pores. This creates a mechanically hard top layer that shows high stiffness, mechanical strength, seismic velocity, and reduced infiltration rate. The existence of surface seals and crusts affects soil erodibility and run-off. In this study, a non-invasive seismic surface wave method was employed to evaluate surface crust and the profile below. The method was based on the multi-channel analysis of surface wave method (MASW). Unlike the conventional MASW methods used in geotechnical and civil engineering applications for exploring subsurface soil from several meters to tens of meters below the surface, the present method aimed at very thin layer (several centimeters) by increasing frequency up to kHz. A self-adaptive high-frequency MASW method with a variable sensor spacing configuration was employed for the task. After signal processing and inversion, a shear wave velocity soil profile was determined from which the top hard layer was evaluated. In this study, the MASW tests were conducted on a naturally formed sealed/crusted soil and on a non-sealed/non-crusted soil as a control test. Soil cores, shear vane and penetration tests were conducted to compare with the observations from the MASW method. The results from both the MASW method and invasive tools are in good agreement, demonstrating that the MASW method can be used to evaluate and assess soil sealing and crusting layer in situ and to explore the soil profile in the vadose zone.

Key words: multichannel analysis of surface wave, Rayleigh waves, dispersion curve, shear wave velocity, surface sealing and crusting.

Abbreviations: MASW, multichannel analysis of surface wave; FFT fast Fourier transform; S, shear; HVL, high velocity layer; LVL, low velocity layer.

INTRODUCTION

Soil sealing and crusting plays a critical role in the hydrology and productivity of agricultural and natural landscapes. In a recent review of soil sealing and crusting, Nciizah and Wakindiki (2015) listed the following detrimental effects of sealing and crusting: reduced infiltration, increased soil erosion, mechanical impedance of seed emergence, reduced aeration, greater energy expended for tillage operations, and increased number of tillage operations to remove crust. It is generally agreed that the most important effect is the reduction of soil infiltration capacity. Reduction in infiltration rate increases the runoff and thus the potential for erosion as well as decreases moisture stored in the soil profile for plant growth. Thus, if sealing and crusting covers enough landscape area it can have detrimental effects on a watershed's hydrology by increased flashiness and magnitude of storm hydrographs and reduced aquifer recharge. Hydrus-1D simulations of a hillslope by Sela et al. (2012) showed that crusts could off-set the loss of water storage due to reduced infiltration by reducing the evaporation losses. While there could be a threshold, depending upon the rainfall intensity and soil depth, between crusts reducing infiltration versus reducing evaporation from a soil-water conservation-plant use stand-point, there is still a detrimental effect of increased runoff from a water management standpoint.

Many researchers distinguish between a surface seal and crust although the two are intricately related. The Glossary of Soil Science Terms (2008) defines a soil crust as “a transient soil-surface layer, ranging in thickness from a few millimeters to a few centimeters, that is either denser, structurally different or more cemented than the material immediately beneath it, resulting in greater soil strength when dry,” whereas, a seal is defined as “the deposition by water, orientation and/or packing of a thin layer of fine soil particles on the immediate surface of the soil, generally reducing its permeability.” Valentine (1995) simply viewed a seal as a “wet crust” which is consistent with the use by Singer and Shainberg (2004) of “seals are wet and crust are dry” but otherwise the terms can be used interchangeably.

Sealing and crusting is generally viewed (Singer and Shainberg, 2004; Nciizah and Wakindiki, 2015) as a two-step process in which raindrops breakdown aggregates into finer fragments and/or primary particles and clogging of pores by infiltration of suspended particles. Breakdown by raindrops is due to the physical force of impact, physical disintegration of aggregates by slaking, which is the micro-explosions within dry aggregates due to rapid jumps in entrapped air pressures by sudden wetting of the aggregate upon contact with raindrops, and physicochemical dispersion of clays due to the low electrolytic composition of rainwater. These dispersed particles and micro-aggregates are suspended in the infiltrating water which clogs pores as the top millimeters of the soil surface filters them out of solution. Subsequent raindrops compact this surface seal further to depths below the immediate surface seal. The degree of compaction, e.g. magnitude of the soil strength increase and depth of crust, depend, therefore, on the kinetic energy of the raindrops, wetting-rate (rainfall intensity), rainwater chemistry as well as soil properties, e.g. soil texture, organic matter content and composition, aggregate stability, soil strength, antecedent moisture conditions, and soil-water chemistry (Agassi et al., 1981, 1985). Singer and Shainberg (2004) concluded from their review of literature that the kinetic energy of rain dominates the seal/crust formation in medium to light-textured soils and wetting rate is dominate in heavy textured soils.

Given that the most significant impact of soil crusting is on infiltration (Romkens et al., 1985), the most common method used to characterize soil crust has been the infiltration rate and hydraulic conductivity (Nciizah and Wakindiki, 2015). Other methods commonly used to delineate areas with soil crust are soil strength, penetration resistance, wet–sieving for aggregate stability, and scanning electron microscopy (SEM) of thin sections (Valentin and Bresson, 1997, Remley and Bradford,1989). Recently, researchers have used high resolution X-radiography images to characterize soil crust (Bresson et al., 2004; Lee et al., 2008) on samples obtained from repacked soil that was subjected to simulated rainfall. Ben-Dor et al. (2003) conducted a laboratory study on repacked soil subjected to simulated rainfall to evaluate the potential for imaging spectroscopy to map soil crust. They found significant spectral differences between crusted and non-crusted soil which were related mostly to texture and mineralogy. They suggested that this technique be tested for remote sensing of crust. de Jong et al. (2009) evaluated the use of hyperspectral remote sensing and found that spectral differences between crusted and non-crusted areas was small with differences mainly in the albedo values. While they concluded that it was possible to use this technique for remote sensing of crust patterns on the landscape, they cautioned that it should be used with care as differences were subtle between crusted and non-crusted areas.

Another non-intrusive technique proposed by Leary et al. (2009) was the use of acoustic techniques. They did preliminary tests on repacked soils with two contrasting erodibilities that were subject to simulated rainfall. This laboratory study found a lower acoustic-seismic admittance on raindrop impacted samples than gently wetted samples which suggest that acoustic techniques could be used in field conditions to map soil crust. The objective of this study was to determine the potential of acoustic/seismic methods for detecting soil seal/crust under field soil conditions subjected to natural rainfall events. As noted by Hussein et al. (2010), few studies on crusting have been carried out in situ under natural rainfall conditions.

In practice, a non-invasive technique for in situ assessing soil surface sealing/crusting is always preferred. For this, an acoustic, or more precisely, a seismic technique known as the multi-channel analysis of surface waves (MASW) method appears to be very promising. The MASW method is based on spectral analysis of Rayleigh waves - a type of seismic surface waves - to determine shear wave velocity profile, i.e. shear wave velocity as a function of depth (Park et al., 1998a; 1998b; Park et al., 1999a; Xia et al., 1999; Miller et al., 1999; Foti, 1999; Park et al., 2007). It has been increasingly applied to geotechnical and civil engineering projects such as mapping bedrock (Miller et al., 1999), detecting voids (Park et al., 1998a; 1999b) and buried objects (Grandjean and Leparoux, 2004), determining Poisson's ratio (Ivanov et al., 2000) and quality factor (Xia et al., 2002), evaluating the stiffness of water bottom sediments (Park et al., 2005), delineating fault zone and dipping bedrock strata (Ivanov et al., 2006), evaluating levees (Lane, et al., 2008), and non-destructive testing of concrete pavements (Ryden, et al., 2001; 2004; 2009; Ryden and Lowe, 2004; Alzate-Diaz and Popovics, 2009). For most of these projects, except for non-destructive testing of pavements, the MASW methods are aimed at exploring subsurface properties at depths from several meters to tens of meters and therefore employ a low frequency (less than 200 Hz) source for the targeted objectives. They usually treat the top layer of soil, typically with a thickness of a couple of meters of weathered parent material, as an effective layer with average properties. Therefore the detailed structural information of the top layer of soil cannot be determined (Park et al., 1999a).

Recently a high-frequency MASW method has been developed, in which either an accelerometer or a laser-Doppler vibrometer is used as a sensor to detect surface vibrations generated by an electrodynamic shaker operating in chirp mode with frequency ranging from 40 Hz to 500 Hz, to explore subsurface soil with a depth of 2.5 meters below the surface (Lu, 2014a; Lu, et al. 2014). The method has found its application in studies of seasonal and weather effects on shallow surface soils (Lu, 2014a) and in the detecting and imaging of a soil fragipan (Lu, et al., 2014). In this study, the high-frequency MASW method is further extended up to kHz frequency range for studying soil surface sealing and crusting. When conducting MASW test at such high frequencies, some technical problems emerged. To solve these problems, a self-adaptive MASW method with variable sensor spacing was developed. This new MASW method increases the accuracy and frequency range in the determination of the dispersion curve and the spatial resolution of soil profile.

MATERIAL AND METHODS

Site and soil characterization

The study was conducted at the North Mississippi Branch of the Mississippi Agriculture and Forestry Experiment Station at Holly Springs, Mississippi. The soil was a Providence silt loam (fine-silty, mixed, active, thermic Oxyaquic Fragiudalfs) which is a moderately well drained soil that developed from loess (mainly silt) deposits over sandy coastal plain parent materials. The typical soil profile consists of an Ochric epipedon (silt loam, weak fine granular structure) from the surface to about 15 cm that transitions to argillic (silt loam and silty clay loam, subangular blocky) horizons that extend to about 60 cm depth, followed by fragipan (silt loam and loam, prismatic structure that are dense and brittle) horizons that extend to about 125 cm.

The site was prepared by clearing the surface of vegetation on March 18, 2015 and being maintained bare using herbicides. A soil seal/crust formed by natural rainfall prior to time of acoustic/seismic testing on 2 May, 2015. The seal/crust was first sampled on 7 May, 2015 by taking five undisturbed soil cores (0.084 m diameter by 0.01 m length) from the surface (0-1 cm depth) and four soil cores (0.084 m diameter by 0.03 m length) from below the crust (2-5 cm depth). Additionally, the following *in situ* measurements were made at multiple locations along the transect where acoustic measurements were made: shear strength at the surface using with a Torvane shear vane (Durham Geo Slope Indicator, www.DGSI.info), shear strength in 0.1 m depths increments to 0.5 m depth with a Geonor shear tester (H-60 vane tester by Geonor, Inc., www.geonor.com), and soil penetration resistance in 0.025 cm depth increments to 0.45 m depth with a Field Scout soil penetrometer (SC-9000 Soil Compaction Meter, Spectrum Technologies, Inc, www. specmeters.com). At each location, the shear vane was pressed 0.1 m into the soil and shear strength measured, a 0.1 m soil probe sample taken for water content, and the shear vane pressed into the soil probe void to the subsequent 0.1 m depth, and the process repeated in 0.1 m increments to 1 m depth or refusal. These measurements were repeated at an adjacent point using just the shear rod (dummy) without the vane to correct for resistance of the rod. The site was maintained bare and exposed to rainfall until 18 September when acoustic/ seismic measurements and soil sampling were repeated. In addition, at that time a portion of the tested area was tilled using a rotor-tiller to a depth of about 10 cm and both acoustic measurements and sampling were made on the freshly tilled area. These measurements were under very dry soil conditions. Both the seal/crust and tilled area were maintained bare and open until measurements were repeated on both type surfaces on 3 November, 2015 following three light rainfall events that provided moist soil conditions.

Rainfall was measured with a NovaLynx RG260-2500 tipping bucket rain gauge (RG260-2500 Tipping Bucket Rain Gage, NovaLynx Corp., www.novalynx.com) with a 20 cm diameter funnel and a tipping bucket that records within 1% accuracy for rainfall rates up to 50 mm/h. The rain-gauge was 0.8 km from the study site. Rainfall intensity and energy was determined using RIST 3.94 (ars.usda.gov/ Research/docs.htm?docid=3251) from the time record of each tip of the rain gauge bucket, which was equivalent to 0.254 mm. The kinetic energy of individual storms was determined according to the equation by Brown and Foster (1987).

The multi-channel analysis of surface wave method

The use of Rayleigh waves for *in-situ* soil characterization has been researched and practiced extensively in civil and geotechnical engineering for decades. Rayleigh waves are one type of surface waves that travel parallel to the soil surface. The vertical distance that Rayleigh waves penetrate into the ground decreases rapidly with depth and the propagation is confined to a limited depth, typically about one wavelength. This characteristic enables one to study different depths of subsurface soils by changing frequency (or wavelength). Since their amplitudes are inversely proportional to the square root of the distance, Rayleigh waves decay more slowly with horizontal distance than do body waves such as the longitudinal P-waves and the shear S-waves. For a circular-foot vibrating source, about two-thirds of the input energy goes into surface waves, making Rayleigh waves easily detectable. For a homogenous half-space medium, Rayleigh waves are non-dispersive and travel at a velocity of approximately 0.93-0.95 Vs when Poisson's ratio is equal to 0.33 to 0.45, where Vs is the shear wave velocity. When the acoustic velocity varies with depth due to weather effects, overburden pressure, and stratified layers, Rayleigh waves become dispersive, presenting phase velocity frequency-dependent behaviors. In other words, Rayleigh waves exhibit a unique phase velocity at each frequency (wavelength), which is directly related to the elastic properties of the associated layer of soils. This dispersive characteristic of Rayleigh waves is the basis of surface wave techniques for soil profile measurement. The shear S-wave velocity profile can then be derived by inverting the dispersive phase velocity curve using an inversion algorithm (Xia et al., 1999; 2003). It is worthy to mention that the shear S-wave velocity is related to a material's stiffness and is one of the paramount parameters in civil, geotechnical, and soil engineering. Studies show that the shear wave velocity is correlated with N-value (Imai and Tonouchi, 1982), an index value of formation hardness used in soil mechanics and civil engineering (Terzaghi et al., 1996), and penetration resistance (Gao, et al., 2013). In this study the penetration resistance profile was obtained in invasive penetration tests to verify the extracted S-wave velocity profile.

A standard MASW procedure consists of several parts: (1) generation of surface waves, (2) recording of surface waves, (3) determination of the dispersion curve, and (4) inversion, as described briefly as follows.

The MASWs usually use sledgehammers, electrodynamic shakers, weight drops, and track-mounted vibrators as sources to excite surface waves. Multiple surface vibrations are detected by multiple geophones laid out on the ground in a linear array.

To determine dispersion curve, two transformations are performed. First, the time-domain signals (time traces) are transformed through a fast Fourier transform (FFT), as expressed in the following.

$$F(\omega, x) = \frac{1}{2\pi}\int_{-\infty}^{+\infty} f(t, x)\cdot \exp(-i\omega t)dt \qquad (1)$$

where t and $\omega=2\pi f$ are time and angular frequency, f denotes frequency, $f(t, x)$ and $F(\omega, x)$ are the received signal and complex FFT spectrum, respectively, at distance x from the source, and i is the imaginary number.

The second transformation is a wavefield transformation, expressed as,

$$E(c, f) = \int_{-\infty}^{+\infty} F(\omega, x)\cdot \exp(i\omega \frac{x}{c})\cdot dx \qquad (2)$$

where $E(c, f)$ is the amplitude in c-f space and c is an arbitrary phase velocity.

The outcome of the two transformations is a so-called overtone image plotted in an intensity graph with the y-axis and x-axis represent the phase velocity and frequency, respectively, and the color represents the value of $F(c, f)$. One of the major advantages of the MASW method is its ability to deal with all the information of seismic wave signals, which usually consist of fundamental-mode and higher-modes of surface waves, body waves, reflected and scattered waves, and ambient noises (Park et al., 2007). These seismic wave components can be effectively identified or separated from the energy patterns because of their unique wave speeds, attenuations, and propagation paths. The dispersion curve can be obtained by picking up the identified fundamental-mode and possible higher modes of Rayleigh wave components.

The shear wave velocity profile, the shear wave velocity as a function of depth, is determined from the measured dispersion curve by an inversion process with an iterative algorithm. An intermediate dispersion curve is calculated using forward modeling of Rayleigh wave propagation starting with an initial earth model that includes the frequency and four soil parameters: the thicknesses of layers, the shear and longitudinal wave velocities, and the density at each layer. The estimated dispersion curve is compared with the measured one. If the comparison yields a difference greater than a threshold value, the earth model is modified. The estimation and comparison is repeated until the results converge to a pre-determined value. The shear wave velocity profile is determined from the final earth model (Xia et al., 1999; 2003).

Self-adaptive MASW method with a variable sensor spacing configuration

When the high-frequency MASW method was conducted and the collected time traces were processed in a traditional MASW manner, several problems emerged. First, existing rules for sensor geometric configuration could not satisfy the requirements of planar dominant Rayleigh waves of the fundamental mode for all frequencies of interest. In the past, there were many discussions about optimizing sensor geometric configurations (Park et al., 1999a; Park et al., 2001; Zhang et al., 2004; Xu et al., 2005; Ivanov et al., 2008) and they all focused on using fixed sensor offsets. One of the most popular rules was that, for example, the near offset (the distance between a seismic source and the first sensor) was set to be greater than half the maximum desired wavelength and the spread length (the length covered by all sensors) should be twice as large as the exploration depth (Park et al., 1999a). These rules were mostly concerned with the lowest frequency component of surface waves, rather than all frequency components. At high frequencies, seismic waves may propagate in far field distance, leading to predominant higher modes over the fundamental mode of Rayleigh waves. Secondly, the attenuation coefficients of Rayleigh waves measured in the high frequency MASW test have much higher values and dynamic range than those of conventional MASW methods. As reported by a recent study (Xia et al., 2012; Lu, 2014b, 2015), the attenuation coefficients were found in a range from 0.01 to 0.07 (1/m) and from 0.05 to 1.3 (1/m) within frequency ranges from 10 to 70 Hz and from 50 Hz to 500 Hz, respectively. This frequency-dependent attenuation nature prevents all frequency components of Rayleigh waves from propagating the same distance. On the other hand, since higher modes of Rayleigh waves have longer wavelengths than those of fundamental mode Rayleigh waves, they penetrate deeper subsurface soils (Xia, et al., 2003) and consequently are less attenuated than the fundamental mode. At certain high frequencies and distances, the energy of Rayleigh waves of the fundamental mode will not dominate over that of higher modes of Rayleigh waves, making it difficult and sometimes impossible to identify the fundamental mode of Rayleigh waves from an overtone image. Thirdly, sensor spacing may become larger than half the wavelength at certain frequencies, leading to spatial aliases at higher frequencies. To eliminate spatial aliases, one may intend to reduce sensor spacing by increasing the number of sensors. However, doing so will lead to prohibitively large numbers of sensors.

To overcome the above problems, a self-adaptive method has been developed to determine high frequency dispersion curves (Lu, 2014b; Lu, 2015), which is a minor modification of the method proposed by Park and Ryden (2007) and Park (2011). The idea is to consider wavelength as a control parameter to define the near offset and far offset at each frequency. The time traces taken into account are selected using a rule related to the wavelength, in order to spatially filter out the influence of the near and far field effects. In detail, an initial dispersion curve is obtained by a fixed-offset MASW test and used to estimate wavelengths at all frequencies of interest. At each frequency, the near offset and spread length are then set to be multiples of the wavelength. In other words, the near offset and spread length are unique at each frequency and self-adaptive to the corresponding wavelength. Furthermore, in order to avoid spatial aliases and minimize the number of sensors or sensor locations, a variable sensor spacing configuration is proposed.

For a traditional MASW method, an overtone image is obtained using the 2-D wavefield transformation by summing over the entire set of time traces. The summation form is expressed as follows (Park et al. 1998b):

$$E(c,f)=\left|\sum_{j=1}^{N} e^{i\phi_j}F_j(f)\right| \qquad (3)$$

where c, f are phase velocity and frequency, $E(c, f)$ the energy at the coordinates of (c, f) in phase velocity ~ frequency space, $F_j(f)$ the fast-Fourier-transform of the j^{th} time trace at offset x_j, phase $\phi_j=2\pi f x_j/c$, and N the total number of time traces. In this formulation, the entire set of time traces is summed and the Fourier transform $F_j(f)$ is usually normalized to unit amplitude for each trace.

For a self-adaptive MASW method, the near offset x_{near} (the distance between a seismic source and the first selected sensor), spread length L (the length covered by the selected subset of sensors), and the far offset x_{far} (the distance between a seismic source and the final selected sensor) are determined by the wavelength λ at each frequency:

$$\begin{aligned} x_{near} &= k_{near}\lambda(f) \\ L &= k_L\lambda(f) \\ x_{far} &= x_{near}+L \end{aligned} \qquad (4)$$

where k_{near} and k_L denote the multipliers for the near offset and spread length respectively. In general, the two multipliers can be adjusted slightly from 0.2 to 0.8 and from 2 to 4 respectively in order to obtain the best overtone image (Lu, 2015).

The 2D wavefield transformation is performed by summing over the subset of time traces that satisfy Eq. (4) and can be expressed as (Park, 2011):

$$E(c,f)=\frac{\left|\sum_{j=n_{near}}^{n_{far}} e^{i\phi_j}F_j(f)\right|}{(n_{far}-n_{near}+1)} \qquad (5)$$

where n_{near} and n_{far} are indices of the time traces that match closely the near offsets x_{near} and far offset x_{far} respectively. The term of $(n_{far} - n_{near}+1)$ in Eq. (5) is used for the purpose of normalization.

In signal processing, an overtone image is obtained by the traditional MASW method via Eq. (3) first. From the dispersion pattern of the image an initial dispersion curve can be determined and it is used to estimate wavelengths at all frequencies. At each frequency, near offset and far offset are then calculated using Eq. (4). In other words, near offset and far offset are unique at each frequency and self-adaptive to the corresponding wavelength. The final overtone image is obtained by Eq. (5), where the final dispersion curve is determined.

In order to sample time traces sufficiently to avoid spatial aliases, a variable sensor spacing configuration was implemented in the study. It should be mentioned that in this study "multiple channels" was achieved by moving a single accelerometer multiple steps with repeated impacts generated by the shaker at the same location. Strictly speaking this kind of data acquisition technique can be classified as a multichannel simulation with one receiver (MSOR) method that was first developed by Ryden, et al. (2001) for pavement assessments at kHz frequencies. Since the central concepts and signal processing algorithms of the MSOR method are essentially the same as those of MASW methods, the term "MASW method" is used throughout the paper. In the current geometric sensor configuration, the spacing for the first 120 sensor steps is set to be 0.5 cm and the next 40 steps start with 1 cm spacing followed by 1 cm incremental spacing for each subsequent step. The distance that the accelerometer covers grows rapidly after the spacing is increased 1 cm every step, much faster than that of equal spacing, thus efficiently reducing the number of sensors. The first sensor position is set to be 20 cm away from the shaker. This sensor geometric configuration allows for sufficiently sampling the entire frequency range without violating Nyquist sampling theorem.

For detailed description of the self-adaptive MASW method, the interested readers may refer to the literature (Lu, 2015).

Experimental setup

The experimental setup for the high-frequency MASW method is shown in Fig. 1. An electrodynamic shaker (Vibration Test System, Model VG-100-6) was used as a seismic source that provided 110 pounds of peak force and a frequency range from DC to 6500 Hz. The shaker was operated in a frequency-sweeping mode to generate a chirp signal with an adjustable frequency range to excite sufficiently high frequency components of surface waves. The shaker has an advantage over impulsive sources such as sledgehammers and weight drops that can only generate fixed and low frequency components.

Figure 1. The experimental setup for the high frequency MASW method.

A 15 lb. metal cylinder was attached to the top of the shaker to enhance energy transferring into the ground. An accelerometer (PCB Piezotronics, Model 352B, 1V/g, 2 to 10k Hz) was used as a vibration sensor. The accelerometer was mounted with a 1.5 cm metal needle that was inserted into the soil surface to facilitate the sensor placement and to enhance contact and energy coupling. The surface vertical vibrations were measured by consecutively placing the accelerometer onto the ground at multiple locations along a straight line. For each step of the accelerometer movement, the shaker excited four chirp signals with overlapped frequency ranges and the accelerometer recorded one set of four readings. Multiple measurements were made using the variable sensor spacing configuration, as described in the previous section. Due to Nyquist sampling theorem and the need to distribute seismic energy uniformly over the entire frequency range, the source frequency is divided into four overlapping frequency ranges: for example, 40-180 Hz, 160-500 Hz, 450-1200 Hz, and 1000-1600 Hz, representing low frequency (LF), middle frequency (MF), high frequency (HF), and extra high frequency (XF) bands. The corresponding chirp durations are 5.0 s, 2.4 s, 2.0 s, and 1.6 s, with sampling frequencies of 10 kHz, 20 kHz, 25 kHz, and 30 kHz, respectively. These parameters may vary a little from test to test. Figure 2 shows a typical received signal gather of 30 time traces.

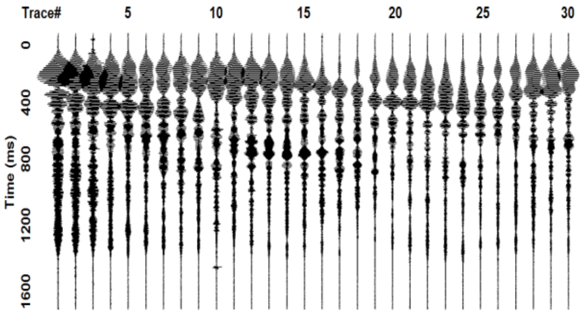

Figure 2. The time traces of detected surface vibrations excited by a chirp source signal.

It was found that at high frequencies, direct air wave may dominate over the surface seismic wave, manifesting itself as a non-dispersion line with phase velocity of 340 m/s in an overtone image. To eliminate the influence of direct air, a wooden barrel with embedded foams was used to cover the shaker and to damp the air wave.

A program written in LabVIEW (National Instruments, Inc.) was used to communicate between a laptop computer and instruments for chirp signal generation, data acquisition, 2-D wavefield transformation, and dispersion curve determination. A software package, SurfSeis 3 (Version 3.0.6.4, Kansas Geological Survey) was used for inversion process. For the case of dry sealed/ crusted soil, a simple and approximated inversion technique that was first proposed by Tokimatsu, et al., 1992 was employed for inversion process at high frequencies.

RESULTS AND DISCUSSIONS

In order to compare the MASW results between crusted soil and non-crusted soil, the study consisted of three field tests at three different soil conditions. The first test was conducted on 7 May 2015 following the development of surface crust (see Fig. 3). The second was conducted on 18 September, 2015 and involved measurements on the original crust area followed by measurements on a freshly tilled area. The third test on 3 November 2015 was at the same test site as the second which included the crust and tilled areas. Between the second and third tests, the test site experienced several days of low intensity rainfall that did not induce crusting of the tilled area but served to moisten the soil profile.

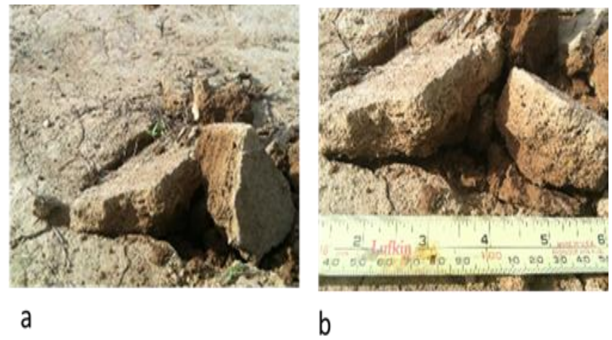

Figure 3. Photos of surface crust at the test site

.

Rainfall and soil property patterns

In soils with low clay and high silt content with low aggregate stability, such as the loess soil in this study, antecedent moisture content and wetting rate do not play an important role (Bradford and Huang, 1992; Mamedov et al., 2001). Instead, the kinetic energy of the rain determines seal formation. Between the time of tillage and acoustic measurements, the surface experienced 15 storm events, defined as rainfall of greater than 1.27 mm and six hour or more interval without rainfall plus six small (<1.27 mm) events. The 15 storm events totaled 199.4 mm with a range of kinetic energy contents from 0.27 to 8.80 MJ ha^{-1} and maximum 5 minute intensities of 3.0 to 73.2 mm hr^{-1}. The mean kinetic energy content was 2.19 MJ ha^{-1} mm^{-1} and mean 5 minute intensity of 20.32 mm hr^{-1}. Jakab et al. (2013) noted that a single storm was sufficient to cause crusting. The maximum 30 minute erosion index (EI30) was 396.4 MJ mm ha^{-1} hr^{-1}. Such rainfall intensities from multiple events are clearly capable of creating surface crust in this low OM, medium textured soil. The six minor events totaled 4.6 mm rainfall with a kinetic energies of < 0.20 MJ ha^{-1}. Nciizah and Wakindiki (2014) noted that it is the inter-storm drying periods that serve to increase soil crusting which is consistent with the natural rainfall events with inter-storm drying conditions used in this study. Following the measurements on the freshly tilled area on 18 September, 2015, seven rainfall events occurred, totaling 55.6 mm. These served to wet the soil without reforming the crust due to the low intensities. The maximum 5 min intensity during this period ranged from 3.0 to 24.4 mm h^{-1} with kinetic energies from 0.25 MJ ha^{-1} to

3.85 MJ ha^{-1}. The maximum EI30 was just 39.8 MJ mm ha^{-1} hr^{-1}. An additional seven minor events occurred that totaled 3.3 mm and with kinetic energies of < 0.08 MJ ha^{-1}. These events between the second and third tests did not create any visible evidence of crusting in the tilled area.

These high intensity-high kinetic energy rains prior to the first test created a soil crust as evidenced by the physical properties of the surface. The soil crust is clearly seen in Table 1 by the higher bulk density of the surface (0-1 cm) which averaged 1.615 Mg m^{-3} as compared to 1.365 Mg m^{-3} immediately below the crust (2-5 cm). Jakab et al. (2013) observed a 15 to 40% increase in bulk density depending upon the type of crust formed. Remley and Bradford (1989) observed surface seals with soil strength ranging from 14 to 43 kPa for medium-textured soils such as in this study. In contrast, they did not observe crust on a sandy loam and clay soil with soil strengths of 11 kPa and 6 kPa, respectively. We observed soil shear strengths of 424 kPa at the surface curst (0-1 cm) and a decrease to 83 kPa below the crust (2-5 cm). The soil penetration resistance, Table 2, did not indicate a strong crust but it did suggest that the crust was deeper than the immediate surface and likely extended to 8 cm with a peak at 5 cm.

The bulk density remained essentially unchanged (1.643 Mg m^{-3}) at the surface (0-1 cm) at the time of the second test. The major differences were that the bulk density increased dramatically in the 2-5 cm depth suggesting that the crust was deeper than the immediate surface, the soil was drier than at the first test, and the soil penetration resistance increased. The bulk density of the 2-5 mm depth increased by 36.5% and the gravimetric moisture content decreased from an average of 18.4% to 14.9% over the 0-30 cm depth. The soil penetration resistance exhibited dramatically increased values from the surface to about 10 cm with a peak at 5 cm. However, the shear strength of the soil profile was unchanged. The effect of tillage is clearly seen in the bulk density, shear strength, and penetration resistance (Tables, 1 and 2). The bulk density decreased by 19.2 and 40.2% for the 0-1 and 2-5 cm depths, respectively for the tilled area. The shear strength of these depths decreased even more dramatically to essentially zero for the tilled area. In addition, the penetration resistance of the upper 10 decreased substantially particularly in the upper 3 cm.

Table 1. Results of soil characterization involving soil moisture content, bulk density and shear strength analysis.

	7 May Crust Area			18 Sept. Crust Area			18 Sept Tilled Area			3 Nov. Crust Area		3 Nov. Tilled Area	
Depth (cm)	Moisture content (g/g %)	Bulk density (g/cm^3)	Shear strength (kPa)	Moisture content (g/g %)	Bulk density (g/cm^3)	Shear strength (kPa)	Moisture content (g/g %)	Bulk density (g/cm^3)	Shear strength (kPa)	Moisture content (g/g %)	Shear strength (kPa)	Moisture content (g/g %)	Shear strength (kPa)
0-1	5.9	1.615	424	7.2	1.642	424	4.8	1.327	0				
2-5	16.5	1.365	83	6.6	1.863	82	11.0	1.115	6	19.2	92	23.7	3
10	18.5		142	15.9		176	15.0		164	20.3	223	26.1	17
20	25.4		167	22.1		200	22.0		142	25.8	152	27.8	128
30	26.0		170	22.9		250	22.0		169	25.9	205	28.0	160
40	25.8		173							23.7	250	27.7	198

Table 2. Results of the penetrometer test

Depth (cm)	Penetrometer resistance (kPa)				
	7 May Crust Area	18 Sept. Crust Area	18 Sept Tilled Area	3 Nov. Crust Area	3 Nov. Tilled Area
0	569	2034	35	630	70
3	1631	2812	59	1523	164
5	2418	2957	651	2048	141
8	2325	2990	748	2547	176
10	1811	2634	1786	2789	464
13	1739	2491	2191	1680	881
15	1797	2336	2168	1495	1132
18	1832	2535	2203	1762	1371
20	1893	2550	2179	1882	1439
23	1739	2718	2610	1966	1465
25	2013	2920	2610	1971	1657
28	2118	3374	2681	2596	1654
30	2182	3351	3253	2932	1654
33	2240	3325	3351	3613	1917
36	2371	3025	3016	3717	2048
38	2514	3145	2920	3768	2266
41	2383	3456	3337	3431	2130
43	2510	3576	3093	3789	1952
46	2559	max	3497	4500	2348

The bulk density was not measured at the time of the third test but the shear strengths and penetration resistance were almost identical at the upper two depths to the original measurements even though the soil was considerably wetter. The effect of tillage was still clearly seen in both the shear strength and penetration resistance measurements. The moisture content increased to 22.8% over the 0-30 cm depth for the crust area and was even higher, 26.4% for the tilled area. The effect of the crust on infiltration is clearly seen in that the profile (0-30 cm) moisture content increased by 53% from the seven rainfall events between 18 September and 3 November for the crust area and by 77% for the tilled area.

Acoustic/seismic properties

As mentioned before, the MASW tests were conducted under different soil conditions. For the tests on dry crusted soils conducted on 7 May and 18 September the MASW results exhibit similar dispersion patterns. For the sake of brevity, only the results on 18 September are presented. For the test on the freshly tilled soil made on 18 September, the MASW data cannot generate reliable and meaningful overtone image. It was speculated that the tillage altered soil structure and the loose soil aggregates increased heterogeneity that scattered the acoustic wave propagation, especially at higher frequencies. Also it is well-known that the disturbed soil requires certain period of time to stabilize. Due to these reasons, the dispersion curves of the freshly tilled soil cannot be well determined and the corresponding MASW data was thus discarded. The third test was conducted under a moist soil condition after several days of low intensity rainfall that did not induce crusting of the tilled area. It was believed that the moist soil condition dispersed soil aggregates and created a lateral homogenous condition that facilitated the acoustic wave propagation. In this study, the overtone images of four frequency bands for the three representative soil conditions were shown in Fig. 4 (a)-(d), Fig. 5 (a)-(d) and Fig. 6 (a)-(d), representing dry sealed/crusted soil on 18 September, 2015, moist sealed/crusted soil on 3 November, 2015, and moist tilled soil on 3 November, 2015. In Figs. 4-6, the y-axis, the x-axis, and the color denote the phase velocity, the frequency, and the value of $E(c, f)$ in Eq. (5), respectively. The color bars are auto-scaled to enhance the contrasts of the images. The multipliers in Eq. (4) were set to be $k_{near} = 0.2$ and k_L=2-2.5 for most frequency bands, except for LF band where k_{near} is set to be 0.7 to avoid near field effects (Lu, 2015). From these overtone images, the dispersion patterns of Rayleigh waves of different modes can be recognized from their color patches.

Fig.4 (a), Fig. 5(a), and Fig. 6(a) show typical dispersive characteristic of the fundamental mode of Rayleigh waves, manifesting a monotonously decreasing phase velocity with frequency. Normally this dispersive behavior predicts that at this low frequency band with the corresponding wavelengths and penetration depths, the S-wave velocity increases with depth, a situation of the so-called normal soil profile (Gucunski and Woods, 1992; Tokimatsu, et al., 1992). This prediction can be later confirmed by the inversion results. In Fig. 4 (b), Fig. 5(b), and Fig. 6(b) the fundamental mode of Rayleigh waves can be well identified from 165 Hz to 500 Hz with the phase velocities less than 200 m/S. Careful examination of the dispersion pattern in Fig. 4(b) reveals that from 165 Hz to 280 Hz the phase velocity decreases with the frequency, following the trend of the normal dispersive behavior of Fig. 4 (a), and from 280 Hz to 500 Hz, however, the phase velocity increases slightly with frequency, suggesting an inversed soil profile, where the S-wave velocity decreases with depth. In Fig. 4(b) and Fig. 6(b), one observes very strong higher modes of Rayleigh waves, manifesting as higher phase velocities than those of the fundamental mode. The appearance of the high modes in the overtone images indicates that the fundamental mode doesn't dominate over the higher modes of Rayleigh waves. As pointed out by many researchers (Gucunski and Woods, 1992; Tokimatsu, et al., 1992; Park, et al., 1999; Xia, et al., 2003; Park, et al., 2005; Boaga, et al., 2014) the generation of higher modes is associated with sensor location, irregular soil layering, and lateral heterogeneity. Another possibility of these seemly higher modes may due to the influence of direct air wave, suggesting that a better air wave insulation device should be used in the future study. Due to this concern, the higher modes with the phase velocities higher than 300 m/s were ignored in the later dispersion curve determination and inversion processes. In Fig. 4(c), the dispersion curve of the fundamental mode can be determined at frequency range from 450 Hz to 1100 Hz. In this frequency range, one observes a continuously increasing trend in the phase velocity, manifesting strong velocity reversal effect. The dispersion curve can be identified from 1000 Hz to 1600 Hz in Fig. 4(d), maintaining a high phase velocity value around 180 m/s with slight declining velocity after 1400 Hz. It is noticed that no "direct air wave"-like higher modes appears in this frequency range. This may due to the fact that as frequency is increased up to kHz with shorter wavelength, the surface waves may only propagate along the rigid layer, leading to the dominance of the fundamental mode of Rayleigh waves. In this situation, Rayleigh wave propagation will reduce to Lamb wave propagation (Ryden, et al., 2001; 2004; Ryden and Lowe, 2004). At sufficient high frequency, the dispersion curve of the first high mode merges into the one of the fundamental mode. In Fig. 5(c)-(d), the fundamental mode can be identified from 450 Hz to 1600Hz and the second and the third higher modes occurred at frequencies above 800 Hz. In Fig. 6(c), the fundamental mode can be recognized from 460 Hz to 860 Hz with the phase velocities less than 90 m/s. The second higher mode can be identified from 530 Hz to 1600 Hz in Fig. 6(c)-(d). The third higher modes appeared in Fig. 6(c)-(d) but they were not included in the later inversion process for the sake of simplicity.

Following the above mode interpretations, the dispersion curves including both the fundamental and higher modes were extracted from Figs. 4-6 by picking up the highest intensity in the dispersion patterns. The dispersion curves of the four frequency bands were combined and plotted in Fig. 7(a)-(c). A software package TableCurve 2D (SYSTAT software Inc.) was used for curve fitting the dispersion curves (not shown in Fig. 7) and the regressed curves were used for the inversion processes.

The one third wavelengths at certain frequencies were calculated using the regressed dispersion curve of the fundamental mode and also plotted **in Fig. 7** as dashed curves. From these one third wavelength curves the exploration depth at each frequency can be estimated (Tokimatsu, et al., 1992). As seen in **Fig. 7(a)**, for example, the sampling depth of Rayleigh waves decreases nonlinearly with frequency. The most drastic variations occur at low frequencies ranging from 50 Hz to 300 Hz with depths changing from 1.5 m to 0.1 m. At frequencies ranging from 300 Hz to 1600 Hz, sampling depths decrease slightly with a depth variation from 0.1 m to 0.035 m. Such a varying trend of sampling depth with frequency also leads to the usage of the variable sensor spacing configuration to avoid spatial aliases. Detailed explanation can be found in the literature (Lu, 2015).

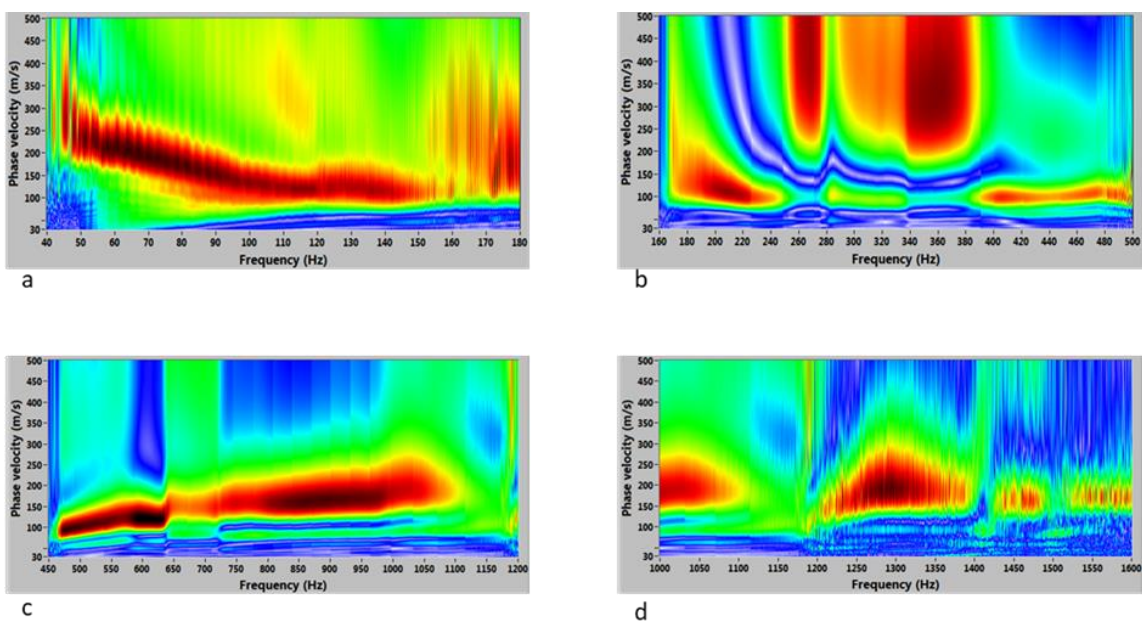

Figure 4. Overtone images of dry sealed/crusted soil on 18 September for (a) LF band, (b) MF band, (c) HF band, and (d) XF band, respectively.

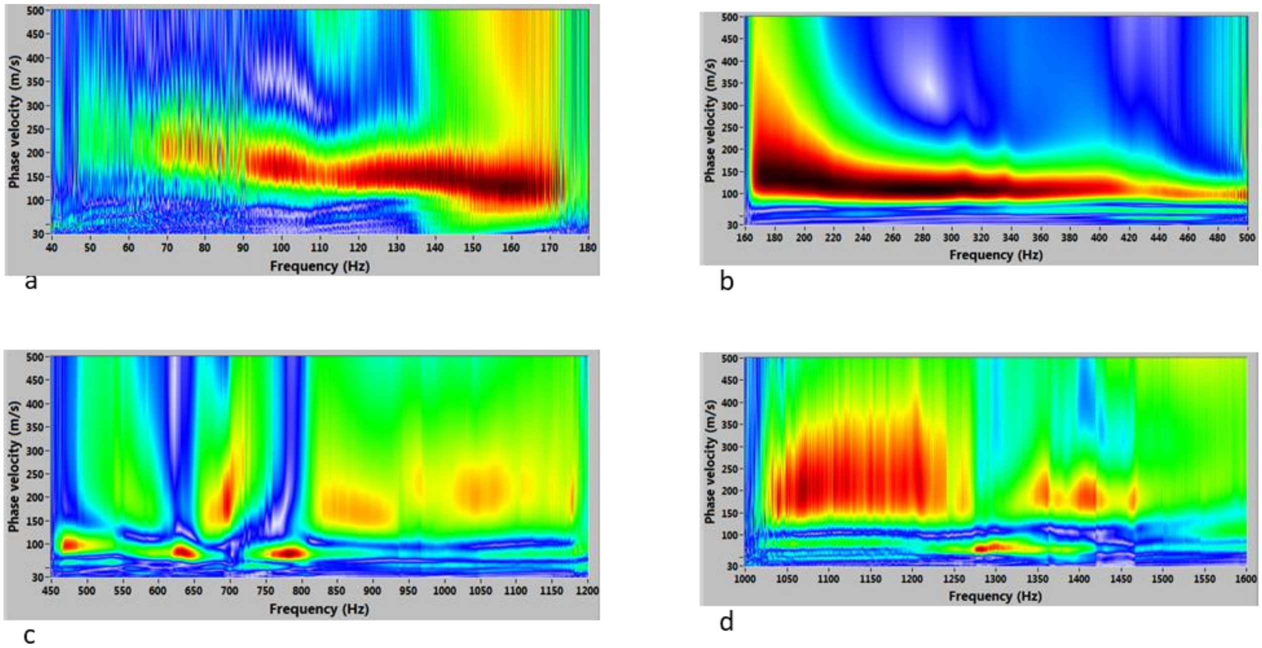

Figure 5. Overtone images of soil on 3 November from moist sealed/crusted area for (a) LF band, (b) MF band, (c) HF band, and (d) XF band, respectively

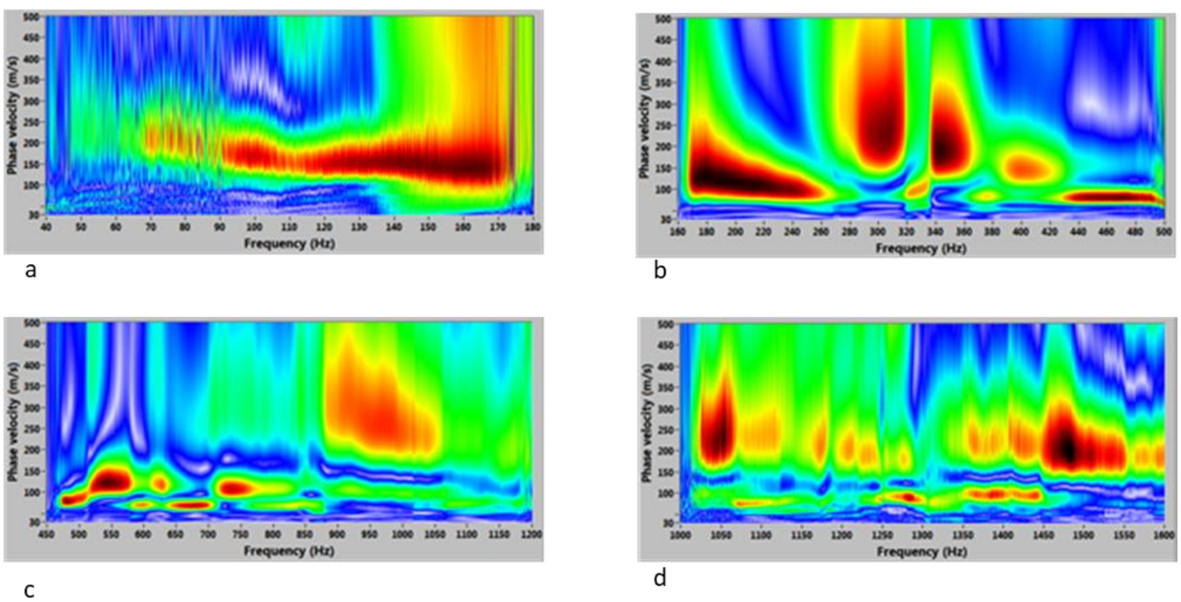

Figure 6. Overtone images of soil on 3 November from moist tilled area for (a) LF band, (b) MF band, (c) HF band, and (d) XF band, respectively.

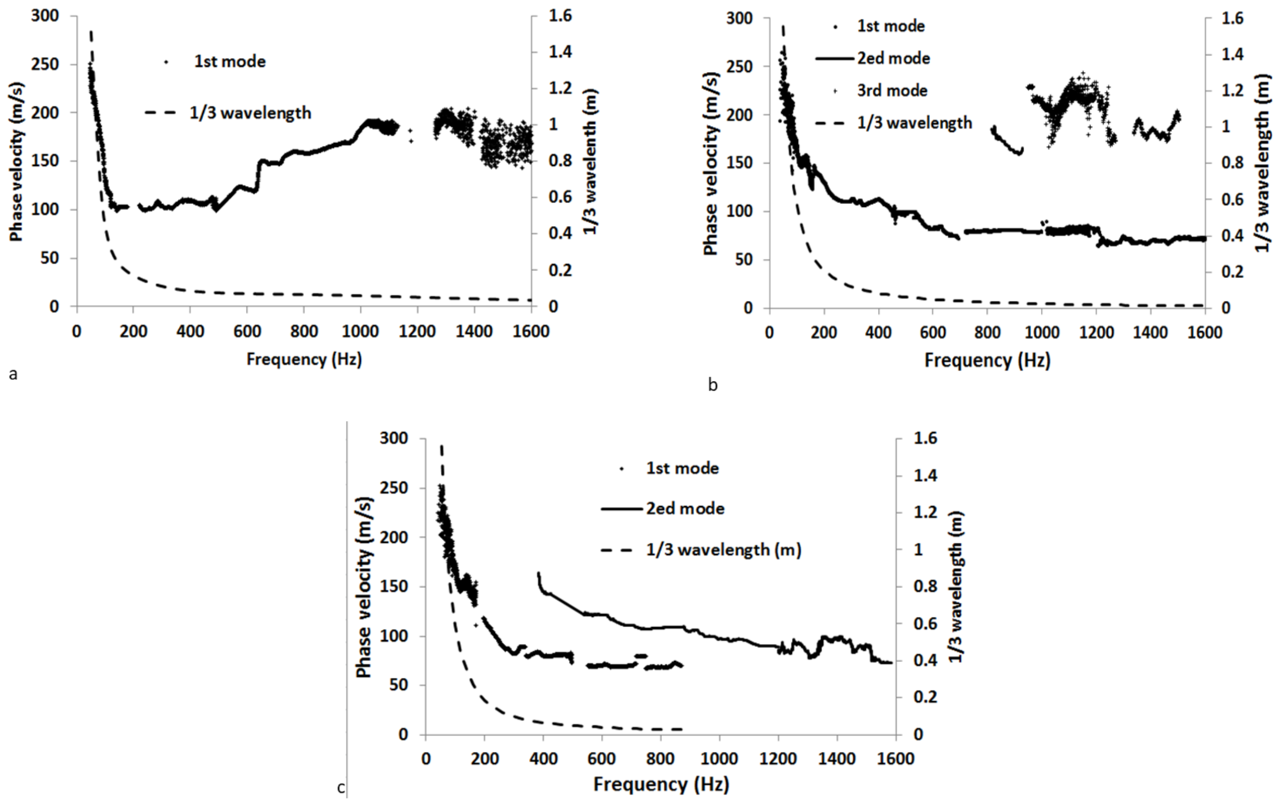

Figure 7. The combined dispersion curves for the fundamental mode(solid dots), the second higher mode (solid curves), the third higher mode ("+" dots), and the one third wavelengths (dashed curve) versus frequency for (a) 18 September dry sealed/crusted soil, (b) 3 November moist sealed/crusted area, and (c) 3 November moist tilled area, respectively.

Currently, the commercial available inversion algorithms, like SurfSeis 3, cannot handle very well the situation of a high velocity layer (HVL) overlaying low velocity layer (LVL) (Lu, 2014a), although some efforts have been made, attempting to solve the problem (Pan, et al. 2013). In this study, we employed a hybrid method to determine soil profile of sealed/crusted soil. First, we ran SurfSeis 3 inversion process to determine a soil profile using the dispersion curve only at frequency range from 50 Hz to 500 Hz. The soil profile in terms of the shear wave velocity with 20 layers and variable thicknesses is plotted in **Fig. 8,** where the stage-like lines (20 segments) display the shear velocity as a function of depth. The inversion yielded a root mean square (RMS) error of 5.6 m/s between the measured and inverted dispersion curves.

Secondly, for inverting the dispersion curve above 500 Hz, we adopted a simple and approximate technique proposed by Tokimatsu, et al., 1992, which assumes that the S-wave velocity equals to the phase velocity and the effective exploration depth is equal to one third of wavelength. The technique was slightly modified from the original one in which the shear wave velocity is equal to 1.1 the phase velocity. In this study, we found that by setting the shear wave velocity equal to the phase velocity yielded the best agreements between the results of the simple inversion and SurfSeis 3 inversion. To demonstrate the effectiveness of the simple inversion method, we compared the soil profile derived from the simple method with the one taken from SurfSeis 3 algorithm using the dispersion curve frequency range from 50 Hz to 500 Hz. As shown in **Fig. 9**, both the inversion approaches yield identical soil profiles and they are superimposed each other at depths below 10 cm.

At frequencies from 500 Hz to 1600 Hz, the simple inversion method yielded a high velocity zone with very thin thickness of about 7 cm, plotted as the round dots in **Fig. 9**.

The soil profile obtained on dry crusted soil on 18 September from the simple inversion approach features three distinctive zones. The top soil from the surface to the depth of 10 centimeters manifests a high velocity zone indicating a hard layer. The elevated S-wave velocity of the zone could both be caused by rainfall mechanical impacts that increase the rigidity and reduce the porosity of the surface soil and due to drying between events which decreases water content and increases soil suction. Combined these processes produce a crusting and sealing effect (Leary, et al., 2009). As mentioned in the literature (Lu and Sabatier, 2009; Lu, 2014a), the increased soil suction leads to an increment of the effective stress, and consequently results in higher velocity. Immediately after the rigid top layer, a zone of soft soil, featuring as sharp decreasing in the S-wave velocity, can be found from the depths of 0.1 m to 0.3 m, showing an opposite hydrological effect on the seismic velocity, i.e. the increased moisture content (as evidenced in Table 1) softens the soil and causes the decrease in the S-wave velocity. The third zone, from the depths of 0.3 m to 1.6 m, exhibits a gradually increasing trend in the S-wave velocity with depth because of the increased overburden pressure.

Based on the above discussions of the soil profile as shown in Fig. 9, the top rigid layer due to soil surface sealing and crusting was therefore identified.

For 3 Novermber conditions of both seal/crust and tilled areas (moist non-disturbed soil and moist tilled soil, respectively) normal soil profile conditions were generally established as seen in Tables 1-2. Therefore, SurfSeis 3 was used to invert the soil profile using the regressed dispersion curves of both the fundamental mode and higher modes in Fig. 7 (b) and (c) over the entire frequency range. It is worthy to mention that the inclusion of the higher modes stabilizes the inversion process and increases the accuracy of inverted soil profile (Xia, et al. 2003, Lu, et al., 2014). The inverted two soil profiles in terms of the shear wave velocity with 20 layers and variable thicknesses are plotted in Fig. 10. The inversions yielded RMS errors of 3.9 m/s and 7.8 m/s respectively.

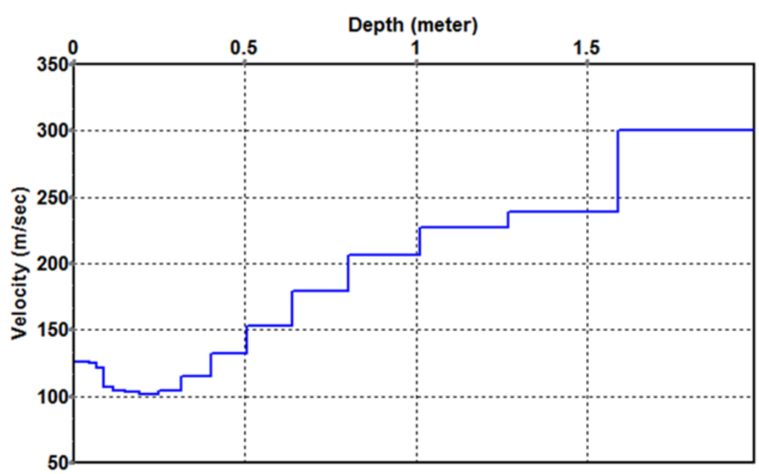

Figure 8. The soil profile for sealed/crusted soil on 18 September, where the stage-like lines display the S-wave velocity as a function of depth.

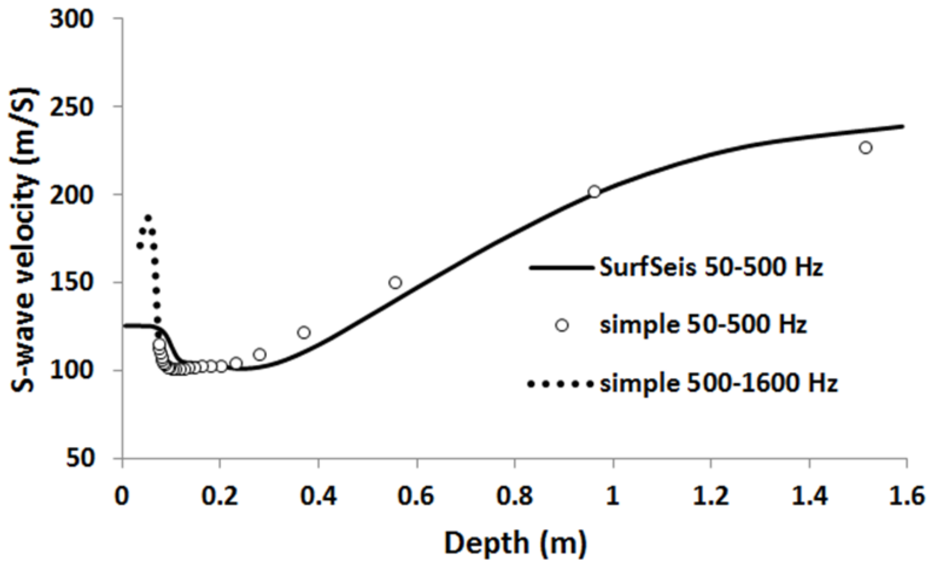

Figure 9. The inverted soil profiles in terms of the shear wave velocity, where the solid curve and circled dots represent the soil profiles using the dispersion curve at frequencies from 50 Hz to 500 Hz inverted by both SurfSeis 3 and the simple inversion techniques respectively, and the round dots display the soil profile using the dispersion curve at frequencies above 500 Hz inverted by the simple inversion method

The soil profiles as shown in Fig. 10 (a)-(b) represent overall normal soil profiles, as we anticipated. Fig. 10 also reveals subtle structural differences in the soil profiles between the moist seal/crusted area and the moist tilled soil. For the moist tilled soil, the soil profile shows a monotonously increasing tendency with depth, whereas the soil profile of moist seal/crusted soil exhibits a slightly raised high velocity layer at the depths between 10 cm to 30 cm, followed by a normal profile starting at a relatively low velocity.

As compared the soil profiles taken from the invasive methods as tabulated in Tables 1-2 with those inverted from the MASW tests as shown in Fig. 9 and Fig. 10, they present the same depth-dependent tendencies, especially in revealing the high velocity and high mechanical strength zone of the top sealed/crusted soil, as well as the subtle structural difference between the moist non-disturbed and moist tilled soils. In a recent study (Gao, et al., 2013), a linear relationship between shear wave velocity and penetrometer resistance has been established, therefore further supporting our results.

It should be pointed out that the present MASW method requires manually moving the accelerometer at multiple locations, which is a labor-intensive and technically challenging task. To facilitate the field test, an automated MASW system has been developed, in which a laser-Doppler vibrometer (Polytec PI, Inc., Model PDV 100, frequency range: DC-22 kHz) serves as an optical non-contact sensor to measure surface vibrations. The laser-Doppler vibrometer is driven by a stepper motor controlled by a computer and its movement can be set arbitrarily small to achieve very high spatial resolution (Lu, 2014a). This system will be used for the soil surface sealing and crusting study in the future.

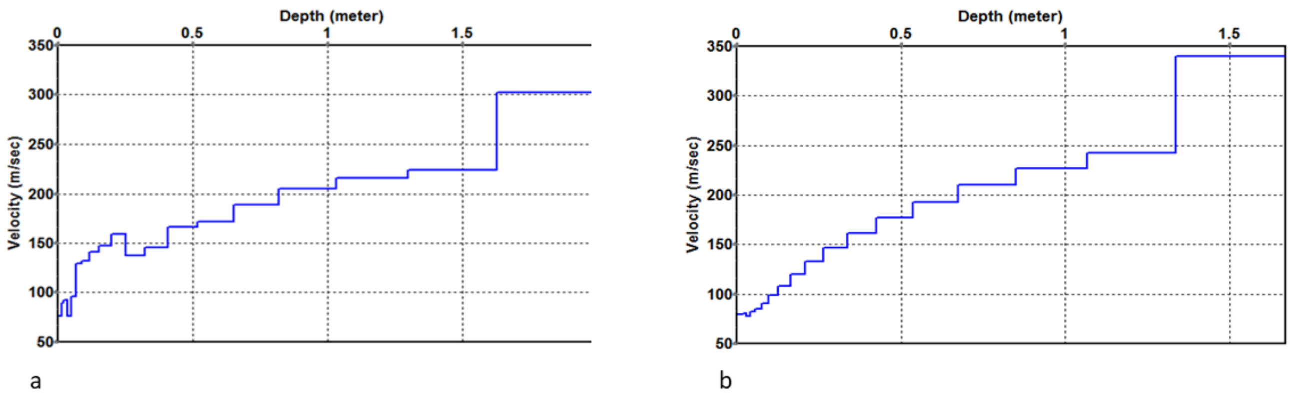

Figure 10. The soil profiles for 3 November moist sealed/crusted area on left and moist tilled area on right.

CONCLUSIONS

A self-adaptive high-frequency MASW method with a variable sensor spacing configuration has been developed for studying soil surface sealing and crusting. The MASW tests were conducted on both a naturally formed sealed/crusted soil and a non-sealed/non-crusted soil artificially created by tillage. The soil profiles in terms of the shear wave velocity were measured non-invasively up to 1.6 meters deep below the surface. On the crusted soil, three distinctive zones were identified, representing a high velocity surface seal/crusting thin layer, a moist and soft middle zone, and a progressively increased velocity region below caused by increased overburden pressure with depth. On the tilled soil without the presence of top rigid layer, the shear wave velocity soil profile exhibited a monotonously increasing tendency with depth. Soil core samples, shear vane and penetration tests were compared with the observations from the MASW method. The results from both the MASW method and soil characterizations were in good agreement, validating that the current MASW method can be used in situ to evaluate soil sealing and crusting layer as well as to explore the soil profile in the vadose zone.

ACKNOWLEDGEMENTS

This work was supported by the U. S. Department of Agriculture under Specific Cooperative Agreement 58-6408-7-234.

LITERATURE CITED

Agassi, M., I Shainberg, and J Morin. 1981. Effect of electrolyte concentration and soil sodicity on infiltration rate and crust formation. Soil Sci. Soc. Am. J. 45:848-851.

Agassi, M., J Morin, and I Shainberg. 1985. Effect of electrolyte concentration and soil sodicity on infiltration rate and crust formation. Soil Sci. Soc. Am. J. 49:186-190.

Alzate-Diaz, S.P., Popovics, J.S., 2009. Application of MASW to characterize pavement top layer. In Proceedings: Non-Destructive Testing in Civil Engineering, Jun-Jul, 2009, Nantes, France.

Ben-Dor, E, N Goldlshleger, Y Benyamini, M Agassi, and DG Blumberg. 2003. The spectral reflectance properties of soil structural crusts in the 1.2 to 2.5-um spectral region. Soil Sci. Soc. Am. J. 67:289-299.

Boaga, J., Vignoli, G., Deiana, R., and Cassiani, G., 2014. The influence of subsoil structure and acquisition parameters in MASW mode mis-identification. Journal of Environmental and Engineering Geophysics, 20, 87-99.

Bradford JM, Huang CH. 1992. Mechanisms of seal formation: Physical components. In *Soil Sealing: Physical and Chemical Processes*, Sumner ME, Stewart BA (eds). Lewis: Boca Raton, FL, p. 55–72.

Bresson, LM, CJ Morgan, and S Assouline. 2004. Using bulk density profiles from X-radiography to examine structural crusts models. Soil Sci. Soc. Am. J. 68:1169-1176.

Brown, LC and GR Foster. 1987. Storm erosivity using idealized intensity distributions. Trans ASAE 30(2):379-386.

De Jong, SM, EA Addink, R van Beek, D Duijsings. 2009. Mapping of soil surface crists using airborne hyperspectral HyMap imagery in a Mediterranean environment. Anais XIV Simpòsio Brasileiro de Sensoriamento Remoto, Natal, Brasil, INPE p. 7725-7732.

Foti, S., 1999. Multistation methods for geotechnical characterization using surface waves. PhD dissertation. Politecnico di Torino, Italy.

Gao, W., Watts, C.W., Ren, T., Shin, H.-C., Taherzadeh, S., Attenborough, K., Jenkins, M., Whalley, W.R., 2013. Estimating penetrometer resistance and matric potential from the velocities of shear and compression waves. Soil Science Society of America Journal, 77, 721-728.

Grandjean, G., Leparoux, D., 2004. The potential of seismic methods for detecting cavities and buried objects: experimentation at a test site. Journal of Applied Geophysics, 56, 93-106.

Gucunski, N. and Woods, R.D., 1992. Numerical simulation of the SASW test. Soil Dynamics and Earthquake Engineering, 11, 213-227.

Hussein, MH, MM Awad, and AS Abdul-Jabbar. 2010. Effect of surface crust on rainfall infiltration in an aridisoil in Northern Iraq. Eutopean Water 32:25-34

Imai, T., and Tonouchi, K., 1982, Correlation of N-value with S-wave velocity: in Proceedings: 2nd European Symposium on Penetration Testing, 67-72.

Ivanov, J., Miller, R.D., Lacombe, P., Johnson, C.D., Lane Jr., J.W., 2006. Delineating a shallow fault zone and dipping bedrock strata using multichannel analysis of surface waves with a land streamer. Geophysics, 71, A39-A42.

Ivanov, J., Miller, R.D., Tsoflias, G., 2008. Some practical aspects of MASW analysis and processing. In Proceedings of 21st SAGEEP (2008), Philadelphia, PA., Apr. 6-10, 2008.

Ivanov, J., Park, C.B., Miller, R.D., Xia, J., 2000. Mapping Poisson's ratio of unconsolidated materials from a joint analysis of surface-wave and refraction events. In Proceedings: Symposium on the Application of Geophysics to Engineering and Environmental Problems, Feb., Arlington, VA.

Jakab, G, T Nemeth, B Csepinszky, B Madarasz, Z Szalai, and A Kertesz. 2013. The influence of short term soil sealing and crusting on hydrology and erosion at Balaton Uplands, Hungary. Carpathian J. Earth and Environ. Sci. 8:147-155.

Lane Jr., J.W., Ivanov, J., Day-Lewis, F.D., Clemens, D., Patev, R., Miller, R.D., 2008. Levee evaluation using MASW: Preliminary findings from the Citrus Lakefront Levee, New Orleans, Louisiana. In Proceedings: Symposium on the Application of Geophysics to Engineering and Environmental Problems, Apr. 2008. Philadelphia, PA., 1-10.

Leary, D., DA DiCarlo, and CJ Hickey. 2009. Acoustic techniques for studying soil-surface seals and crusts. Ecohydrology 2:257-262.

Lee, SS, CJ Gantzer, AL Thompson, SH Anderson, RA Ketcham. 2008. Using high-resolution computed tomography analysis to characterize soil-surface seals. Soil Sci. Soc. Am. J, 72(5):1478-1485.

Lu, Z., 2014a. Feasibility of using a seismic surface wave method to study seasonal and weather effects on shallow surface soils. Journal of Environmental & Engineering Geophysics, DOI: 10.2113/JEEG19.2.71, Vol.19, 71–85.

Lu, Z., 2014b. Self-adaptive method for high-frequency dispersion curve determination. In Proceedings of the Symposium on the Application of Geophysics to Engineering and Environmental Problems (SAGEEP 2014), Boston, MA., Mar. 16-20, 2014.

Lu, Z., 2015. Self-adaptive method for high frequency seismic surface wave method. Journal of Applied Geophysics. 121, 128-139, DOI:10.1016/j.jappgeo.2015.08.003.

Lu, Z., and Sabatier, J.M., 2009, Effects of soil water potential and moisture content on sound speed: Soil Science Society of America Journal, 73, 1614-1625.

Lu, Z., Wilson, G.V., Hickey, C.J., 2014. Imaging a soil fragipan using a high-frequency MASW method. In Proceedings of the Symposium on the Application of Geophysics to Engineering and Environmental Problems (SAGEEP 2014), Boston, MA., Mar. 16-20.

Mamedov, AI, I Shainberg, and GJ Levy. 2001. Irrigation with effluents: Effects of prewetting rate and clay content on runoff and soil loss. J. Environ. Qual. 30:2149-2156.

Miller, R.D., Xia, J., Park, C.B., Ivanov, J., 1999. Multichannel analysis of surface waves to map bedrock. The Leading Edge, 18, 1392-1396.

Nciizah, AD, and IIC Wakindiki. 2014. Rainfall pattern effects on crusting, infiltration and erodibility in some South African soils with various texture and mineralogy. Water SA 40:57-63.

Nciizah, AD, and IIC Wakindiki. 2015. Soil sealing and crusting effects on infiltration rate: A critical review of shortfalls in prediction models and solutions. Archives of Agronomy and Soil Sci. 61(9):1211-1230.

Pan, Y., Xia, J., Gao, L., Shen, C., and Zheng, C., 2013. Calculation of Rayleigh-wave phase velocities due to modes with a high-velocity surface layer. Journal of Applied Geophysics, 96, 1-6.

Park, C.B., 2011. Imaging dispersion of MASW data-full vs. selective offset scheme. Journal of Environmental and Engineering Geophysics, 16, 13-23.

Park, C.B., Miller, R.D., Xia, J., 1998b. Imaging dispersion curves of surface waves on multi-channel record. In Expanded Abstracts: 68th Society of Exploration Geophysics, 1377-1380.

Park, C.B., Miller, R.D., Xia, J., 1999a. Multichannel analysis of surface waves. Geophysics, 64, 800-808.

Park, C.B., Miller, R.D., Xia, J., 1999b. Detection of near-surface voids using surface wave. In Proceedings: Symposium on the Application of Geophysics to Engineering and Environmental Problems, Mar. Oakland, California, 281-286.

Park, C.B., Miller, R.D., Xia, J., 2001. Offset and resolution of dispersion curve in multichannel analysis of surface waves (MASW). In Proceedings of SAGEEP, Denver, CO, Mar. 4-7, 2001, SSM4.

Park, C.B., Miller, R.D., Xia, J., Ivanov, J., 2007. Multichannel analysis of surface waves (MASW) – active and passive methods. The Leading Edge, January 2007, 60-64.

Park, C.B., Miller, R.D., Xia, J., Sonnichsen, G.V., Hunter, J.A., Good, R.L., Burns, R.A., Christian, H., 2005. Underwater MASW to evaluate stiffness of water-bottom sediments. The Leading Edge, July, 2005, 724-728.

Park, C.B., Ryden, N., 2007. Offset selective dispersion imaging. In Proceedings of 2007 SAGEEP, Denver, CO., Apr. 1-5, 2007, 910-915.

Park, C.B., Xia, J., Miller, R.D., 1998a. Ground roll as a tool to image near-surface anomaly. Expanded Abstracts: 68th Annual International Meeting, Society of Exploration Geophysics, 874-877.

Remley, PA, and JM Bradford. 1989. Relationship of soil crust morphology to inter-rill erosion parameters. Soil Sci. Soc. Am. J. 53:1215-1221.

Römkens, MJM, RL Baumhardt, MB Parlange, FD Whisler, JY Parlange, and SN Prasad. 1985. Rain-induced surface seals:their effect on ponding and infiltration. Annales Geophysicae, 4:417-424.

Ryden, N., Lowe, M.J.S., 2004. Guided wave propagation in three-layer pavement structures. Journal of the Acoustical Society of America, 116, 2902-2913.

Ryden, N., Lowe, M.J.S., Cawley, P., 2009. Non-contact surface wave testing of pavements using a rolling microphone array. In Proceedings: Non-Destructive Testing in Civil Engineering, Jun-Jul, 2009, Nantes, France.

Ryden, N., Park, C.B., Ulrikens, P., Miller, R.D., 2004. Multimodal approach to seismic pavement testing. Journal of Geotechnical Engineering, 130, 636-645.

Ryden, N., Ulriksen, P., Park, C.B., Miller, R.D., Xia, J., Ivanov, J., 2001. High frequency MASW for non-destructive testing of pavements-accelerometer approach. In Proceedings: Symposium on the Application of Geophysics to Engineering and Environmental Problems, Denver, CO., RBA-5.

Sela, S, T Svoray, and S Assouline. 2012. Soil water content variability at the hillslope scale: Impact of surface sealing. Water Resour. Res. 48, W03522, doi:10.1029/2011WR011297

Singer MJ, and I. Shainberg. 2004. Mineral soil surface crusts and wind and water erosion. Earth Surf. Proc. And Land. 29:1065-1075.

Terzaghi, K., Peck, R.B., and Mesri, G, 1996, Soil mechanics in engineering practice: 3rd Ed. John Wiley&Sons, Inc. New York.

Tokimatsu, K., S. Tamura, and H. Kojima, 1992. Effects of multiple modes on Rayleigh wave dispersion characteristics, Journal of Geotechnical Engineering, 118, 1529-1543.

Valentin, C, and LM Bresson. 1992. Morphology, genesis, and classification of surface crusts in loamy and sandy soils. Geoderma 55:225-245.

Valentin, C. 1995. Sealing, crusting and hardsetting soils in Sahelian agriculture. Proc. 2nd

International Symposium on Sealing, Crusting and Hardsetting Soils: Productivity and Conservation. Australian Soc. Of Soil Science, Inc., Queensland, Australia. p 53-76.

Xia, J. Xu, Y., Miller, R.D., Ivanov, J., 2012. Estimation of near-surface quality factors by constrained inversion of Rayleigh-wave attenuation coefficients. Journal of Applied Geophysics, 82, 137-144.

Xia, J., Miller, R.D., Park, C.B., 1999. Estimation of near-surface shear-wave velocity by inversion of Rayleigh waves. Geophysics, 64, 691-700.

Xia, J., Miller, R.D., Park, C.B., Tian, G., 2002. Determining Q of near-surface materials from Rayleigh waves. Journal of Applied Geophysics, 51, 121-129.

Xia, J., Miller, R.D., Park, C.B., Tian, G., 2003. Inversion of high frequency surface waves with fundamental and higher modes. Journal of Applied Geophysics, 52, 45-57.

Xu, Y., Xia, J., Miller, R.D., 2005. Quantitative estimation of minimum offset for multichannel surface-wave survey with actively exciting source. Journal of Applied Geophysics, 59, 117-125.

Zhang, S.X., Chan, L.S., Xia, J., 2004. The selection of field acquisition parameters for dispersion images from multichannel surface wave data. Pure and Applied Geophysics, 161, 185-201.

Performance Comparison of Integrated Navigation System for Different Configurations

Umar Iqbal[1], Ashraf Abosekeen[2], Aboelmagd Noureldin[3], and Michael J. Korenberg[4]

[1]Electrical and Computer Engineering, Mississippi State University, Mississippi State, MS 39217, USA
[2]Electrical Engineering, Military Technical College, Cairo, Egypt,
[3]Electrical and Computer Engineering, Royal Military College of Canada, Queen's University, Kingston, Ontario, Canada,
[4]Electrical and Computer Engineering, Queen's University Kingston, Ontario, Canada

Corresponding Author: Umar Iqbal
E-mail: umar@ece.msstate.edu

https://doi.org/10.31753/IJRD28760138

ABSTRACT

Global positioning systems (GPS) position is determined from the distance measurements to four or more satellites with good geometry. Autonomous vehicles can utilize GPS navigation under open sky areas. However, GPS signal is degraded/denied in urban areas due to satellite signal blockage, multipath, and interference. A suite of multiple types of sensors with distinct strengths is required to achieve localization and positioning for autonomous operation. This paper is a review of a multi-sensor system with different configurations. Two types of the reduced inertial sensor system (RISS) were utilized: Odometer-based RISS/GPS and Frequency Modulated Continuous Wave Radar-based RISS/GPS. The Radar-based RISS/GPS navigation system performance is then evaluated by adding Magnetometer measurements. Fast Orthogonal Search (FOS) non-linear error modeling is employed for residual non-linear position errors modeling associated with the Magnetometer / Radar-based RISS /GPS positioning solution to improve the results further. During the availability of the GPS, FOS established the non-linear error model. In degraded/denied GPS environments such as urban canyons, the FOS-based non-linear error model operates in prediction mode to estimate the position errors associated with the Magnetometer / Radar-based RISS /GPS, thus providing improved positioning performance. These system configurations were evaluated for an actual road test trajectory for a GPS outage of 300 seconds to examine the performance. The results show that the system configurations play a significant role in improving positioning accuracy.

Keywords—Global Positioning System (GPS), MEMS sensors, Fast Orthogonal Search (FOS), Radio Doppler and Ranging (Radar), Reduced Inertial Sensors System (RISS), Kalman filter (KF*)*

INTRODUCTION

Autonomous vehicles have the potential to revolutionize our transportation systems by enhancing safety, bringing down crash rates, `and improving transportation system efficiency [1,2]. Land vehicle crashes are a leading cause of death, and 37,000 Americans were killed in crashes involving motor vehicles in 2018 [3]. 90% of crashes are due to driver error or misbehavior [1]. Autonomous vehicles have the potential to reduce risky driving behaviors like speeding, distraction, and impaired driving [1,3]. It will help to reduce the overall costs of crashes, including medical bills, vehicle repair, and lost work time. Autonomous vehicles can enhance productivity by allowing drivers to recapture time and help people with disabilities.

An essential requirement of an autonomous vehicle system is to have reliable positioning everywhere under all operational environments [4]. Global positioning systems (GPS) can provide positioning information. GPS receivers triangulate their position by measuring the distance using the travel time of radio signals to four or more satellites [5,6]. However, GPS signals suffer blockage, jamming and are affected by many factors such as multipath in urban canyons, quality of the receiver used, weather, and atmospheric conditions. Inertial navigation systems composed of gyroscopes and accelerometers are immune to external interference. However, the accuracy of MEMS sensors-based INS system deteriorates quickly due to sensors' scale factor instability, misalignment, and bias error drift [6,7]. 3D-Magnetometer can be utilized to determine the heading measurements relative to the Earth's magnetic north [2,8-10]. Radars greatly impact automotive applications, especially the frequency-modulated-continuous-wave (FMCW) radar [2,11,12]. The FMCW radar can determine both the distance and velocity of a target. The FMCW consumes less power than the CW radar, has a small size, and is much more affordable. For this paper, FMCW radar is used for the correction of the inertial system only during the GNSS outage periods.

Kalman filter (KF) can be used for INS and GPS data fusion for integrated positioning and navigation to take advantage of both sensors systems [13,14]. However, KF may not handle the stochastic and high order errors of MEMS grade INS sensors appropriately. Korenberg proposed a general-purpose modeling technique Fast-Orthogonal-Search (FOS) [15]. For time-series analysis, FOS takes the form of a sinusoidal series, and for system identification, FOS is modeled in the form of a non-linear difference equation [16,17]. This paper will focus on using GPS, 3D-RISS, 3D-Magnetometer, ACC-FMCW-Radar, and FOS to enhance navigation.

This paper compares few different techniques and their effect on the overall navigation solution. This investigation is beneficial for land vehicle navigation and other mobile systems. The application of proposed integrated navigational aids can provide accurate location information in challenging situations.

RISS MECHANIZATION

The low-cost 3D Reduced Inertial Sensor Systems (RISS) platform consists of one MEMS grade gyroscope (vertically aligned to the body frame of the vehicle), two accelerometers (pointing in the forward and transverse directions of the vehicle), and an odometer [18, 19]. In 3D-RISS, the z-axis gyroscope is used to measure the azimuth, two accelerometers to determine pitch and roll, and the vehicle's odometer to measure the velocity [20].

To calculate the azimuth, one must first calculate the rate of change of the azimuth. The azimuth can be calculated using the gyroscope and odometer readings, v_e , the latitude, φ, and the nominal radius of the Earth, R_N. The azimuth must also be compensated with the component of the Earth's rotation and the rotation of the local level frame on the Earth's curvature. The rate of change of the azimuth can be calculated using the above variables as:

$$\dot{A} = -\left(\omega_z + \omega^{ie} sin\varphi - \left(\frac{v_e tan\varphi}{R_N + h}\right)\right) \quad (1)$$

Where ω_z is the measurement made by the z-axis accelerometer, ω^e is the Earth's rotation rate, φ is the latitude of the vehicle, v_e is the Eastern velocity of the vehicle, R_N is the normal radius of the Earth, and h is the altitude of the vehicle. The azimuth is obtained by integrating the azimuth change rate [20].

From the odometer, the translational velocity, v is converted into the east, north and up velocities using the azimuth previously calculated [19, 21].

$$v = \begin{bmatrix} v_e \\ v_n \\ v_u \end{bmatrix} = \begin{bmatrix} v_{od}\, sin(A)\, cos(p) \\ v_{od}\, cos(A)\, cos(p) \\ v_{od}\, sin(p) \end{bmatrix} \quad (2)$$

The 3D-position components are obtained from the velocities as in Eq. (2), taking the earth geometry into consideration.

$$\begin{bmatrix} \dot{\varphi} \\ \dot{\lambda} \\ \dot{h} \end{bmatrix} = \begin{bmatrix} \frac{v_n}{R_M + h} \\ \frac{v_e}{(R_N + h)cos(\varphi)} \\ v_u \end{bmatrix} \quad (3)$$

Where R_M is the meridian radius of the Earth, R_N is the normal radius of the Earth, $\dot{\varphi}$ is the rate of change in latitude, $\dot{\lambda}$ is the rate of change in longitude, and $\dot{h}$ is altitude rates, respectively [20-24].

FAST-ORTHOGONAL-SEARCH (FOS) ALGORITHM

The FOS employ an arbitrary set of non-orthogonal candidate functions $P_m(n)$ and finds a functional expansion of an input $y(n)$ to minimize the mean-square error (MSE) between the input and the functional expansion. The functional expansion of the input $y(n)$ in terms of the arbitrary candidate functions $P_m(n)$ is given by Eq. (4) [15]:

$$y(n) = \sum_{m=0}^{M} a_m P_m(n) + \varepsilon(n) \qquad (4)$$

Where: a_m is the weights of the functional expansion and $\varepsilon(n)$ is the modelling error.

There is no unique solution for Eq. (4) due to non-orthogonal candidate functions. FOS may model the input with less model terms than an orthogonal functional expansion [16]. FOS begins by generating a functional expansion using orthogonal basis functions as in Eq. (5).

$$y(n) = \sum_{m=0}^{M} g_m w_m(n) + e(n) \qquad (5)$$

Where, $g_m(n)$ is the weights of the functional expansion and $e(n)$ is the modelling error. $w_m(n)$ is the orthogonal functions that are derived from the candidate functions $P_m(n)$ using the Gram-Schmidt (GS) orthogonalization algorithm. Orthogonal functions $w_m(n)$ are implicitly defined by the GS coefficients α_{mr} and do not need to be computed point-by-point.

The GS coefficients α_{mr} and the orthogonal weights g_m can be found recursively using Eq.(4) through (9) [15, 16, 17].

In the final stage, FOS calculates the weights of the original functional expansion a_m (Eq. 3), from the weights of the orthogonal series expansion, g_m and the weights. The value of a_m can be found recursively using Eq. (6).

$$a_m = \sum_{i=m}^{M} g_i v_i, \qquad v_m = 1 \qquad (6)$$

Where,

$$v_i = -\sum_{r=m}^{i-1} \alpha_{ri} v_r, \qquad i = m+1, m+2, \ldots\ldots, M. \qquad (7)$$

The mean squared error (MSE) of the orthogonal function expansion has been shown to be as in Eq.(8) [15, 16].

$$\overline{\varepsilon^2(n)} = \overline{y^2(n)} - \sum_{m=0}^{M} g_m^2 \overline{w_m^2(n)} \qquad (8)$$

It then follows that the MSE reduction given by the m^{th} candidate function is given by [15,16]:

$$Q_m = g_m^2 \overline{w_m^2(n)} = g_m^2 D(m,m) \qquad (9)$$

FOS can fit a system model with less terms by fitting terms that reduce the MSE in order of their significance.

LOOSELY COUPLED GPS/INS INTEGRATION

For loosely coupled GPS/RISS/Mag/Radar integration, GPS and RISS (augmented with Mag and Radar systems) operate separately and provide separate navigation solutions. The solutions for both GPS and RISS are fed to a KF to model the error of the RISS component. During GPS outages, the integration uses the error model developed during the availability of GPS to estimate the RISS error. The integrated solution can be calculated by removing the estimated error from the RISS solution [2,20]. Two versions of RISS systems are used, first based on an odometer and the other based on the adaptive cruise control frequency modulated continuous wave (ACC-FMCW) radar, as shown in Fig 1.

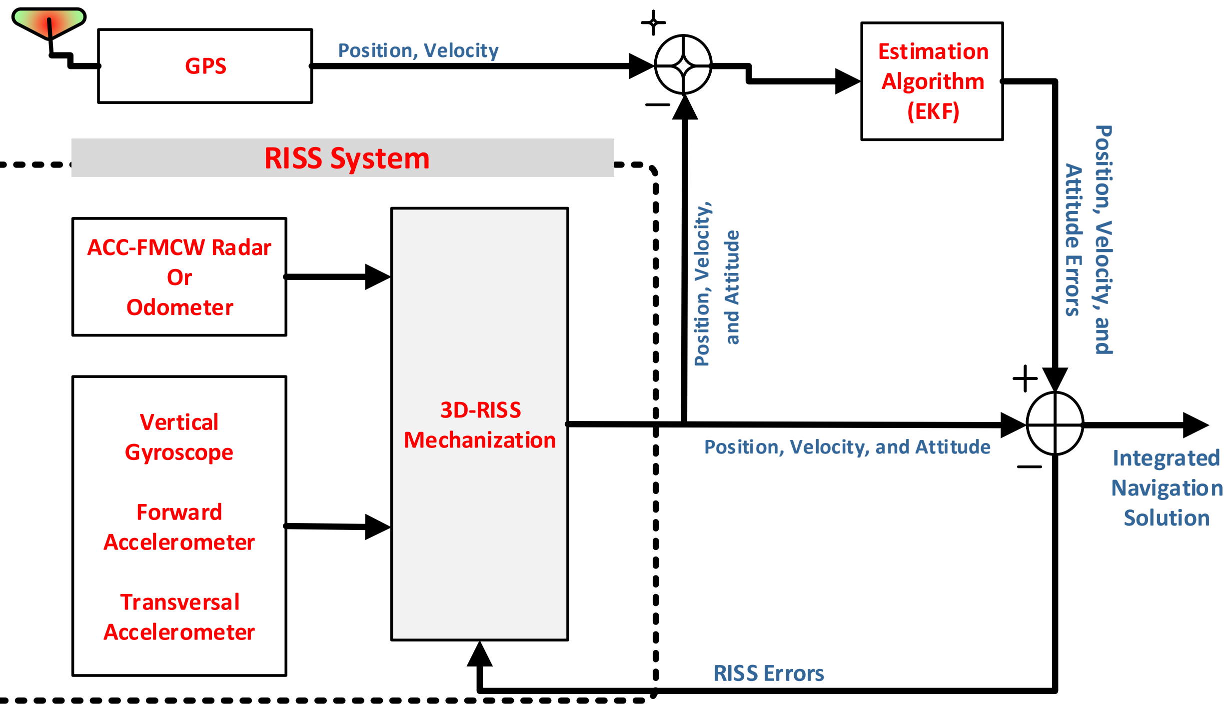

Fig. 1 Integrated Navigation System Block Diagram

The magnetometer can be used to further improved by augmenting magnetic-azimuth update to limit the position drift for prolonged GPS outages. Calibrated azimuth from the 3D-Magnetometer assists the ACC-FMCW Radar-based RISS system performance improvement. Fast orthogonal search (FOS) can further enhance the system by providing non-linear error modeling of the residual errors associated with the ACC-FMCW radar positioning solution to reduce the error growth over the prolonged GNSS outages. FOS is to generate a non-linear error model for the Mag/ ACC-FMCW radar-based RISS while the FOS/Magnetometer / Radar-based RISS /GPS solution is available (i.e., GPS signals are available). Afterward, the generated model is fed to the system during the GPS outages for performance improvement. FOS is utilized to mitigate the residual non-linear errors for FOS/Magnetometer / Radar-based RISS /GPS that could not be modeled and compensated for with the EKF-based architecture.

EXPERIMENTAL SETUP AND RESULTS

Experimental work was carried out through actual road trajectory in the downtown area of Kingston, ON, Canada, to verify the effectiveness of the proposed algorithms. One 300 seconds duration outage was simulated for the trajectory. Table 1 compares the performance of four different system configurations.

Equipment used include: [A Novatel dual-frequency GNSS receiver (SPAN-OEM4), Novatel tactical-grade IMU-CPT unit, A MEMS-grade Crossbow IMU 300CC-100, A 3-axis magnetometer (Model number: HMC5883L)]. The RMS-Error in position is calculated by taking the square of the error between the proposed system solution and the reference solution. The reference trajectory is based on the tightly coupled integration between the IMU-CPT and the SPAN-OEM4 GPS receiver.

Table 1 Performance comparison during Outages of 300 Seconds

System Configuration	RMS-Error in position
Odometer-based RISS/GPS	182.4 m
Radar-based RISS/GPS	94.5 m
Magnetometer/Radar-based RISS/GPS	67 m
FOS/Magnetometer/Radar-based RISS/GPS	18.8 m

CONCLUSION

This paper has reviewed four different system configurations, using GPS, ACC-FMCW radar, magnetometers, MEMS-based RISS, to enhance land vehicle navigation. The results show that the performance of a multi-sensor integration algorithm can be improved by using innovative system configurations and can be further improved by applying techniques such as **FOS** to obtain a more accurate positioning solution.

REFERENCES

[1] Anon., 2019. Federal Highway Traffic Safety Policies: Impacts and Opportunities (R44394). Available at: https://www.everycrsreport.com/reports/R44394.html [Accessed 25 March 2020].

[2] A. Abosekeen, U. Iqbal, A. Noureldin, and M. J. Korenberg, “A Novel Multi-Level Integrated Navigation System for Challenging GNSS Environments,” IEEE Trans. Intell. Transp. Syst., pp. 1–15, 2020, doi: 10.1109/TITS.2020.2980307.

[3] Anon., 2020. How Connected Vehicles Work. [Online] Available at: https://www.transportation.gov/research-and-technology/how-connected-vehicles-work [Accessed 24 March 2020].

[4] Lee, B.-H.et al., 2015. GPS/DR Error Estimation for Autonomous Vehicle Localization. Sensors, 15(8), p. 20.

[5] Bishop, R., 2005. Intelligent Vehicle Technology and Trends. Norwood, MA 02062: Artech House.

[6] Iqbal, U. et al., 2013. Pseudoranges Error Correction in Partial GPS Outages for Non-Linear Tightly-Coupled Integrated System. IEEE Transactions on Intelligent Transportation Systems, pp. 1510 – 1525 14 (3).

[7] A. D. King, "Inertial Navigation - Forty Years of Evolution," GEC Review 1998.

[8] R. B. Langley, “Getting Your Bearings. The Magnetic Compass and GPS,” Innovation Column, GPS World, Sept. 2003.

[9] A. Abosekeen, T. B. Karamat, A. Noureldin, and M. J. Korenberg, "Adaptive cruise control radar-based positioning in GNSS challenging environment," IET Radar, Sonar Navig., vol. 13, no. 10, pp. 1666–1677, Oct. 2019.

[10] A. Abosekeen, A. Noureldin, and M. J. Korenberg, “Improving the RISS/GNSS Land-Vehicles Integrated Navigation System Using Magnetic Azimuth Updates,” IEEE Trans. Intell. Transp. Syst., vol. 21, no. 3, pp. 1250–1263, Mar. 2020.

[11] V. Issakov, “Radar Systems,” in Microwave Circuits for 24 GHz Automotive Radar in Silicon-based Technologies, 2010, pp. 1–208.

[12] A. Abosekeen, U. Iqbal, A. Noureldin,, “IMPROVED NAVIGATION THROUGH GNSS OUTAGES: Fusing Automotive Radar and OBD-II Speed Measurements with Fuzzy Logic,” GPS World, vol. 32, no. 2, pp. 36–41, Feb-2021.

[13] U. Iqbal, T. B. Karamat, A. F. Okou, and A. Noureldin, "Experimental Results on an Integrated GPS and Multisensor System for Land Vehicle Positioning," International Journal of Navigation and Observation, Hindawi Publishing Corporation, 2009.

[14] P. Zarchan, Fundamental of Kalman Filtering: A Practical Approach, 2nd ed., American Institute of Aeronautics and Astronautics (AIAA), 2005.

[15] Korenberg, M.J., "Fast Orthogonal Identification of Non-linear Difference Equation and Functional Expansion of Models", Proceedings

of the 30th Midwest Symposium of Circuits and Systems, vol. 1, August 1987, pp. 270-276.

[16] Adeney, K.M and Korenberg, M.J., "Fast Orthogonal Search for Array Processing and Spectrum Estimation", IEEE Proceedings – Vision, Image and Signal Processing, vol. 141, no. 1, February 1994, pp. 13-18.

[17] Korenberg, M.J., and Paarmann, LD, "Applications of Fast Orthogonal Search: Time-Series Analysis and Resolution of Signal in Noise," Annals of Biomedical Engineering, vol. 17, 1989, pp. 219-231.

[18] U. Iqbal, F. Okou, and A. Noureldin, "An Integrated Reduced Inertial Sensor System-RISS/GPS for Land Vehicles," in Proceeding of IEEE/ION Position, Location and Navigation Symposium, Monterey, CA, 2008, pp. 1014.

[19] U. Iqbal and A. Noureldin, Integrated Reduced Inertial Sensor System/GPS for Vehicle Navigation, VDM Verlag, 2009.

[20] J. Georgy, A. Noureldin, M. Korenberg, and M. Bayoumi., "Low Cost Three Dimensional Navigation Solution for RISS/GPS Integration Using Mixture Particle Filter," IEEE Transactions on Vehicular Technology, vol. 59(2), pp. 599-615, 2010.

[21] Aboelmagd N, Karmat TB, Georgy J (2013) Fundamentals of inertial navigation, satellite-based positioning and their integration. Springer, Berlin.

[22] A. Abosekeen, A. Noureldin, and M. J. Korenberg, “Utilizing the ACC-FMCW radar for land vehicles navigation,” in 2018 IEEE/ION Position, Location and Navigation Symposium (PLANS), 2018, pp. 124–132.

[23] A. Abosekeen, U. Iqbal, and A. Noureldin, “Enhanced Land Vehicles Navigation by Fusing Automotive Radar and Speedometer Data,” in 33rd International Technical Meeting of the Satellite Division of the Institute of Navigation (ION GNSS+ 2020), 2020, pp. 2206–2219.

[24] M. A. Rashed, A. Abosekeen, H. Ragab, A. Noureldin, and M. J. Korenberg, “Leveraging FMCW-radar for autonomous positioning systems: Methodology and application in downtown Toronto,” in Proceedings of the 32nd International Technical Meeting of the Satellite Division of the Institute of Navigation, ION GNSS+ 2019, 2019, pp. 2659–2669.

Analysis of Energy Transfer Mechanism in Bypass Transition using Direct Numerical Simulation

Satish Muthu[1] and Shanti Bhushan[2]
[1]Department of Bioinformatics, Mississippi Valley State University, Itta Bena, MS, 38941
[2]Department of Mechanical Engineering, Mississippi State University, Starkville, MS, 39762

Corresponding Author: Shanti Bhushan
E-mail:bhushan@me.msstate.edu
https://doi.org/10.31753/IJRD28760144

ABSTRACT

The mechanism of bypass transition from laminar to turbulent flow states is still not very well understood. The research focuses on analysis of the inter-component turbulent energy transfer in the pre-transition, transition and turbulent regimes using temporally developing direct numerical simulation (DNS) for freestream turbulence induced bypass transition flow over a flat-plate boundary layer (FPBL) to elucidate such mechanism. Results demonstrate that the pressure-strain is the key term that distributes energy from the longitudinal Klebanoff modes, generated in the pre-transition regime, to the wall-normal and spanwise components resulting in three-dimensional turbulence. The transition to turbulence is inhibited as the pressure-strain is suppressed (of shear sheltering effect), which occurs because the rapid part of the term balances the slow (return) part of the term. Consequently, the bypass transition initiates as the return pressure-strain starts to dominate over the rapid pressure-strain. This fundamental understanding of the bypass transition mechanism provides a basis for deriving transition onset marker.

NOMENCLATURE

C_f	: Skin friction coefficient
k	: Turbulent kinetic energy, $k = \frac{1}{2}(u'^2 + v'^2 + w'^2)$
x, y, z	: Streamwise, wall-normal and spanwise coordinate directions, respectively.
U	: Mean streamwise velocity
$\tau_{ij} = \overline{u_i' u_j'}$	: Reynolds stress components
u', v', w'	: Turbulent velocity fluctuations along *x*, *y* and *z* directions, respectively.
p'	: Turbulent pressure fluctuations
p_r', p_s', p_{st}'	: Rapid, return (slow) and wall (Stokes) components of the pressure fluctuations, respectively.
R_{ij}	: Pressure-strain correlation
R_{ij}^r, R_{ij}^s, R_{ij}^{st}	: Rapid, return (slow) and wall (Stokes) components of the pressure-strain correlation respectively
Tu	: Freestream turbulence intensity
u_τ	: Friction velocity, $u_\tau = \sqrt{\tau_w/\rho}$
δ	: Boundary layer thickness
ν	: Kinematic viscosity
ρ	: Density
Re_X	: Reynolds number based on distance along the plate.
$\overline{\cdots}$	: Ensemble averaging, both over streamwise-spanwise (*x*-*z*) plane and time.
$[\ \ ]^+$	: Non-dimensional variables in wall units, i.e., nondimensionalized by $u_\tau$and ν.

INTRODUCTION

Accurate prediction of boundary layer flow is critical for analyzing stress and thermal loading for a wide range of engineering applications, including aerospace, automotive, biomedical, power generation and chemical processing. One key feature of the boundary layer is whether it is laminar or turbulent. In general, turbulent flows exert higher frictional forces and result in higher heat transfer. Hence, an improved understanding of the transition flow pattern is important for the design of a vehicle or the thermal protection system [1].

The boundary layer flow regimes that cannot sustain self-energizing turbulent motions are referred to as "laminar." When the boundary layer experiences large-scale three-dimensional fluctuations with scales larger than the boundary layer thickness and the wall stress and heat transfer characteristics start to deviate from the laminar boundary layer, the flow is referred to as "buffeted laminar." As the Reynolds number increases, small disturbances (turbulence intensity Tu < 1%) can cause the boundary layer to undergo "natural transition" from laminar to turbulent states. The natural transition is characterized by the growth of low amplitude Tollmien-Schlichting (T-S) waves. The modal stability theory provides the critical Reynolds number when the disturbances start to grow. It is assumed that disturbance amplitudes grow exponentially, and the transition onset occurs when their amplification reaches a threshold value. When the laminar boundary layer is exposed to large external disturbances, such as high freestream turbulence, large wall roughness elements, flow separation, pressure gradient effects etc. [2-4], the transition from laminar to turbulent states bypass the above linear stability theory and is referred to as "bypass transition."

A review of the literature shows that understanding of bypass transition mechanism is not mature [5]. The known physical mechanisms of turbulent spot formation and turbulence growth have been primarily developed using high-fidelity numerical predictions of flat-plate boundary layer transition because of freestream turbulence under zero-pressure gradient conditions [6-14]. For such flow conditions it is well accepted that the bypass transition initiates with the generation of longitudinal streaks (Klebanoff modes) in the pre-transition region [15] and that energy of the streaks ($\overline{u'^2}$) grows linearly with Re_X [16], where Re_X is Reynolds number based on the distance along the plate. Transition occurs because of the secondary sinuous and/or varicose-like instabilities of the longitudinal streaks, which is accompanied by the ejection and spanwise sway of the streaks [17] and formation of turbulent spots. Thus, transition onset is accompanied by transfer of energy form the streamwise fluctuating component to the wall-normal and spanwise components. However, studies have not reached a consensus regarding the mechanisms responsible for turbulent spot formation, turbulence energy production, and the energy transfer pathway from freestream disturbances to pre-transitional fluctuations to turbulent fluctuations. The primary objective of this study is to propose an energy transfer mechanism for boundary layer bypass transition based on the role of the pressure-strain correlation using direct numerical simulations (DNS) of zero-pressure gradient flat-plate boundary layer.

VALIDATION FOR DNS PREDICTIONS

A review of literature [6-14], shows that DNS of transitioning flat-plate boundary layer flows are typically performed using spatially developing flows. However, such approach limits simulations to high freestream turbulence intensities (Tu) ≥ 3%, as transition occurs at low $Re_X < 10^5$ and requires small flow domain and grid sizes. An alternative to the spatially developing DNS (S-DNS) is the temporally developing DNS (T-DNS) [18]. In this latter approach, the simulation is started with an initial laminar boundary layer condition superimposed with freestream disturbances, and a periodic boundary condition is applied along the streamwise and spanwise directions. This allows the simulation domain to move along with the flow, and it is expected that the solution at any instant is a realization of an infinitesimal section of the flat-plate boundary layer, as demonstrated in Fig. 1. Such simulations require a smaller streamwise domain compared to the spatially developing counterparts and is expected to be one to two orders of magnitude less computationally expensive for high Re_X flows.

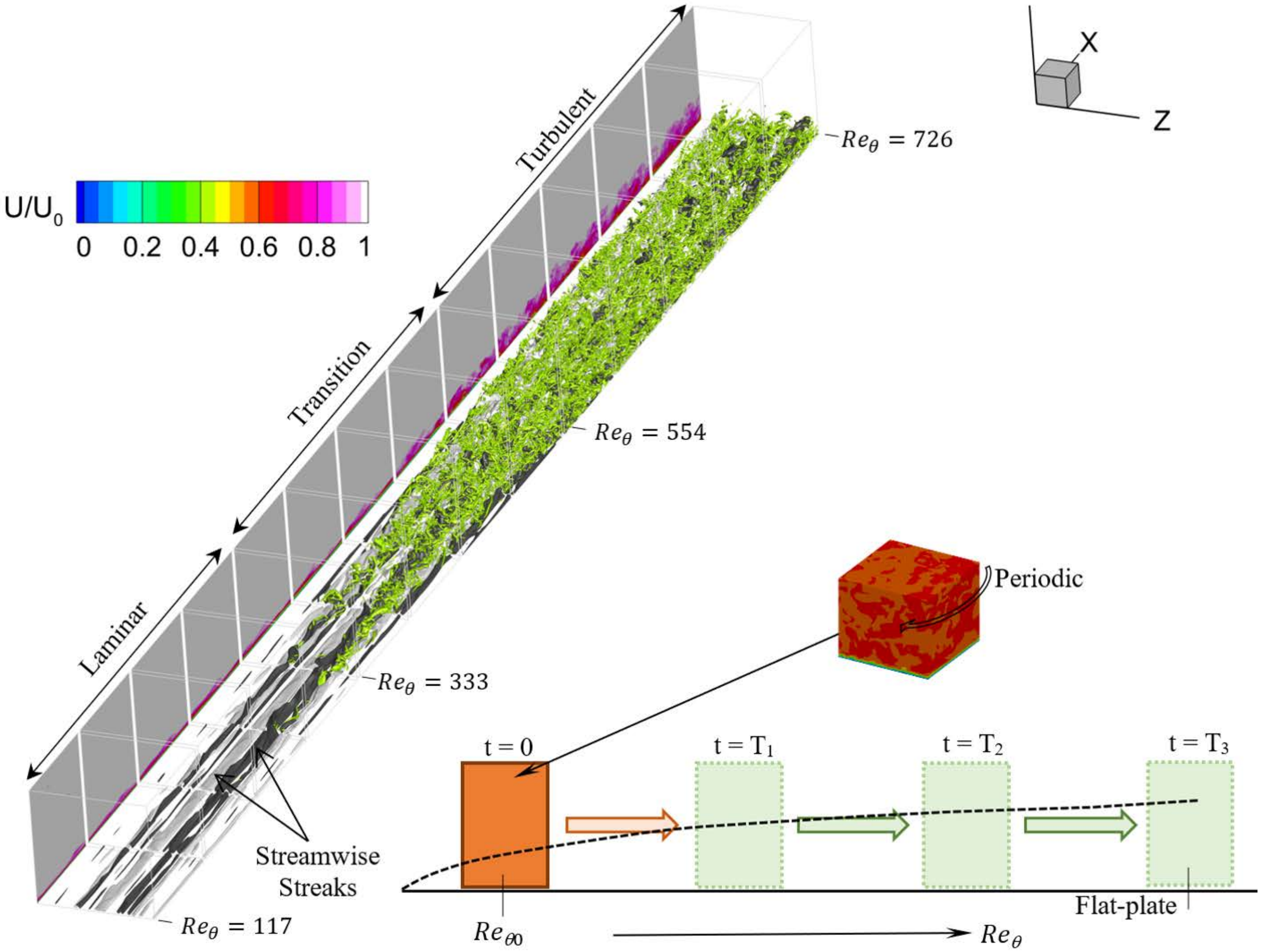

Figure 1. Temporal variation of the flow for the $Tu = 3.5\%$ case obtained using DNS. The plot shows contours of instantaneous streamwise velocity, u/U_0 at the spanwise center plane $z = 0$ obtained by placing results every 2000 time-steps (or $1U_0/L$) shown side-by-side to show the growth of the boundary layer. The black and white isosurfaces show the growth of high ($u' = 0.1U_0$) and low ($u' = -0.1U_0$) speed longitudinal streaks, respectively. The green isosurfaces show the turbulent coherent structures, which are visualized using isosurfaces of second largest eigen value of the rate-of-strain tensor $\lambda_2 = -20$. The inset plot shows a schematic diagram demonstrating the evolution of the flow during a temporally developing simulation.

The simulations are performed using a pseudo-spectral solver which solves the incompressible Navier-Stokes equations using Fast Fourier Transforms (FFT) along the periodic streamwise (x) and spanwise (z) directions, and Chebyshev's polynomials along the non-homogeneous wall normal (y) direction [19]. The simulations were performed using a cubic domain with dimensions varying from $20\delta_0$ to $50\delta_0$, where δ_0 is the initial laminar boundary layer thickness. The initial flow conditions included $Tu = 3.5\%$ and laminar boundary layer thickness-based Reynolds number $Re_{\delta_0} = 798.2$ and freestream turbulence length scale $\ell_0/\delta_0 = 1.85$. Two different grid resolutions were used consisting of $192{\times}257{\times}192$ and $256{\times}257{\times}256$ (fine) points along the streamwise, wall-normal and spanwise directions, respectively. The grid was uniform in the streamwise and spanwise direction, but clustered near the wall ($y = 0$). The fine grid involved grid resolution of $\Delta x^+ \sim 6$, $\Delta z^+ \sim 0.30$, $\Delta y^+_{min} \sim 0.25$ and $\Delta y^+_{max} \sim 11.5$ for the $40\delta_0$ domain, which satisfies DNS grid resolution guidelines [18]. The initial turbulent fluctuations were obtained using a precursor T-DNS of decaying isotropic turbulence over a flat-plate.

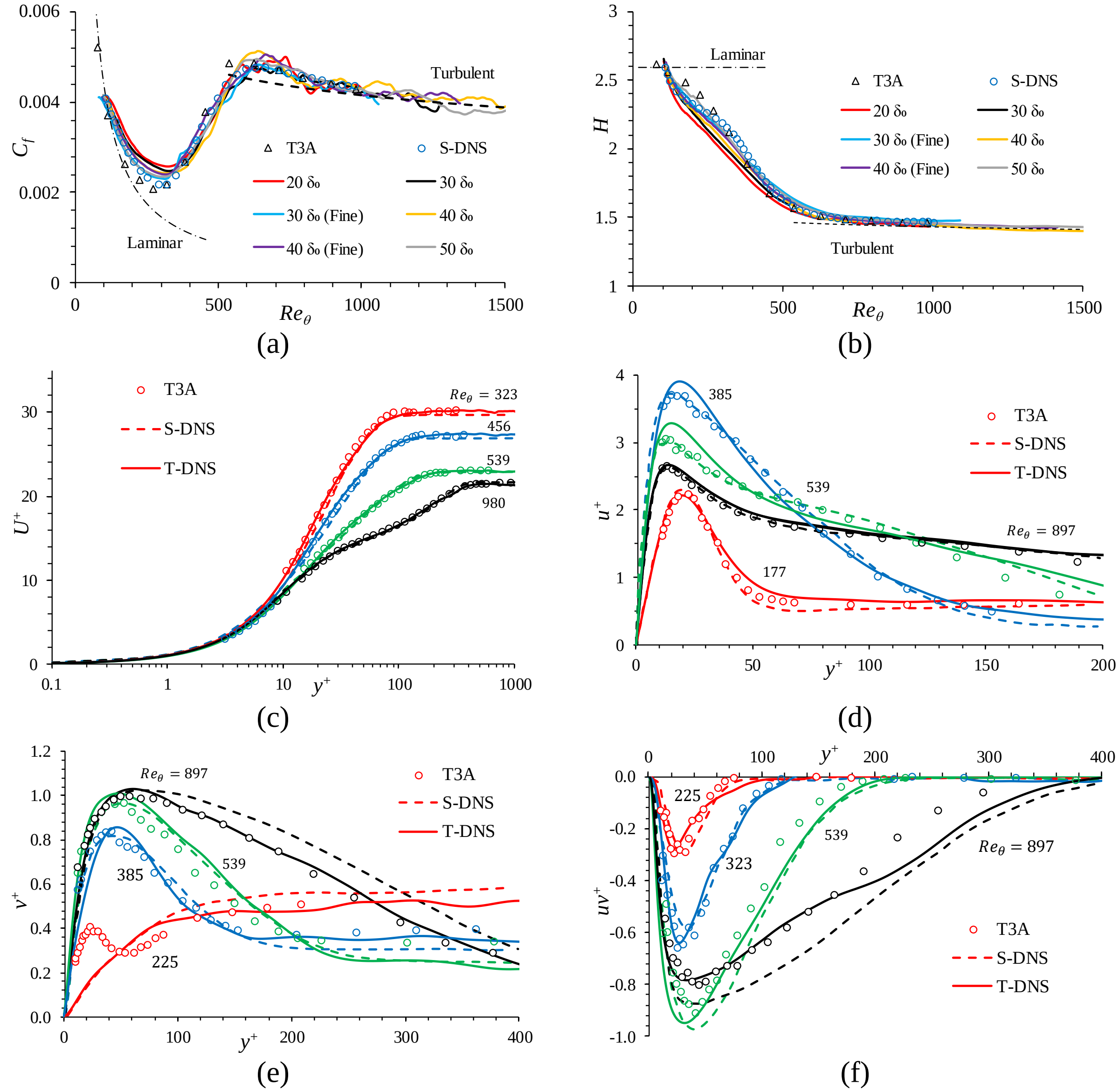

Figure 2. T-DNS predictions of: (a) C_f, (b) H in boundary layer (Re_θ) coordinates, and (c) mean velocity profiles; (d) $u^+ = \sqrt{\overline{u'^2}}/u_\tau$; (e) $v^+ = \sqrt{\overline{v'^2}}/u_\tau$; and (f) shear stress $\overline{u'v'}/u_\tau^2$ in pre-transition, transition, and turbulent regimes (Re_θ locations for the respective profiles are indicated on the figure) for $Tu = 3.5\%$. The results are compared with S-DNS [20] and with experiments [21].

As depicted in Fig. 1, the temporal simulations accurately predicted the growth of near-wall Klebanoff modes in the pre-transition regime, their subsequent breakdown in the transition regime, and the generation of counter-rotating quasi-streamwise and hairpin-like structures in the turbulent regime. The effect of domain size and grid resolution on the transition predictions are analyzed for the predictions of the boundary layer parameters skin friction coefficient C_f and shape factor H in boundary layer (or Re_θ) coordinates as shown in Fig. 2(a) and 2(b). The C_f profile shows laminar regime up to $Re_\theta \leq 330$, transition regime for $330 < Re_\theta \leq 670$, and turbulent regime for $Re_\theta > 670$. In the transition regime, C_f is slightly over-predicted compared to S-DNS [20] and experiment [21] on smaller domains and the predictions improve with the increase in the domain size. Analysis of the streamwise velocity fluctuation shows that the over-prediction of C_f is due to the over-prediction of the turbulent fluctuations u' associated with the streaks. Grid refinement shows significant improvement in results for $30\delta_0$ domain and provides the best agreement with the S-DNS. In the turbulent regime, all the simulations show unsteady C_f. The predictions on $50\delta_0$ shows the least unsteadiness, as the turbulence is underpredicted because of coarse grid resolution. Detailed analysis revealed that a streamwise domain size of $40\delta_0$ is large enough to ensure that the turbulent structures are de-correlated, and small enough such that the spatial growth of the boundary layer within the domain is negligible to justify the streamwise periodic boundary condition. Thus, final validation and analysis was performed using results obtained on $40\delta_0$ domain discretized using the fine grid.

The mean velocity, $U^+ = \bar{u}/u_\tau$, profile in Fig. 2(c) shows a large sub-layer, growth of log-layer, and well-defined log-layer in the laminar, transition and turbulent regimes, respectively. T-DNS predictions compare very well with experiments and S-DNS for all Re_θ locations. The streamwise velocity fluctuations in Fig. 2(d) show significant energy in the near-wall region, which are contained in the Klebanoff modes. The energy is transported away from the wall during transition, which results in the growth of the log-layer. The fluctuations show a sharp 70% increase from $Re_\theta = 177$ to 385, i.e., in the pre-transition to early transition regime, and beyond that the peak decreases by 40% and the profile becomes flatter. The T-DNS predictions compare well with experiments and S-DNS in the pre-transition and turbulent regions but show a slight overprediction (~6%) of the peak values for $Re_\theta =$ 385 and 590. The Reynolds stress profiles at selected laminar, transition, and turbulent locations in Figs. 2(e) and 2(f) also agree reasonably well with S-DNS and experimental data.

STRESS BUDGETS AND ROLE OF PRESSURE-STRAIN CORRELATION

T-DNS predictions of the Reynolds stress and turbulent kinetic energy (TKE) budgets for the flat-plate boundary layer in the fully developed turbulent regime are shown in Figure 3. The stress budget terms are computed as:

$$\frac{\partial \tau_{ik}}{\partial t} + \underbrace{\overline{u}_j \frac{\partial \tau_{ik}}{\partial x_j}}_{C} = \underbrace{-\left(\tau_{kj}\frac{\partial \overline{u_i}}{\partial x_j} + \tau_{ij}\frac{\partial \overline{u_k}}{\partial x_j}\right)}_{P} + \underbrace{\overline{\frac{p'}{\rho}\left(\frac{\partial u_k'}{\partial x_i} + \frac{\partial u_i'}{\partial x_k}\right)}}_{R} - \underbrace{\frac{\partial\left(\overline{u_i'u_j'u_k'}\right)}{\partial x_j}}_{PT} - \underbrace{\frac{1}{\rho}\frac{\partial\left(\overline{p'u_k'}\delta_{ij} + \overline{p'u_i'}\delta_{kj}\right)}{\partial x_j}}_{T} + \underbrace{\nu\frac{\partial^2 \tau_{ik}}{\partial x_j \partial x_j}}_{D} - \underbrace{2\nu\overline{\frac{\partial u_i'}{\partial x_j}\frac{\partial u_k'}{\partial x_j}}}_{\varepsilon} \tag{1}$$

where, $j = 1,2,3$ and C, P, R, ε, D, T, and PT represent the turbulent convection, turbulent production, pressure-strain, viscous dissipation, viscous diffusion, turbulence diffusion, and the pressure transport terms, respectively. The indices i and j denote the three flow directions (x, y, z) and range from 1 to 3. Repeated indices denote summation. Note that the averaged values denoted by the overbar symbol are obtained using spatial averaging in the $x - z$ plane. Thus, for such flows involving slow streamwise growth and U is the only mean streamwise velocity component, the only terms that survive in Eq. (1) are shown in Table 1.

The stress budgets in the fully developed turbulence region are similar to the S-DNS data for channel flow ($Re_\tau = 590$) [23] and fully-developed turbulent flat-plate boundary layer ($Re_\theta = 1100$) [22]. The results show that v' generation near the wall ($y^+ < 7$), or ejection events, are due to pressure-diffusion, and balanced by pressure-strain which tends to reorient wall normal fluctuations to the streamwise and spanwise directions. The turbulent energy is redistributed from u' to w' and v' via pressure-strain in the lower log-layer. Energy decay is mostly from u' followed by w' and least from v'. The budgets in the transition regime (not shown) show turbulence production and growth mechanisms similar to the turbulent flow. The stress budget in the laminar region (not shown) shows growth of u' fluctuations, which are the Klebanoff modes. The production of the fluctuations initiates from the interaction of the mean flow gradients with freestream v' to generate turbulent shear $u'v'$, and the latter further interacts with $u'v'$ to produce u'. The energy-transfer and distribution patterns emphasize that the growth of the pressure-strain term is critical for transition onset. The TKE budget in the fully developed turbulent region as shown in Fig. 3(e) shows that in the sub-layer ($y^+ \leq 5$) the viscous diffusion is proportional to the dissipation. In the buffer layer ($5 < y^+ \leq 30$) the production dominates and is roughly balanced by the sum of viscous diffusion and turbulent diffusions and dissipation. In the log layer ($y^+ > 30$), production is proportional to the dissipation. Also, viscous diffusion is dominant for $y^+ < 10$ and pressure transport is negligible throughout.

The role of pressure-strain in transition is an open area of research. Mayle and Schulz [24] reported that the pressure diffusion term is the main driver for the growth of the near-wall streaks, and the pressure-strain terms are the primary mechanism for energy redistribution. Large eddy simulation results for flat-plate boundary layers [25,26], and developing channel flow DNS [27,28] studies (which exhibited transition-like behavior) also indicated that the pressure-strain terms transfer energy from the streamwise Reynolds stress component to the other normal stress components and participate in the generation of wall-normal (v') fluctuations during ejection events. They also noted that pressure-strain terms are negligible in the pre-transition regime compared to the fully developed turbulent region. This is further supported by DNS results [10,11,17] in which it was reported that the stark differences between the elongated near-wall streaks in the pre-transition regime and the nearly isotropic coherent structures in the freestream turbulence can be explained due to the shear-sheltering mechanism, i.e., inhibition of the pressure-strain terms which results in suppression of three-dimension turbulence growth. The stress budget analysis confirms the role of pressure-strain on transition initiation and turbulence generation. The stress budget terms for the streamwise component integrated over the entire boundary layer in Figs. 4 and 5 confirms that the pressure-strain term is negligible in the pretransition regime compared to the fully developed turbulent region and activates right around the transition onset location and is the source of v' generation.

Table 1: Summary of the TKE and stress budget terms.

Budget variable	**Budget Term**						
	C	**P**	**ε**	**D**	**T**	**PT**	**R**
TKE		$-\overline{u'v'}\frac{\partial U}{\partial y}$	$-\frac{1}{Re}\overline{\frac{\partial u_i'}{\partial x_k}\frac{\partial u_i'}{\partial x_k}}$	$\frac{1}{Re}\frac{\partial^2 k}{\partial y^2}$	$-\frac{\partial \overline{k_{inst}v'}}{\partial y}$	$-\frac{1}{2}\frac{\partial \overline{p'v'}}{\partial y}$	0
$\overline{u'u'}$		$-2\overline{u'v'}\frac{\partial U}{\partial y}$	$-2\frac{1}{Re}\overline{\frac{\partial u'}{\partial x_k}\frac{\partial u'}{\partial x_k}}$	$\frac{1}{Re}\frac{\partial^2 \overline{u'u'}}{\partial y^2}$	$-\frac{\partial \overline{u'u'v'}}{\partial y}$	0	$2\overline{p'\frac{\partial u'}{\partial x}}$
$\overline{v'v'}$	0	0	$-2\frac{1}{Re}\overline{\frac{\partial v'}{\partial x_k}\frac{\partial v'}{\partial x_k}}$	$\frac{1}{Re}\frac{\partial^2 \overline{v'v'}}{\partial y^2}$	$-\frac{\partial \overline{v'v'v'}}{\partial y}$	$-\frac{\partial \overline{p'v'}}{\partial y}$	$2\overline{p'\frac{\partial v'}{\partial y}}$
$\overline{w'w'}$		0	$-2\frac{1}{Re}\overline{\frac{\partial w'}{\partial x_k}\frac{\partial w'}{\partial x_k}}$	$\frac{1}{Re}\frac{\partial^2 \overline{w'w'}}{\partial y^2}$	$-\frac{\partial \overline{w'w'v'}}{\partial y}$	0	$\overline{p'\frac{\partial w'}{\partial z}}$
$\overline{u'v'}$		$-\overline{v'v'}\frac{\partial U}{\partial y}$	$-2\frac{1}{Re}\overline{\frac{\partial u'}{\partial x_k}\frac{\partial v'}{\partial x_k}}$	$\frac{1}{Re}\frac{\partial^2 \overline{u'v'}}{\partial y^2}$	$-\frac{\partial \overline{u'v'v'}}{\partial y}$	$-\frac{\partial \overline{p'u'}}{\partial y}$	$\overline{p'\left[\frac{\partial u'}{\partial y}+\frac{\partial v'}{\partial x}\right]}$

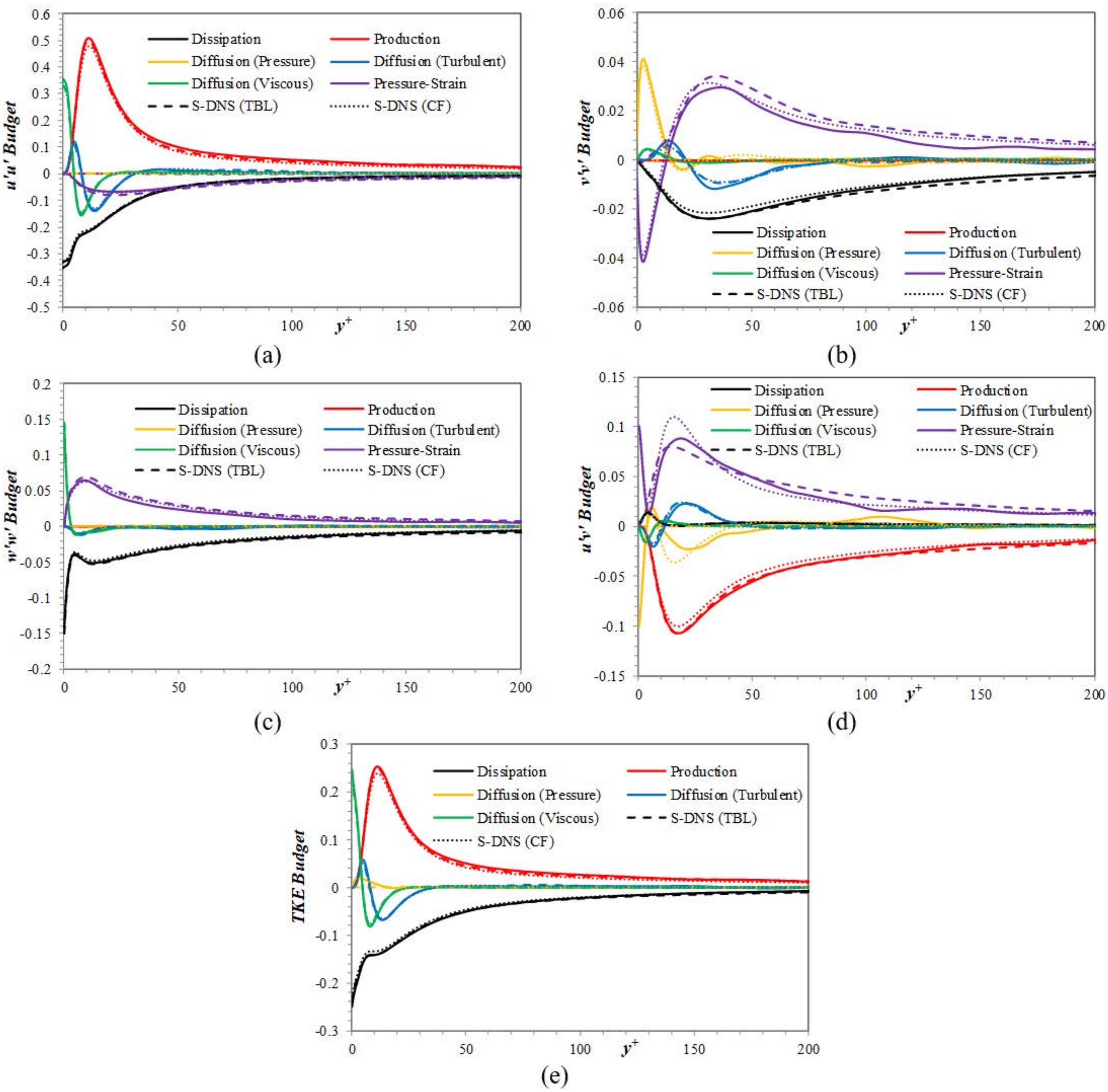

Figure 3. Budgets for: (a) $\overline{u'u'}$, (b) $\overline{v'v'}$, (c) $\overline{w'w'}$, (d) $\overline{u'v'}$ and (e) TKE in the fully developed flat-plate turbulent boundary layer ($Re_\theta = 1100$) obtained using T-DNS. Spatial DNS data of the fully developed turbulent boundary layer {S-DNS (TBL)}[22] at $Re_\theta = 1100$ and channel flow {S-DNS (CF)} [23] at $Re_\tau = 590$ are also shown for comparison.

ROLE OF RAPID AND SLOW PRESSURE-STRAIN TERMS IN TRANSITION

The governing equation for the fluctuating pressure is the Poisson equation derived from the Navier –Stokes equation for incompressible flow as:

$$-\frac{1}{\rho}\nabla^2 p' = \underbrace{2\frac{\partial \bar{u}_i}{\partial x_j}\frac{\partial u_j'}{\partial x_i}}_{Rapid\ source\ term} + \underbrace{\frac{\partial^2\left(u_i'u_j'\right)}{\partial x_i \partial x_j} - \frac{\partial^2\left(\overline{u_i'u_j'}\right)}{\partial x_i \partial x_j}}_{Slow\ source\ term} \tag{2}$$

The above equation is linear in pressure and can therefore be broken up into, the rapid (p_r'), slow (return) (p_s') and wall (Stokes) (p_{st}') components. The rapid source term represents the interaction between the mean flow and the fluctuating turbulent velocity gradients and is the origin of the rapid fluctuating pressure. The slow source term is because of the gradients of the turbulent velocity fluctuations. The individual pressure fluctuation components can be obtained as:

$$\nabla^2 p_r' = -2\rho \frac{\partial U}{\partial y}\frac{\partial v'}{\partial x}$$
$$\nabla^2 p_s' = -\rho \frac{\partial}{\partial x_l \partial x_k}\left(u_k'u_l' - \overline{u_k'u_l'}\right) \tag{3}$$
$$\nabla^2 p_{st}' = 0$$

with wall boundary conditions:

$$\left.\frac{\partial p_r'}{\partial y}\right|_w = 0;\ \left.\frac{\partial p_s'}{\partial y}\right|_w = 0;\ \text{and}\ \left.\frac{\partial p_{st}'}{\partial y}\right|_w = \mu\frac{\partial^2 v'^2}{\partial y^2} \tag{4}$$

The slow and rapid pressure-strains are computed using corresponding pressure fluctuations as:

$$R_{ij}^s = \overline{\frac{p_s'}{\rho}\left(\frac{\partial u_i'}{\partial x_j} + \frac{\partial u_j'}{\partial x_i}\right)}$$
$$R_{ij}^r = \overline{\frac{p_r'}{\rho}\left(\frac{\partial u_i'}{\partial x_j} + \frac{\partial u_j'}{\partial x_i}\right)} \tag{5}$$

Figure 6 shows the profiles of rapid and slow pressure-strain terms for the streamwise and wall-normal velocity fluctuations in the pre-transition and turbulent regimes. Note that the plots are shown for $Re_\theta = 200$ for the pre-transition regime, rather than $Re_\theta = 240$ as shown earlier, because this showed a much smoother profile compared to those at $Re_\theta = 240$. In the pre-transition region (Fig. 6a), R_{11}^s is mostly negative, whereas R_{11}^r is negligible. The wall-normal component shows an interesting behavior, where the slow and rapid component are opposite in nature and cancel each other almost exactly. The slow term is positive, whereas the rapid term is negative. In the fully developed turbulent regime (Fig. 6b), both R_{11}^r and R_{11}^s are negative, but the slow term is significantly larger than the rapid term. For the wall-normal component, R_{22}^s is mostly positive except for $y^+ < 10$, and R_{22}^r is mostly negative for $y^+ > 10$.

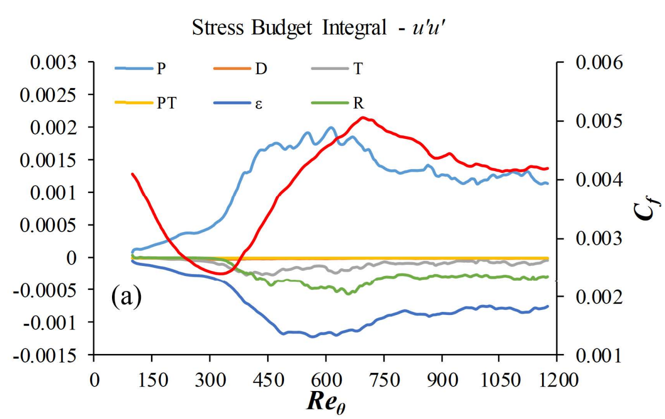

Figure 4. Integral of the Reynolds stress budget terms for: $\overline{u'u'}$ for flat-plate boundary layer with Tu =3.5% (primary axis). Variation of C_f is also shown (secondary axis).

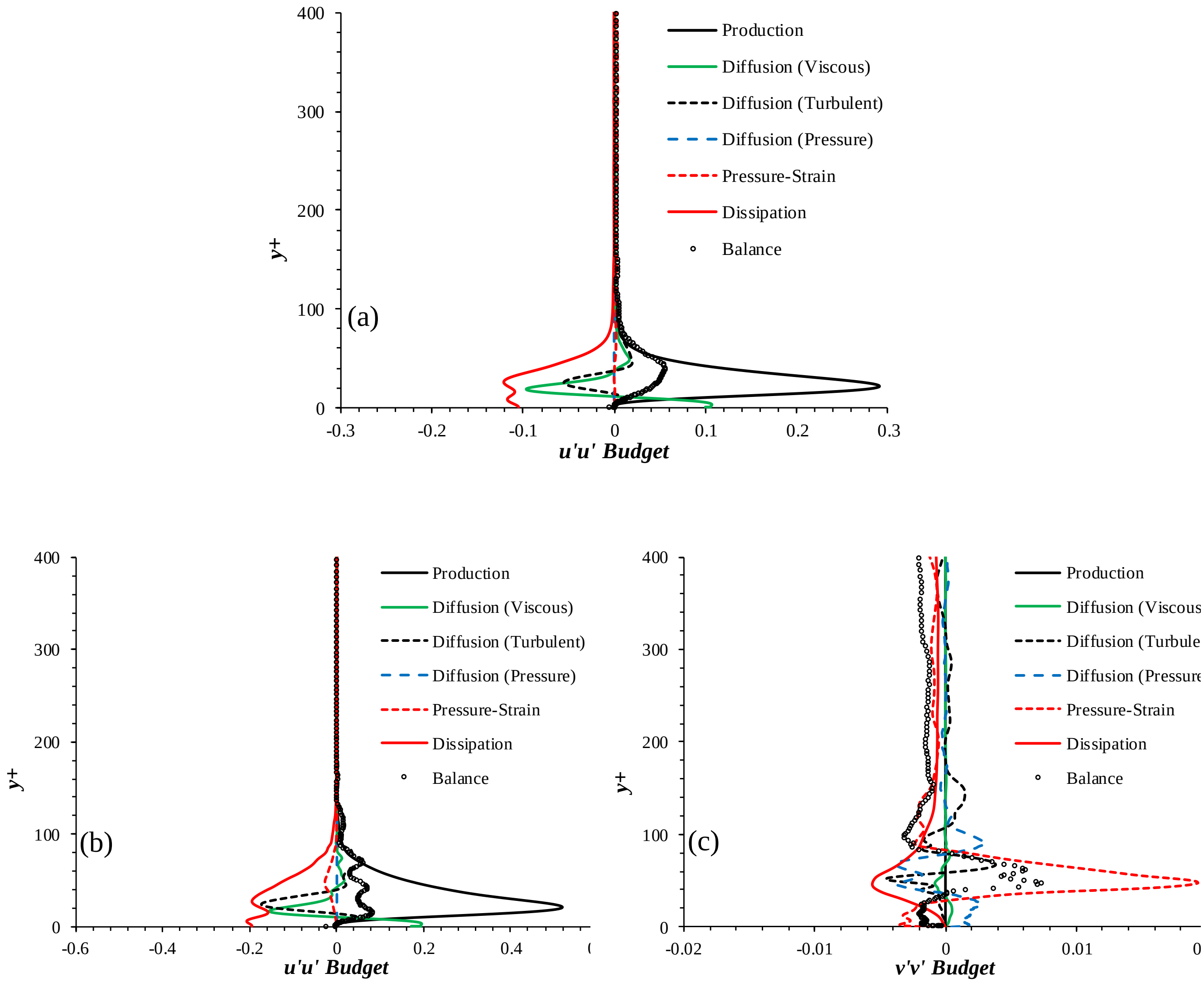

Figure 5. Stress budgets for a) $\overline{u'u'}$ in the pre-transitional regime $Re_\theta \approx 240$. Stress budgets for b) $\overline{u'u'}$ and c) $\overline{v'v'}$ at the onset of transition $Re_\theta \approx 330$ for flat-plate boundary layer T-DNS with $Tu = 3.5\%$.

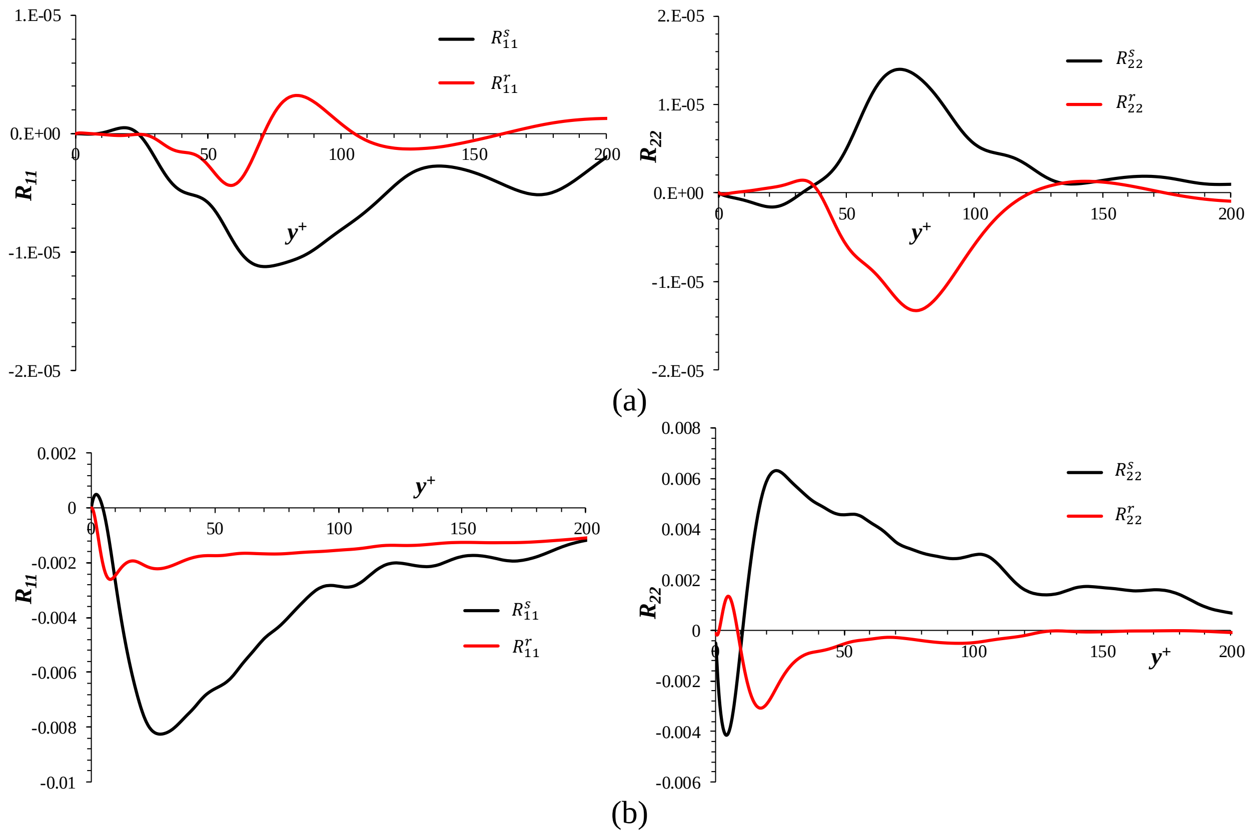

Figure 6. Profiles of the rapid and return part of the pressure-strain terms for $\overline{u'u'}$ and $\overline{v'v'}$ obtained for the $Tu = 3.5\%$ case in the: (a) pre-transitional regime $Re_\theta = 200$; and (b) fully-developed turbulent regime $Re_\theta = 1100$.

DISCUSSION AND CONCLUSIONS

TKE and shear stress budget in pre-transition, transition and turbulent flow regions were analyzed using DNS to understand the turbulence generation, transfer and dissipation pattern during bypass transition. The analysis emphasizes following key observations.

1. Bypass transition is characterized by the growth of longitudinal streaks (Klebanoff modes). These streaks are genereted as the freestream turbulence enters the laminar boundary layer and triggers wall-normal fluctuations v' via pressure diffusion. Following that v' interacts with mean shear to generate turbulent shear, $u'v'$, which in return interacts with the mean shear leads to the production of $u'u'$. This is consistent with mechanism reported by [29,30].
2. The pressure-strain term redistributes energy from the streamwise component to the wall-normal and spanwise components for $y^+ > 10$ resulting in 3D nature of turbulence. The pressure-strain terms are negligible in the pre-transition regime consistent with shear-sheltering phenomenon [20].
3. Splitting the pressure-strain into rapid and return components shows than both the components are present throughout the boundary layer, but they interreact differently. In the pre-transition region, they are nearly equal to each other and opposite in sign which leads to the suppression of the energy redistribution. As the boundary layer transitions to turbulence, the slow pressure-strain dominates over the rapid term. Thus, transition initiation can be thought of as to occur at a location where the return component starts to dominate over the rapid component.
4. In the sublayer region ($y^+ < 10$), the rapid and slow terms show an opposite trend, i.e., rapid component is the source of the v' generation, whereas slow component is a sink term. The slow term dominates over the rapid term, and is identified to be the cause of wall-blocking effect.

This is consistent with the rapid distortion theory, which identifies lack of the rapid pressure-strain term as the primary cause of wall-blocking.

The energy transfer pathway expected in the pre-transition and transition region is depicted in Fig. 7, and the primary difference between the two regimes is the relative effect of the slow (return) and rapid pressure-strain terms. This fundamental understanding of the bypass transition mechanism provides a basis for deriving transition onset marker by Muthu et al. [31].

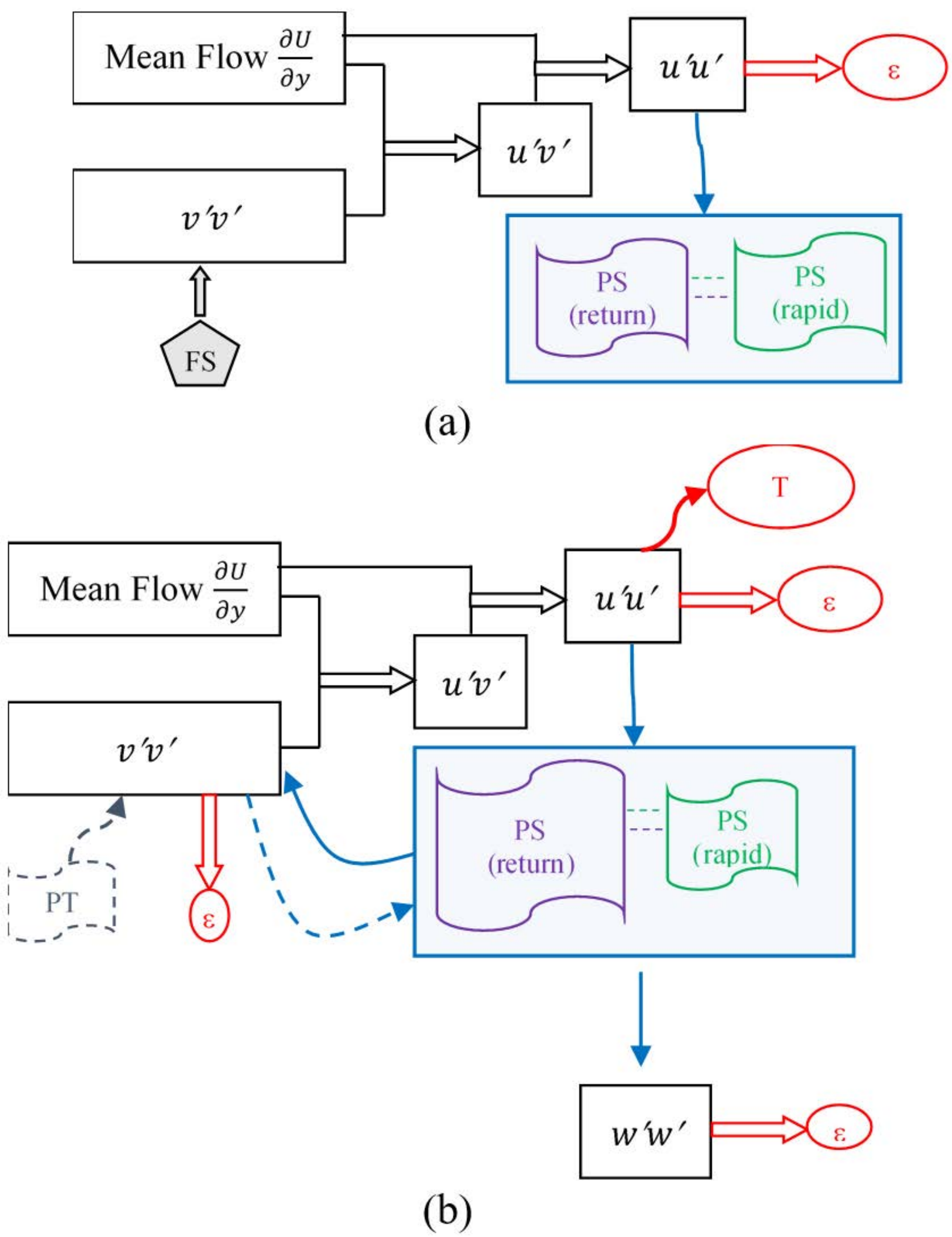

Figure 7. Schematic diagram showing energy transfer mechanism in (a) pre-transition region and (b) turbulent regimes. Dashed lines indicate behavior in the near-wall region ($y^+ < 10$). PT is pressure transport, PS is pressure-strain, and FS is freestream. The mechanism shown in the shaded Blue box is the role of the return (slow) and rapid pressure-strain terms.

ACKNOWLEDGEMENT

The effort at Mississippi State University was supported by NASA EPScoR Project Number 80NSSC17M0039. All simulations were performed on Talon and Shadow HPC systems at the High-Performance Computing Collaboratory, Mississippi State University.

REFERENCES

[1] Knisely, C.P., Haley, C. and Zhong, X. (2019). "Impact of Conical Hypersonic Boundary Layer Transition on Skin Drag and Heating," AIAA Scitech 2019 Forum, 7-11 January, San Diego, California.

[2] Morkovin, M. V., 1969, "On the Many Faces of Transition," *Viscous Drag Reduction*, pp. 1–31.

[3] Dick, E., and Kubacki, S., 2017, "Transition Models for Turbomachinery Boundary Layer Flows: A Review," International Journal of Turbomachinery, Propulsion and Power, **2**(2), p. 4.

[4] Zhao, Y., and Sandberg, R. D., 2020, "Bypass Transition in Boundary Layers Subject to Strong Pressure Gradient and Curvature Effects," Journal of Fluid Mechanics, **888**.

[5] Spalart, P. R., and Venkatakrishnan, V., 2016, "On the Role and Challenges of CFD in the Aerospace Industry," Aeronaut. J., **120**(1223), pp. 209–232.

[9] Wu, X., and Durbin, P. A., 2001, "Evidence of Longitudinal Vortices Evolved from Distorted Wakes in a Turbine Passage," J. Fluid Mech., **446**, pp. 199–228.

[10] Jacobs, R. G., and Durbin, P. A., 2001, "Simulations of Bypass Transition," J. Fluid Mech., **428**, pp. 185–212.

[11] Zaki, T. A., and Durbin, P. A., 2005, "Mode Interaction and the Bypass Transition Route to Transition," J. Fluid Mech., **531**(85–111), pp. 85–111.

[12] Schlatter, P., Brandt, L., de Lange, H. C., and Henningson, D. S., 2008, "On Streak Breakdown in Bypass Transition," *Physics of Fluids*, p. 101505.

[13] Wu, X., and Moin, P., 2009, "Direct Numerical Simulation of Turbulence in a Nominally Zero-Pressure-Gradient Flat-Plate Boundary Layer," J. Fluid Mech., **630**, pp. 5–41.

[14] Schlatter, P., Örlü, R., Li, Q., Brethouwer, G., Fransson, J. H. M., Johansson, A. V, Alfredsson, P. H., and Henningson, D. S., 2009, "Turbulent Boundary Layers up to Re= 2500 Studied through Simulation and Experiment," Phys. Fluids, **21**(5), p. 51702.

[15] Kendall, J., 1998, "Experiments on Boundary-Layer Receptivity to Freestream Turbulence," *36th AIAA Aerospace Sciences Meeting and Exhibit*, p. 530.

[16] Andersson, P., Berggren, M., and Henningson, D. S., 1999, "Optimal Disturbances and Bypass Transition in Boundary Layers," Phys. Fluids, **11**(1), pp. 134–150.

[17] Brandt, L., Schlatter, P., and Henningson, D. S., 2004, "Transition in Boundary Layers Subject to Free-Stream Turbulence," J. Fluid Mech., **517**, pp. 167–198.

[18] Muthu, S., and Bhushan, S., 2020, "Comparison between Temporal and Spatial Direct Numerical Simulations for Bypass Transition Flows," J. Turbul., **21**(5–6), pp. 311–354.

[19] Bhushan, S., and Muthu, S., 2019, "Parallel Performance Assessment of a Pseudo-Spectral Solver for Transition and Turbulent Boundary Layer Flows," Eng. Appl. Comput. Fluid Mech., **13**(1), pp. 763–781.

[20] Jacobs, R. G., and Durbin, P. A., 2001, "Simulations of Bypass Transition," J. Fluid Mech., **428**, pp. 185–212.

[21] Roach, P. E., and Brierley, D. H., 1990, "The Influence of a Turbulent Freestream on Zero Pressure Gradient Transitional Boundary Layer Development. Part 1: Test Cases T3A and T3B," *In Numerical Simulation of Unsteady Flows and Transition to Turbulence (Ed. O. Pironneau, W. Rodi, I. L. Ryhming, A. M. Savill & T. V. Truong)*, Cambridge University Press, pp. 319–347.

[22] Jimenez, J., Hoyas, S., Simens, M. P., and Mizuno, Y., 2010, "Turbulent Boundary Layers and Channels at Moderate Reynolds Numbers," J. Fluid Mech., **657**, pp. 335–360.

[23] Moser, R., Kim, J., and Mansour, N., 1999, "Direct Numerical Simulation of Turbulent Channel Flow up to Re_τ= 590," Phys. Fluids, **11**(4), pp. 943–945.

[24] Mayle, R. E., and Schulz, A., 1997, "The Path to Predicting Bypass Transition," J. Turbomach., **119**(3), pp. 405–411.

[25] Voke, P. R., and Yang, Z., 1995, "Numerical Study of Bypass Transition," Phys. Fluids, **7**(9), pp. 2256–2264.

[26] Lardeau, S., Li, N., and Leschziner, M. A., 2007, "Large Eddy Simulation of Transitional Boundary Layers at High Free-Stream Turbulence Intensity and Implications for RANS Modeling," J. Turbomach.

[27] He, S., and Seddighi, M., 2013, "Turbulence in Transient Channel Flow," J. Fluid Mech., **715**(60–102), pp. 60–102.

[28] Bhushan, S., Walters, K. D., Muthu, S., and Pasiliao, C. L., 2018, "Identification of Bypass Transition Onset Markers Using Direct Numerical Simulation," J. Fluids Eng., (140(11)), p. 111107.

[29] Landahl, M. T., 1980, "A Note on an Algebraic Instability of Inviscid Parallel Shear Flows," J. Fluid Mech., **98**(2), pp. 243–251.

[30] Savill, A., 2002, "New Strategies in Modelling Bypass Transition," *Closure Strategies for Turbulent and Transitional Flows*, Cambridge University Press, pp. 493–521.

[31] Muthu, S., Bhushan, S. and Walters, DK. Identification of a Pressure-Strain Correlation Based Bypass Transition Onset Marker. J. Fluids Eng., 143(10), 101501, 2021.

Plasmonic Nanomaterial for Rapid Naked Eye Diagnosis of COVID-19: Recent Progress and Opportunities

Avijit Pramanik, Ye Gao, Shamily Patibandla, Kalein Gates and Paresh Chandra Ray
Department of Chemistry and Biochemistry, Jackson State University, Jackson, MS, USA

Corresponding Author: Paresh Chandra Ray
Fax: +16019793674
E-mail: paresh.c.ray@jsums.edu
https://doi.org/10.31753/IJRD28760156

ABSTRACT

Infectious diseases by SARS-CoV-2 or coronavirus disease 2019 (COVID-19) is responsible for more than 2.5M death worldwide till today. Due to the COVID-19 pandemic situation there is an urgent need for a rapid, simple, and inexpensive point-of-care diagnosis and mass screening technique to save millions of human lives. Since Gold nanoparticles (GNPs) provide unique plasmonic optical properties and displaying different colors depending on their size, shape and state of aggregation, designing GNPs based colorimetric biosensor for COVID-19 became very attractive for real life application. In this review, we provide the advances on the development of antibody or aptamer conjugated plasmonic nanoparticle, which represent powerful platform for naked eye colorimetric detection, of COVID-19 antigen or viruses. Initially, we discuss the fundamental scientific strategy has been used to design colorimetric test assay using gold nanoparticle. We then highlighted current state-of-the-art progress towards the preliminary achievement of the gold nanoparticle based colorimetric assay for COVID-19 sensing from clinical sample. Finally, we discussed the advantages and major challenges for plasmonic nanoparticle based colorimetric assays in infectious diseases diagnosis.

Keywords:

COVID-19 and History of Pandemics

Over several centuries, pandemic caused by deadly viruses, bacteria, and different organisms are responsible for huge mortality in this world [1-10]. The very first pandemic, which is known in history was the plague struck the city of Athens in 430 BC (Before Christ), which killed 25% of the population in that city [1-4]. The next one was a Antonine plague in 165 AD (anno Domini), which killed 5M people[1-4]. Pandemics due to the Plague of Justinian (541–542 AD) killed 50 million people and Black Death (1346–1353) pandemics killed 200 million people, as well as smallpox pandemics (1852–1860) were responsible for 56 million of deaths worldwide[1-10]. Just around 100 years before, the 1918 influenza pandemic, killed around 500 million people, which was nearly 3% of the world's population at that time[5-15]. Just 40 years before, the AIDS (acquired immunodeficiency syndrome) epidemic started and it is responsible for more than 35 million death till today[1-10]. As of March 2020, the world is currently dealing with a global outbreak of by SARS-CoV-2 (COVID-19)[4-8]. Current pandemic has taken more than 2.6 M human life worldwide till now[12-32].

SARS-CoV-2 is spherical particle approximately 120 nm in diameter, as shown in Figure 1B, measured by transmission electron microscopy **(**TEM) techniques. SARS-CoV-2, a single-stranded RNA genome, belongs to the subfamily of coronavirus [15-32]. As shown in Figure 1A-1D, SARS-CoV-2 transcribes nine sub-genomic RNAs, and spike (S) proteins through which the virus spreads inside the cell via binding with angiotensin converting enzyme 2 (ACE-2) of cell's surface receptor[20-42].

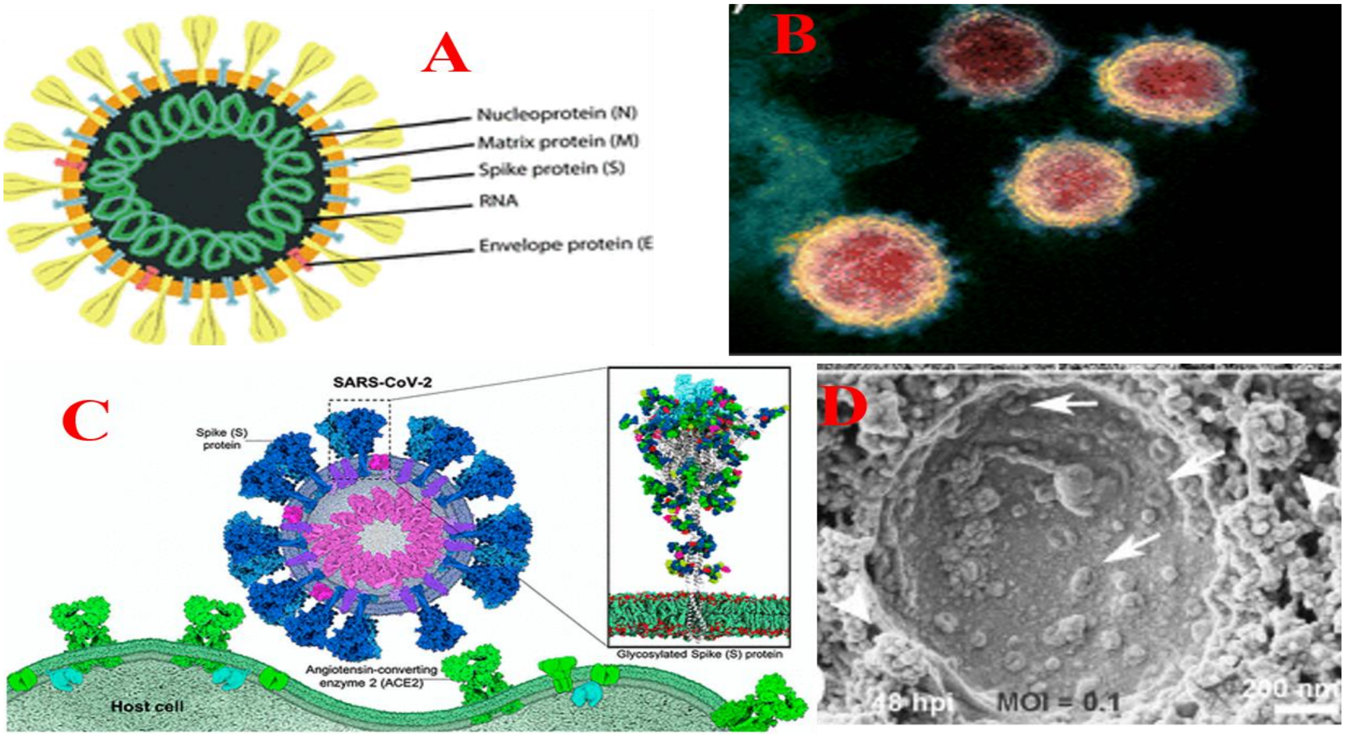

Figure 1: A) The schematic shows the SARS-CoV-2 structure with its structural viral proteins. Reproduced with permission from reference 21. Copyright 2020 American Chemical Society. B) Transmission electron microscopy (TEM) images of SARS-CoV-2. Reproduced with permission from reference 21. Copyright 2020 American Chemical Society. C) Molecular dynamic studies show how spike protein of COVID-19 interact with angiotensin-converting enzyme 2 (ACE2) of cells. Reproduced with permission from reference 16. Copyright 2020 American Chemical Society. D) SEM image shows COVID-19 virus can enter inside the cell via binding between spike protein and ACE2. Reproduced with permission from reference 15. Copyright 2020 Nature Publication.

Other important structural proteins for COVID-19 virus are envelope (E), membrane (M), and nucleocapsid (N) protein, as shown in Figure 1A [10-32]. Since infection spreads via S protein, all the vaccination now available in the market, target the S glycoproteins on the viral surface to disable receptor interactions [20-42]. Currently real-time reverse transcription-polymerase chain reaction (RT-PCR) are used for clinical diagnosis of SARS-CoV-2 infection in hospital and other clinical setting[10-30]. Although RT-PCR technique exhibits excellent accuracy, since the sequencing require long detection times (> 24 hours), which hinder the application of these methods for immediate detection, which is important for avoiding spreading in the society[10-30]. As a result, we and others have reported the development of nanomaterial based rapid and accurate diagnosis assay for COVID-19 antigen or virus which have capability to be used for avoiding virus spreads, even from asymptomatic carriers [20-42].

2. Nanomaterial based diagnostic platform for COVID-19

Recent advances in past few months from different groups have demonstrated that nanomaterial-based tools have capability to improve the speed, sensitivity, accuracy, and portability for COVID-19 detection[10-20]. For this purpose, different types of nanomaterial including plasmonic gold and silver nanoparticles, silica NPs, quantum dots (QDs), two-dimensional graphene have been considered seriously, as shown in Figure 2A-2E[20-40].

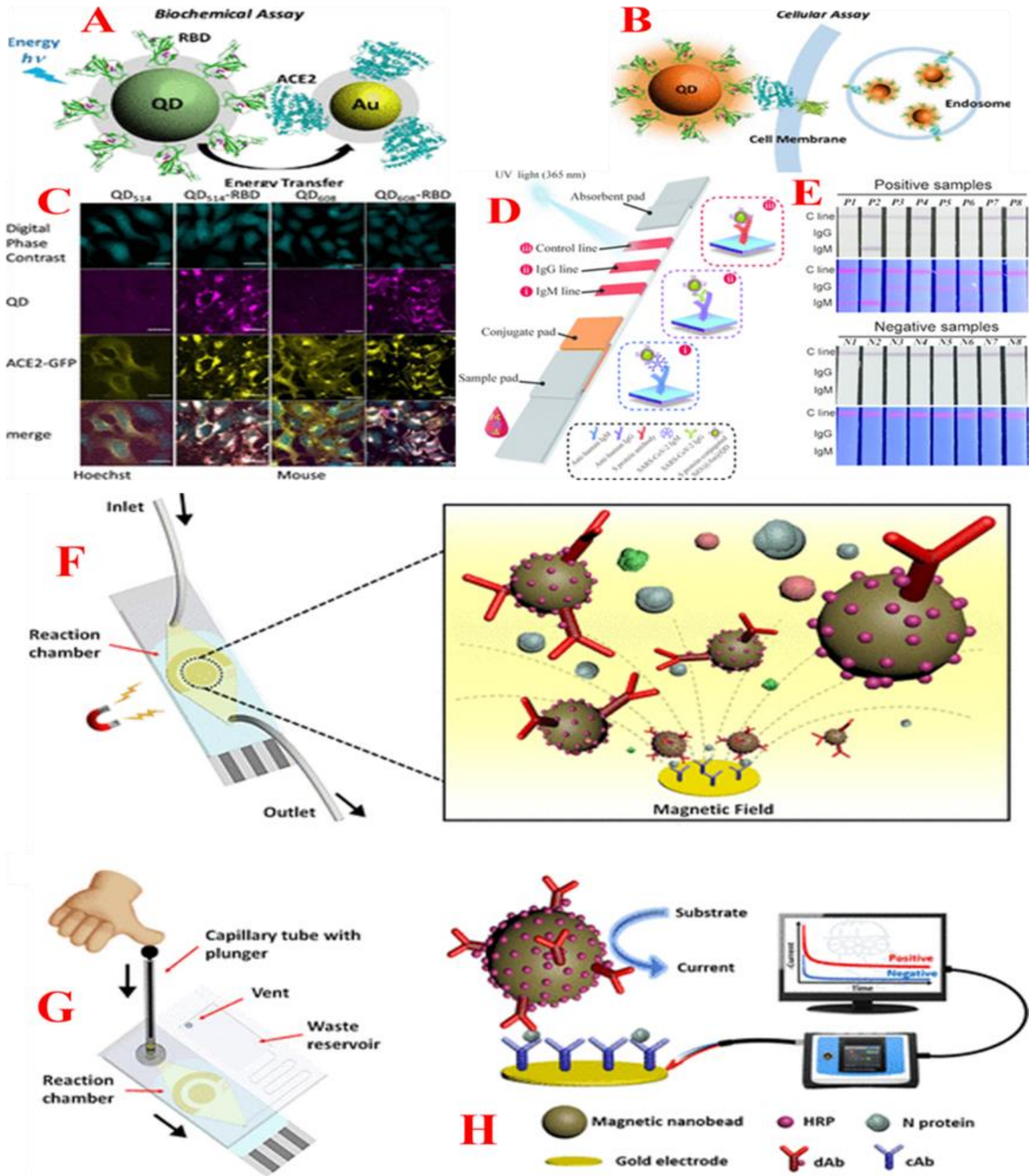

Figure 2: A) Scheme shows the biochemical assay using energy transfer from quantum dots conjugated spike protein receptor binding domain (QD-RBD) to gold nanoparticle conjugated host cell's angiotensin converting enzyme 2 (AuNP-ACE2. Reproduced with permission from reference 33. Copyright 2020 American Chemical Society. B) Scheme shows the cellular assay using QD-RBD interaction with ACE2 on the cell membrane. Reproduced with permission from reference 33. Copyright 2020 American Chemical Society. C) Fluorescence image of the montage of ACE2-GFP (yellow) HEK293T clone 2 treated with 100 nM QD_{514}-RBD (magenta) and QD_{608}-RBD (magenta). Reproduced with permission from reference 33. Copyright 2020 American Chemical Society. D) Scheme shows dual-mode gold-based lateral flow immunoassay LFIA biosensor. Reproduced with permission from reference 34. Copyright 2020 American Chemical Society. E) Photographs and fluorescence images of dual-mode LFIA applied in 8 positive serum specimens of patients with COVID-19 at different stages, shown in the top. Similarly, photographs and fluorescence images of dual-mode LFIA applied in 8negative serum specimens, shown in below. Reproduced with permission from reference 34. Copyright 2020 American Chemical Society. F) Scheme shows microfluidic immunosensor chip design for the magnetic concentration of dually-labeled magnetic nanobeads (DMBs) to the sensor surface. Reproduced with permission from reference 42. Copyright 2021 American Chemical Society. G) Scheme shows microfluidic immunosensor chip for the smartphone-based diagnostic device. Reproduced with permission from reference 42. Copyright 2021 American Chemical Society. H) Scheme shows the design of the electrochemical sensing scheme using the PalmSens4-based sensing platform. Reproduced with permission from reference 42. Copyright 2021 American Chemical Society.

Plasmonic nanoparticle-based SARS-CoV-2 antigen, antibody or virus detection techniques are developed using the unique optical properties, which is known as localized surface plasmon resonance (LSPR) [20-30]. In the next section, we will discuss how LSPS based assay have been developed for the detection of COVID-19. On the other hand, well-tailored emission characteristics and the ability to serve as a central anchor for multiple spike proteins, QD based fluorescence technique has been developed for COVID-19[30-40]. As shown in Figure 2A-2C, Gorshkov *et. al*. have demonstrated that QD nanoparticles labeled with SARS-CoV-2 virus Spike's S1 subunit receptor binding domain (RBD) can be used for effectively bind with host cell's angiotensin converting enzyme 2 (ACE2), as a result, it can be used as an efficient and facile biosensor assays for COVID-19 [33]. Similarly, as shown in Figure 2D-2E, Wang. et. al. designed dual-mode Colloidal gold (Au NP)-based lateral flow immunoassay LFIA biosensor for rapid and sensitive identification of SARS-CoV-2-specific IgM/IgG in clinical samples [34]. Reported data indicates that the sensitivity was obtained to be 100%, which indicate that the proposed method can be used for rapid and accurate screening of SARS-CoV-2 virus. Similarly, Zhong et. al. [41] reported rapid and sensitive detection of SARS-CoV-2 with functionalized magnetic nanoparticles (MNPs). In their reported data, functionalized MNPs were conjugated with SARS-CoV-2 spike proteins and used as sensors to detect a mimic virus. Li *et. al*. have reported a microfluidic immunosensor for rapid, high sensitivity measurements of SARS-CoV-2 N protein in serum [42]. As shown in Figure 2F-2H, for this purpose, they have used a unique sensing scheme employing dually-labeled magnetic nanobeads for immunomagnetic enrichment and signal amplification [42]. Reported data shows that the sensitivity for their assay can be as low as 10 pg/mL in 5× diluted serum within 30 min and 50 pg/mL in whole serum within 55 min [42].

Although all the above reported data are highly promising, to tackle COVID-19 pandemic for large amount of rapid testing is necessary where, easy-to-use colorimetric rapid diagnostic tests is very important for the society [20-30]. Plasmonic metal nanoparticle-based colorimetric sensors have become powerful tools for the detection of different targets with convenient readout[20-30]. Among the many types of plasmonic nanoparticles, gold nanoparticles based colorimetric assay exhibits extraordinary success which is mainly due to their localized surface plasmon resonance (LSPR) properties [40-54]. Details have been discussed in next section.

Plasmonic Gold Nanoparticle based Colorimetric assay for COVID-19 detection

Since mass testing is fundamental to tackle COVID-19 pandemic, we and others have designed easy-to-use bio-conjugated gold nanoparticles based colorimetric COVID-19 rapid diagnostic tests [12-30]. As we all know human eyes are only sensitive to visible color variations, GNP based -optical changes in the presence of COVID-19 are of great interest for clinical assay which can be performed by visual inspection[22-40]. Due to the ease of synthesis as well as the functionalization with aptamer/antibody/ peptide and biocompatibility, GNP has been used heavily in the development of newer diagnostic methods which are safer and easier than the conventional existing methods[12-30]. Since gold nanoparticle exhibit unique localized surface plasmon resonance (LSPR) optical properties, as well as the stability in biological media, we and others have reported GNPs based assay for the specific identification of viruses, bacteria and cancer[42-54]. As it is now well documented that the visible absorption optical properties of gold nanoparticles are due to the effect of boundary conditions of the coherent electron oscillations [43-54]. The LSPR response for plasmonic gold nanoparticles arises from the interaction between the electric field of the incident light and the surface conduction electrons on metal nanoparticle lattice[43-54]. The above interaction varies with nanoparticle composition, size, shape and the local refractive index[43-54]. Gold nanoparticle based colorimetric assay's working principle for CIVID-19 is based on LSPR properties GNPs. As we and others have reported before, LSPR coupling among the nanoparticles can be manipulated by changing the distance between GNPs or by varying the degree of aggregation of GNPs[43-54]. As shown in Figure 3A-3C, we have designed GNP dimmer at different separation distance for monomer via double stand DNA (ds-DNA) spacers .[43-48]. We have also reported theoretical finite difference time domain (FDTD) simulation investigation for the GNP dimer coupling, as shown in

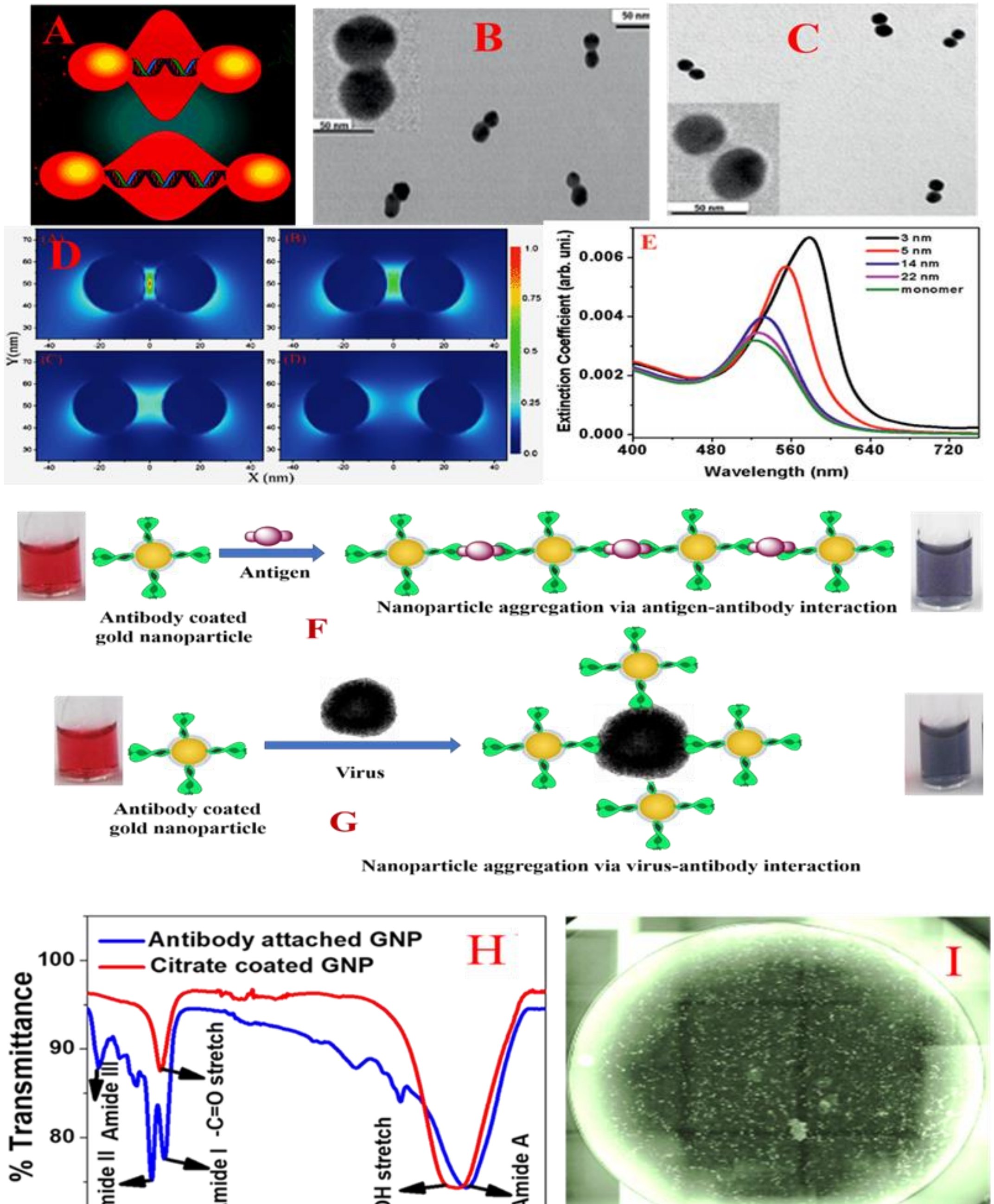

Figure 3: A) Scheme shows the design of gold nanoparticle dimmer where the monomer is separated by double stand DNA. B) TEM image of GNP dimmer, with 3 nm separation between two individual nanoparticles when they are separated by thiolated 4 bp ds-DNA. C) TEM image of GNP dimmer with 8 nm separation between two individual nanoparticles, when they are separated by thiolated 20 bp ds-DNA. D) FDTD simulations shows electric field distribution for GNP nano-dimmer with different spacing. E) Simulated extinction spectra for GNP monomer and GNP dimmer with different spacing. F) Scheme shows that in the presence of antigen, due to the antigen-antibody interaction gold nanoparticle aggregates (inserted picture shows the color of antibody attached gold nanoparticle in the presence of antigen). G) Scheme shows that in the presence of virus, due to the antigen-antibody interaction gold nanoparticle aggregates on the surface of virus (inserted picture shows the color of antibody attached gold nanoparticle in the presence of virus). H) FTIR spectra from citrate coated gold nanoparticle and antibody attached GNPs. I) SARS-CoV-2 pseudovirus green fluorescent protein (GFP) expression in infected HEK293T cells in the presence of gold nanoparticle. (Figures A, B, C, D, E Reproduced with permission from reference 43. Copyright 2015 Royal Society of Chemistry. Figures F, G, H Reproduced with permission from reference 28. Copyright 2021 Royal Society of Chemistry)

Figure 3D [43]. As shown in Figure 3E, theoretical FDTD and experimental data indicates that the plasmonic resonance occurs near 528 nm in the single nanoparticle[43]. On the other hand, in case dimmer, the plasmonic absorption maxima is highly depends on the distances of individual gold nanoparticle[43]. Since the color of the GNP changes with distance between two nanoparticles, by varying the nanoparticle aggregation, color of the GNP can be manipulated from red to blue[43]. The above phenomena have been used for the design of the aggregation based colorimetric identification of viruses[25-30]. Since GNP based colorimetric assay is very simple and visual output can be monitored using naked eye, we and others have developed colorimetric assay for COVID-19 antigen, antibodies and virus itself using bio-conjugated GNPs [25-30].

For this purpose, initially citrate coated gold nanoparticles were synthesized using $HAuCl_4$, $3H_2O$ and sodium citrate, as we and others have reported before **[45-51].** After that we have developed biocompatible gold nanoparticles and for this purpose nanoparticles were coated with SH-PEG–CO_2H. In this case, we have used Carboxy-PEG_{12}-Thiol, (HS-PEG_{12}-COOH). Experimental details have been reported before [28]. In the next step, for targeted diagnosis, we have developed anti-spike antibody attached gold nanoparticle. For this purpose, we have used EDC (1-ethyl-3-(3-dimethylaminopropyl)-carbodiimide)/NHS (N-hydroxysuccinimide) chemistry has been used. Experimental details have been reported before [28].

Fourier transform infrared (FTIR) spectra from anti-spike-antibody attached gold nanoparticle reported in Figure 3E, shows the presence of Amide-A, Amide-I, Amide-II and Amide-II bands, which indicates that anti-spike-antibody are attached on gold nanoparticle surface [28].

To determine possible toxicity from PEG conjugated and unconjugated gold nanoparticles in COVID-19 biological media, HEK293T cells (ATCC # CRL3216) were plated on a 96-well plate in complete media (DMEM + 10% FBS) and incubated under normal growth conditions (5% CO_2 and 37°C, protected from light) for 12-24 hours [28]. Experimental details have been reported before [28]. After that the pseudovirus stock (2.5 µl of the $2X10^{10}$ units/ml stock) was mixed with the diluted nanoparticles and incubated for 1 h at 37°C, then laid over HEK293T cells plated in the 96-well tissue culture dishes, along with 0.6 µL of the 500 nM Sodium Butyrate (to give a final concentration of 2mM). Plates were incubated at 37°C and 5% CO_2 for 48 h. Cells were fixed in 3.7% formaldehyde and the assay was read on Cytation 5 automated fluorescent microscope (BioTek Instruments, Inc., Winooski, VT, USA) [28]. Experimental details have been reported before [28]. As shown in Figure 3I, we have not observed any toxicity from unconjugated gold nanoparticle. Similarly, we have not observed any toxicity from PEG coated gold nanoparticle.

As shown in Figure 3F-3G, the working principle for anti-spike antibody attached GNP based colorimetric assay for COVID-19 antigen is based on the fact that, in the presence of SARS-CoV-2 spike recombinant antigen, due to the antigen-antibody interaction, anti-spike antibody attached GNP aggregates [28]. As a result, a colorimetric change from purple to bluish color is observed with naked eyes, as shown in Figure 4A-4E[28].

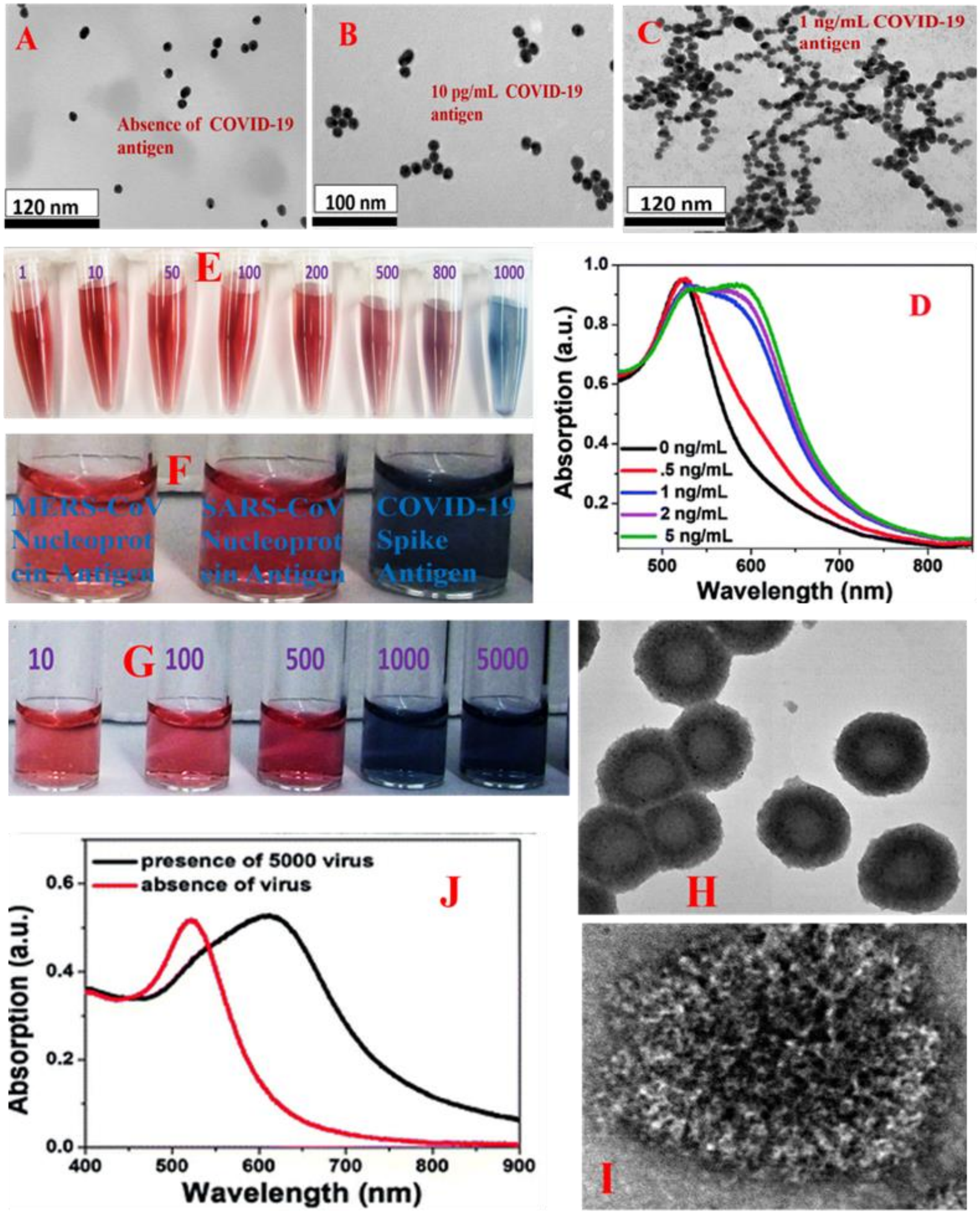

Figure 4: A) TEM shows the morphology of anti-spike antibody attached gold nanoparticle in the absence of COVID-19 antigen.. B) TEM shows the morphology of antibody attached GNPs in the presence of 10 pg/mL of COVID-19 antigen (COVID-19 Spike Recombinant Antigen. C) TEM shows the morphology of antibody attached GNPs in the presence of 1 ng/mL of COVID-19 antigen. D) Absorption spectra from antibody attached GNPs in the presence of different concentrations of COVID-19 antigen. (E) The color of antibody attached GNPs in the presence of different amounts of COVID-19 antigen from 1 pg mL^{-1} to 1000 pg mL^{-1}. (F) Selectivity of the anti-spike antibody attached gold nanoparticle-based colorimetric assay for COVID-19 antigen (5 ng mL^{-1}). G) Changes in the color of antibody attached GNPs in the presence of different amounts of pseudo SARS-CoV-2 (10–5000 virus particles per mL). H) A TEM image showing the morphology of pseudo SARS-CoV-2, which we used for virus diagnosis.. I) A TEM image showing the morphology of anti-spike antibody attached gold nanoparticle conjugated pseudo SARS-CoV-2 when we used 800 pM gold nanoparticles J) Variations in the absorption spectrum of antibody attached GNPs in the presence and absence of pseudo SARS-CoV-2. Figures A, B, C, E, F, G, H, I, and J are reproduced with permission from reference 28. Copyright 2021 Royal Society of Chemistry.

The observed color change, as shown in Figure 4E, is mainly due to the surface plasmon coupling between anti-spike antibody attached gold nanoparticles[28]. Reported experimental data shows that naked eye colorimetric diagnosis of COVID-19 antigens using anti-spike antibody attached gold nanoparticles is very quick and it takes less than 5 minutes to get the result[28]. As shown in Figure 4D, due to the aggregation of gold nanoparticles a red shift of the absorption spectra from 520 to 600 nm has been observed[28]. Sensitivity of naked eye colorimetric assay for COVID-19 antigen was reported to be 1ng/mL antigen[28]. Similarly, selectivity of the naked eye colorimetric assay was demonstrated using severe acute respiratory syndrome coronavirus (SARS-CoV) and Middle East respiratory syndrome coronavirus (MERS-CoV) antigen, as shown in Figure 4F[28].

As shown in the Figure 4G, reported naked eye colorimetric diagnosis of SARS-CoV-2 using anti-spike antibody attached GNPs is based on the fact that in the presence of virus, due to the spike protein–antibody interaction, antibody attached GNPs aggregate on the surface of the virus[28]. As shown in the Figure 4H-4I, since the size of the pseudo SARS-CoV-2 is around 120–160 nm, on the other hand GNPs are around 30 nm, as a result, several antibody attached GNPs can aggregate on the surface of each virus particle[28]. Due to the above discussed aggregation, we observed the color of the suspension of antibody attached GNPs change from pink to blue, as shown in Figure 4G[28]. Due to the aggregation of GNPs on virus surface, as shown in Figure 4J, the absorption spectra exhibit a red shift of from 520 to 640 nm. Reported data indicates that GNPs based virus detection is very quick and it takes less than 5 minutes to get the results[28]. As shown in Figure 4G, the sensitivity of naked eye colorimetric assay for the identification of pseudo-SARS-CoV-2 was determined to be 1000 virus particles/ml[28].

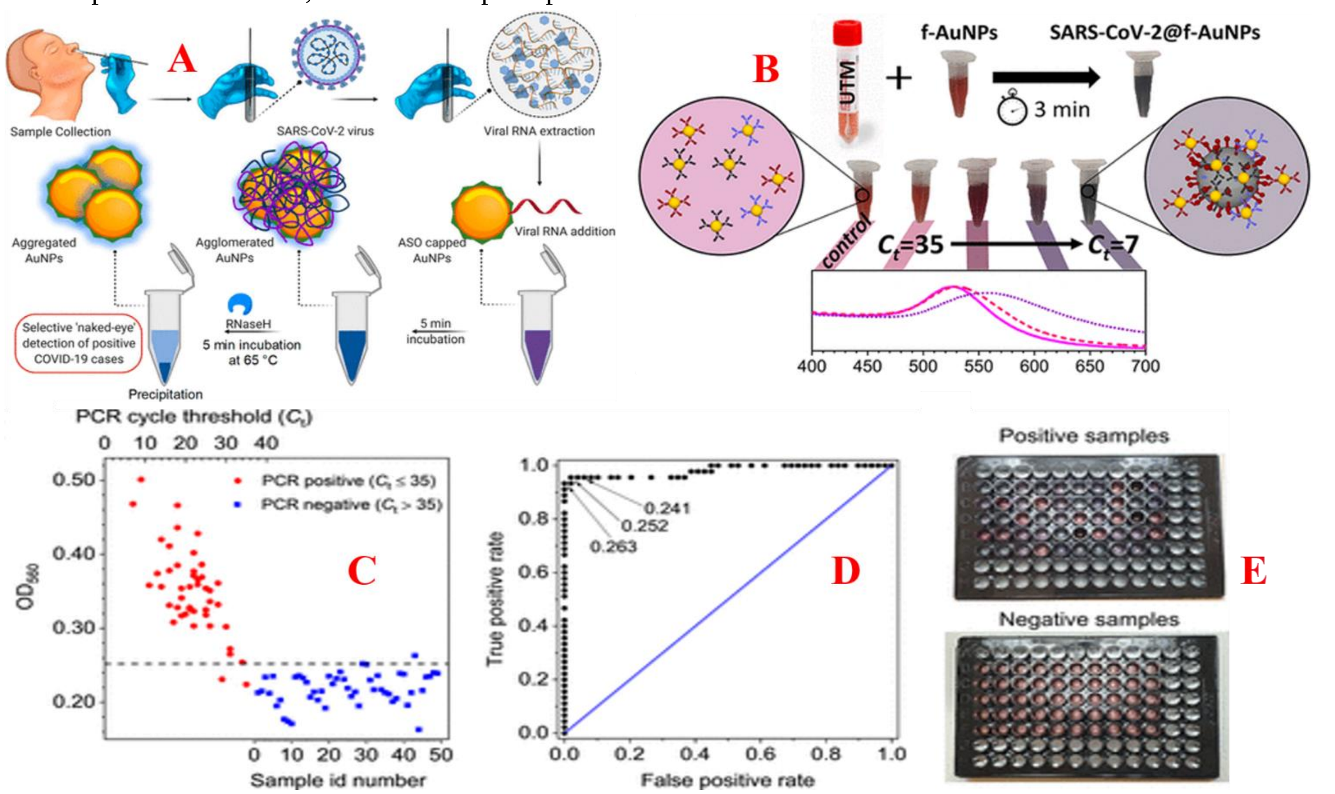

Figure 5: A) Scheme shows the Selective Naked-Eye Detection of SARS-CoV-2 RNA Mediated by the Suitably Designed ASO-Capped AuNPs. Reproduced with permission from reference 22. Copyright 2020 American Chemical Society. B) Scheme shows anti-spike, anti-membrane, and anti-envelope antibody attached GNP based Naked-Eye Detection of SARS-CoV-2 from clinical sample. Reproduced with permission from reference 27. Copyright 2020 American Chemical Society. C) Results of the colorimetric test on real thawed samples from 45 positive (red circle points) and 49 negative patients (blue square points) previously tested by real-time PCR. Reproduced with permission from reference 27. Copyright 2020 American Chemical Society. D) The receiver operating characteristic (ROC) curve retrieved from the data of the panel. E) Picture of the 96 multiwell plate containing 250 µL of positive (top panel) and negative (bottom panel) samples. The plate reading was carried out by a commercial multiwell reader that took less than 1 min. Reproduced with permission from reference 27. Copyright 2020 American Chemical Society.

Moitra et. al. reported [22] the development of a colorimetric naked eye assay for *N*-gene of SARS-CoV-2 viral genome detection using plasmonic properties of gold nanoparticles, as shown in Figure 5A. In their design they have utilized the thiol-modified antisense oligonucleotides (ASOs) sequences covering two regions of the viral genome sequence[22]. Their reported data shows that colorimetric naked eye assay can be used for diagnosing positive COVID-19 cases within 10 min from the total RNA isolated from the infected bio-samples[22]. They have demonstrated the selectivity against MERS-CoV viral RNA load where no distinct change in absorbance was found. Similarly, Ventural et. al. have reported a colorimetric biosensor based on 20 nm GNPs attached with antibody against spike, envelope, and membrane protein of SARS-CoV-2, as shown in Figure 5B-5E [27]. Their reported data shows that the naked eye colorimetric data are comparable with a real-time PCR data which are used in clinics[27].

CONCLUSIONS AND OUTLOOK

In this review article we have summarized recent efforts to design naked eye colorimetric assays using GNP for the identification of SARS-CoV-2 antigen and virus. Although the reported data looks very encouraging, we have to admit that material design for combating COVID-19 is still in its infancy, which started less than a year before. As a result, the works presented here is the initial steps towards the new development. We expect that new novel bio-conjugated material will be discovered in the near future, which will be able translate the research from laboratory to clinics for personalized healthcare. Despite the considerable achievements, the major fundamental challenges are the development of cost-effective, biocompatible and environmentally friendly nanomaterials for real-life infectious disease marker sensing application. For this purpose, collaborative effort between academia, industry as well as government sector are very important for future innovation.

ACKNOWLEDGEMENTS

Dr. Ray is supported by NSF-RAPID grant # DMR-2030439, NSF-PREM grant # DMR-1826886 and NIH-NIMHD grant # 1U54MD015929-01.

REFERENCES

1. Morens, D. M; Folkers, G. K; Fauci, A. S..; Emerging infections: a perpetual challenge. *Lancet Infect Dis* **2008**, 8, 710–719.
2. Crosby AW. America's Forgotten Pandemic: The Influenza of 1918. Cambridge, UK: Cambridge University Press; 1989. p. 66.
3. Evans RJ. Death in Hamburg: Society and Politics in the Cholera Years, 1830–1910. New York: Penguin Books; 2005.
4. Grmek MD, editor; History of AIDS: Emergence and Origin of a Modern Pandemic. Princeton, NJ: Princeton University Press; 1990.
5. Centers for Disease Control and Prevention. Coronavirus Disease 2019 (COVID-19) Situation Summary. Published 2020 March 27 CDC.gov; Available at: https://www.cdc.gov/coronavirus/2019-ncov/cases-updates/summary.htm
6. Centers for Disease Control and Prevention. Interim Pre-Pandemic Planning Guidance: Community Strategy for Pandemic Influenza Mitigation in the United States: Early, Targeted, Layered Use of Nonpharmaceutical Interventions. 2007CDC; Available at: https://stacks.cdc.gov/view/cdc/11425.
7. Huremović, D. Brief History of Pandemics (Pandemics Throughout History). *Psychiatry Pandemics* **2019**, 7–35
8. Jones, D.S. History in a Crisis—Lessons for Covid-19. *N. Engl. J. Med.* **2020**, *382*, 1681–1683.
9. Wang, C.; Horby, P. W.; Hayden, F. G.; Gao, G. F. A novel coronavirus outbreak of global health concern. *Lancet* **2020**, *395*, 470– 473
10. Gates, B. Responding to Covid-19—A Once-in-a-Century Pandemic?. *N. Engl. J. Med.* **2020**, *382*, 1677– 1679
11. Zhang, L.; Lin, D.; Sun, X.; Curth, U.; Drosten, C.; Sauerhering, L.; Becker, S.; Rox, K.; Hilgenfeld, R. Crystal Structure of SARS-CoV-2 Main Protease Provides a Basis for Design of Improved α-Ketoamide Inhibitors. *Science* **2020**, *368*, 409– 412
12. Watanabe, Y.; Allen, J. D.; Wrapp, D.; McLellan, J. S.; Crispin, M. Site-specific glycan analysis of the SARS-CoV-2 spike. *Science* **2020**, *369*, 330– 333,
13. Wang, Y.; Liu, M.; Gao, J. Enhanced receptor binding of SARS-CoV-2 through networks of hydrogen-bonding and hydrophobic interactions. *Proc. Natl. Acad. Sci. U. S. A.* **2020**, *117*, 13967– 13974
14. Hoffmann M., et al., SARS-CoV-2 Cell Entry Depends on ACE2 and TMPRSS2 and Is Blocked by a Clinically Proven Protease Inhibitor. *Cell*, 2020. 181(2): p. 271–280.e8
15. Caldas L.A., et al., Ultrastructural analysis of SARS-CoV-2 interactions with the host cell via high resolution scanning electron microscopy. *Scientific Reports*, 2020. 10, 16099
16. P. R. Arantes , A. Saha and G. Palermo , Fighting COVID-19 Using Molecular Dynamics Simulations, *ACS Cent. Sci.*, 2020, **6** , 1654 —1656

17. Thanh Le, T.; Andreadakis, Z.; Kumar, A.; Gómez Román, R.; Tollefsen, S.; Saville, M.; Mayhew, S. The COVID-19 Vaccine Development Landscape. *Nat. Rev. Drug Discovery* **2020**, 19 (5), 305– 306
18. Tang, Z.; Kong, N.; Zhang, X.; Liu, Y.; Hu, P.; Mou, S.; Liljeström, P.; Shi, J.; Tan, W.; Kim, J. S.; Cao, Y.; Langer, R.; Leong, K. W.; Farokhzad, O. C.; Tao, W. A Materials-Science Perspective on Tackling COVID-19. *Nat. Rev. Mater.* **2020**, *5*, 847– 860
19. Wang, C.; Li, W.; Drabek, D.; Okba, N. M. A.; van Haperen, R.; Osterhaus, A. D. M. E.; van Kuppeveld, F. J. M.; Haagmans, B. L.; Grosveld, F.; Bosch, B.-J. A human monoclonal antibody blocking SARS-CoV-2 infection. *Nat. Commun.* **2020**, *11* (1), 1– 6
20. Huang, H. Y.; Fan, C. H.; Li, M.; Nie, H. L.; Wang, F. B.; Wang, H.; Wang, R.; Xia, J. B.; Zheng, X.; Zuo, X. L.; Huang, J. X. Covid-19: A Call for Physical Scientists and Engineers. *ACS Nano* **2020**, *14*, 3747– 3754,
21. Medhi. R.; Srionoi, P.; Ngo, N.; Tan, H.; Lee, T. R.; Nanoparticle-Based Strategies to Combat COVID-19, *ACS Appl. Nano Mater.* **2020**, 3, 9, 8557–8580
22. Moitra, P.; Alafeef, M.; Dighe, K.; Frieman, M. B.; Pan, D. Selective Naked-Eye Detection of SARS-CoV-2 Mediated by N Gene Targeted Antisense Oligonucleotide Capped Plasmonic Nanoparticles. *ACSNano* **2020**, *14*, 7617– 7627
23. Seo, G.; Lee, G.; Kim, M. J.; Baek, S. H.; Choi, M.; Ku, K. B.; Lee, C. S.; Jun, S.; Park, D.; Kim, S. J.; Lee, J. O.; Kim, B. T.; Park, E. C.; Kim, S. Rapid Detection of COVID-19 Causative Virus (SARS-CoV-2) in Human Nasopharyngeal Swab Specimens Using Field-Effect Transistor-Based Biosensor. *ACS Nano* **2020**, *14*, 5135– 5142
24. Zhang, Q.; Honko, A.; Zhou, J.; Gong, H.; Downs, S. N.; Vasquez, J. H.; Fang, R. H.; Gao, W.; Griffiths, A.; Zhang, L. Cellular Nanosponges Inhibit SARS-CoV-2 Infectivity. *Nano Lett.* **2020**, *20*, 5570-5574
25. Zhang, Q.; Honko, A.; Zhou, J.; Gong, H.; Downs, S. N.; Vasquez, J. H.; Fang, R. H.; Gao, W.; Griffiths, A.; Zhang, L. Cellular Nanosponges Inhibit SARS-CoVInfectivity. *NanoLett.* **2020**, *20*, 5570– 5574
26. Talebian, S.; Wallace, G. G.; Schroeder, A.; Stellacci, F.; Conde, J. Nanotechnology-Based Disinfectants and Sensors for SARS-CoV-2. *Nat. Nanotechnol.* **2020**, *15* (8), 618– 621
27. Ventura B Della, Cennamo M, Minopoli A, Campanine, R.; Censi, B. S: Terracciano, D.; Portella, G.; Velotta, R.; Colorimetric Test for Fast Detection of SARS-CoV-2 in Nasal and Throat Swabs. *ACS sensors* **2020**, 5, 3043–3048
28. Pramanik, A.; Gao, Y.; Patibandla S.; Mitra , D.; McCandless , M. G.; Fassero, L. A.; Gates , K.; Tandon , R.; and Ray, P. C.; Rapid Diagnosis and Effective Inhibition of Corona Virus Using Spike Antibody Attached Gold Nanoparticle, *Nanoscale Advances*, **2021**, DOI: 10.1039/D0NA01007C
29. Pramanik, A.; Gao, Y.; Patibandla S.; Mitra , D.; McCandless , M. G.; Fassero, L. A.; Gates , K.; Tandon , R.; and Ray, P. C.; Aptamer Conjugated Gold Nanostar-Based Distance-Dependent Nanoparticle Surface Energy Transfer Spectroscopy for Ultrasensitive Detection and Inactivation of Corona Virus, *J. Phys. Chem. Lett.* **2021**, 12 (ASAP Article).
30. Alafeef, M.; Dighe, K.; Moitra, P.; Pan. D.; Rapid, Ultrasensitive, and Quantitative Detection of SARS-CoV-2 Using Antisense Oligonucleotides Directed Electrochemical Biosensor Chip. *ACS Nano* **2020**, 14, 17028–17045
31. Y.; Jiao, Y.-J. Rapid Detection of IgM Antibodies against the SARS-CoV-2 Virus via Colloidal Gold Nanoparticle-Based Lateral-Flow Assay. *ACS Omega* **2020**, *5*, 12550
32. Song, Y.; Song, J.; Wei, X.; Huang, M.; Sun, M.; Zhu, L.; Lin, B.; Shen, H.; Zhu, Z.; Yang, C. Discovery of Aptamers Targeting the Receptor-Binding Domain of the SARS-CoV-2 Spike Glycoprotein. *Anal. Chem.* **2020**, *92*, 9895– 9900
33. Gorshkov, K.; Susumu, K.; Chen, J.; Xu, M.; Pradhan, M.; Zhu, W.; Hu, X.; Breger, J. C.; Wolak, M.; Oh, E. Quantum-Dot-Conjugated SARS-CoV-2 Spike Pseudo-Virions Enable Tracking of Angiotensin Converting Enzyme 2 Binding and Endocytosis. *ACS Nano* **2020**, *14* (9), 12234– 12247
34. Wang, C.; Yang, X.; Gu, B.; Liu, H.; Zhou, Z.; Shi, L.; Cheng, X.; Wang, S.; Sensitive and Simultaneous Detection of SARS-CoV-2-Specific IgM/IgG Using Lateral Flow Immunoassay Based on Dual-Mode Quantum Dot Nanobeads, *Anal. Chem.* **2020**, 92, 23, 15542–15549
35. Forssén, P.; Samuelsson, J.; Lacki, K.; Fornstedt, T. Advanced Analysis of Biosensor Data for SARS-CoV-2 RBD and ACE2 Interactions. *Anal. Chem.* **2020**, *92* (17), 11520– 11524
36. Qiu, G.; Gai, Z.; Tao, Y.; Schmitt, J.; Kullak-Ublick, G. A.; Wang, J. Dual-Functional Plasmonic Photothermal Biosensors for Highly Accurate Severe Acute Respiratory Syndrome Coronavirus 2 Detection. *ACS Nano* **2020**, *14* (5), 5268– 5277
37. Broughton, J. P.; Deng, X.; Yu, G.; Fasching, C. L.; Servellita, V.; Singh, J.; Miao, X.; Streithorst, J. A.; Granados, A.; Sotomayor-Gonzalez, A.; Zorn, K.; Gopez, A.; Hsu, E.; Gu, W.; Miller, S.; Pan, C.-Y.; Guevara, H.; Wadford, D. A.; Chen, J. S.; Chiu, C. Y. CRISPR–Cas12-Based Detection of SARS-CoV-2. *Nat. Biotechnol.* **2020**, *38*, 870– 874,
38. Xu, X.; Sun, J.; Nie, S.; Li, H.; Kong, Y.; Liang, M.; Hou, J.; Huang, X.; Li, D.; Ma, T.; Peng, J.; Gao, S.; Shao, Y.; Zhu, H.; Lau, J. Y.; Wang, G.; Xie, C.; Jiang, L.; Huang, A.; Yang, Z.; Zhang, K.; Hou, F. F. Seroprevalence of immunoglobulin M and G antibodies against SARS-CoV-2 in China. *Nat. Med.* **2020**, *26*, 1193– 1195

39. Chen, Z.; Zhang, Z.; Zhai, X.; Li, Y.; Lin, L.; Zhao, H.; Bian, L.; Li, P.; Yu, L.; Wu, Y.; Lin, G. Rapid and Sensitive Detection of anti-SARS-CoV-2 IgG, Using Lanthanide-Doped Nanoparticles-Based Lateral Flow Immunoassay. *Anal. Chem.* **2020**, *92*, 7226– 7231
40. Li, Z.; Yi, Y.; Luo, X.; Xiong, N.; Liu, Y.; Li, S.; Sun, R.; Wang, Y.; Hu, B.; Chen, W.; Zhang, Y.; Wang, J.; Huang, B.; Lin, Y.; Yang, J.; Cai, W.; Wang, X.; Cheng, J.; Chen, Z.; Sun, K.; Pan, W.; Zhan, Z.; Chen, L.; Ye, F. Development and Clinical Application of A Rapid IgM-IgG Combined Antibody Test for SARS-CoV-2 Infection Diagnosis. *J. Med. Virol.* **2020**, *92*, 1518– 1524
41. Zhong, J.; Rosch, L. E.; Viereck, T.; Schilling, M.; Ludwing, F.; Toward Rapid and Sensitive Detection of SARS-CoV-2 with Functionalized Magnetic Nanoparticles, *ACS Sens.* **2021**(ASAP Article)
42. Li, J.; Lillehoj, P.: Microfluidic Magneto Immunosensor for Rapid, High Sensitivity Measurements of SARS-CoV-2 Nucleocapsid Protein in Serum, *ACS Sens.* **2021**, ASAP Artcile
43. Sinha, S. S.; Paul, D. K.; Kanchanapally, R.; Pramanik, A.; Chavva, S. R.; Nellore, B. P. V.; Jones, S. J.; Ray, P. C. Long-range Two-photon Scattering Spectroscopy Ruler for Screening Prostate Cancer Cells, *Chem. Sci.* **2015**, 6, 2411– 2418
44. DeRussy, B. M., Aylward, M. A., Fan, Z., Ray, P. C. & Tandon, R. Inhibition of cytomegalovirus infection and photothermolysis of infected cells using bioconjugated gold nanoparticles. *Sci. Rep.* **2014**, 4, 5550.
45. Sinha, S. S.; Jones, S.; Pramanik, A.; Ray, P. C. Nanoarchitecture Based SERS for Biomolecular Fingerprinting and Label-Free Disease Markers Diagnosis. *Acc. Chem. Res.* **2016**, *49*, 2725– 2735
46. Paul, A. M.; Fan, Z.; Sinha, S. S.; Shi, Y.; Le, L.; Bai, F.; Ray, P. C. Bioconjugated Gold Nanoparticle Based SERS Probe for Ultrasensitive Identification of Mosquito-Borne Viruses Using Raman Fingerprinting. *J.Phys. Chem C* **2015**, *119*, 23669– 23675
47. Fan, Z.; Yust, B.; Nellore, B. P. V.; Sinha, S. S.; Kanchanapally, R.; Crouch, R. A.; Pramanik, A.; Chavva, S. R.; Sardar, D.; Ray, P. C. Accurate Identification and Selective Removal of Rotavirus Using a Plasmonic-Magnetic 3D Graphene Oxide Architecture. *J. Phys. Chem. Lett.* **2014**, *5*, 3216– 3221
48. Wang, S., Sing, A. K.; Senapati, D.; Neely, A.; Yu, H.; Ray, P. C.; Rapid colorimetric identification and targeted photothermal lysis of *Salmonella* bacteria by using bioconjugated oval-shaped gold nanoparticles. *Chem. Eu. J.* **2010**, 16, 5600–5606.
49. Singh, A. K.; Khan, S. A.; Fan, Z.; Demeritte, T.; Senapati, D.; Kanchanapally, R.; Ray, P. C. Development of a Long-Range Surface-Enhanced Raman Spectroscopy Ruler. *J. Am. Chem. Soc.* **2012**, *134*, 8662– 8669,
50. Pramanik, A.; Davis, D.; Patibandla, S; .; Begum, S, Ray, P.; Gates, K.; Gao, Y.; Ray, P. C.WS2-Gold Nanoparticle Heterostructures Based Novel SERS Platform for Rapid Identification of Antibiotic-Resistant Pathogen**s,** *Nanoscale Adv.*, **2020**, 2, 2025-2033
51. Vangara, A.; Pramanik, A,; Gao, Y.; Gates, K.; Begum, S.; Ray, P. C.; Fluorescence Resonance Energy Transfer Based Highly Efficient Theranostic Nanoplatform for Two-Photon Bioimaging and Two-Photon Excited Photodynamic Therapy of Multiple Drug Resistance Bacteria, *ACS Appl. Bio Mater.*, **2018**, *1*, 298–309
52. Ding, S.-Y.; You, E.-M.; Tian, Z.-Q.; Moskovits, M. Electromagnetic theories of surface-enhanced Raman spectroscopy. *Chem. Soc. Rev.* **2017**, *46*, 4042– 4076,
53. Reguera, J.; Langer, J.; Jiménez de Aberasturi, D.; Liz-Marzán, L. M. Anisotropic Metal Nanoparticles for Surface Enhanced Raman Scattering. *Chem. Soc. Rev.* **2017**, *46*, 3866– 3885,
54. Cardinal, M. F.; Vander Ende, E.; Hackler, R. A.; McAnally, M. O.; Stair, P. C.; Schatz, G. C.; Van Duyne, R. P. Expanding Applications of SERS Through Versatile Nanomaterials Engineering. *Chem. Soc. Rev.* **2017**, *46*, 3886– 3903.

Engineering Pseudoviruses to Study Antibody Responses and Antiviral Screening against SARS-CoV-2

Ritesh Tandon

Center for Immunology and Microbial Research; Department of Medicine,
University of Mississippi Medical Center, Jackson, MS 39216.

Corresponding Author: Ritesh Tandon
E-mail:rtandon@umc.edu
https://doi.org/10.31753/IJRD28760167

ABSTRACT

The Severe Acute Respiratory Syndrome Coronavirus 2 (SARS-CoV-2) has caused a pandemic of unprecedented size in modern history. The rapid development of several different types of vaccines against SARS-CoV-2 in a record time offers hope that the pandemic will be controlled in near future (1-4). However, the emergence of B.1.1.7 (United Kingdom), B.1.351 (South Africa), P.1 (Brazil), B.1.427 (California), B.1.429 (California) and several other new variants of concerns (VOC) of SARS-CoV-2 around the world has the potential to jeopardize vaccine efficacy and the length of protection offered by these vaccines (5-11). The variants are also predicted to lead to an increase in transmission rates resulting in a snowball effect and further emergence of new variants (12-15). Moreover, deficiencies in the vaccine-roll out programs across different countries, vaccine hesitancy, optimal storage, technical errors and vaccine accessibility issues continue to jeopardize the required coverage necessary to obtain herd immunity. Here, I discuss some of our recent work related to engineering of relatively safe pseudoviruses that can be utilized for studying antibody responses as well as for screening of potential antivirals against SARS-C0V-2.

INTRODUCTION

The SARS-CoV-2 spike (S) glycoprotein, which mediates viral entry into the host cell by binding to human angiotensin-converting enzyme 2 (ACE2) and other accessory receptors, decorates the virus surface and determines critical events responsible for virus pathogenesis, including virus entry, spread into neighboring cells/tissues, as well as the majority of antibody responses against the virus. The spike protein is also the major candidate for the development of vaccines. It consists of two subunits, S1 and S2 where the receptor-binding domain (RBD) of the S1 subunit binds to ACE2 receptor on host cell membranes and the resultant exposure of fusion domain in S2 allows for viral entry (16). Mutations in S protein, including D614G and N501Y in the RBD, could plausibly increase the affinity of S towards ACE2 and increase virus transmission (13) as well as reduce the neutralizing activity of anti-S antibodies (17).

A pseudotype is a virus or a viral vector that displays the functional envelope glycoprotein of a heterologous virus, assembled into its outer wrapping, thus acquiring a new tropism (18). Pseudotyped particles have been used in virology for a long time to study highly pathogenic viruses that can only be handled in a biosafety level 3 or 4 (BSL3 or BSL4) laboratory such as Ebola virus and Marburg virus (18, 19). With the current advent of COVID-19 and the huge impact it has made on our daily lives, the development of pseudotyped particles coated with SARS-CoV-2 Spike glycoprotein has allowed for important studies on this virus in laboratories that do not have the facilities for BSL-3 or BSL-4 work. We initially pseudotyped a suicidal lentivirus (HIV) with SARS-CoV-2 spike protein and used this system to screen for neutralizing antibodies in convalescent patient serum to guide the clinicians whether the serum could be used for lifesaving transfusion in severely ill patients (20). These pseudotyped particles can be used in a BSL-2 laboratory since they consist of a replication defective HIV coated with SARS-COV-2 surface protein (Fig. 1). Other possible applications include drug inhibitor screening, vaccine studies and serological screening.

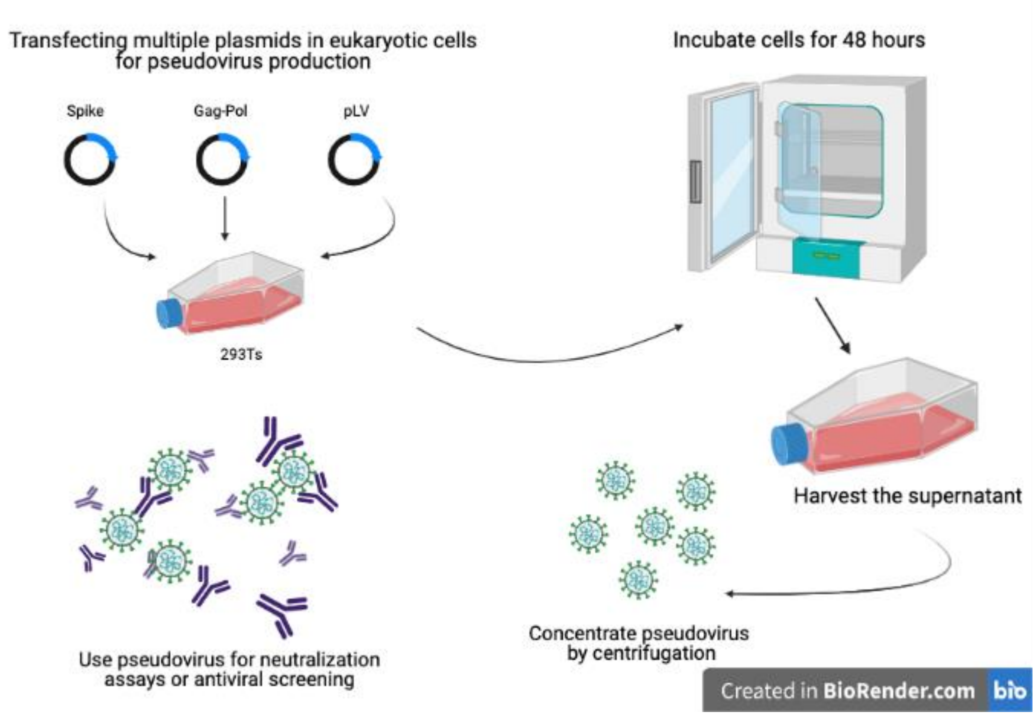

Fig. 1. Production of SARS-CoV-2 pseudovirus by transfecting plasmids encoding SARS-CoV-2 spike protein and the components of a lentivirus. The pseudovirus is harvested and used for neutralization assays as well as antiviral screening.

MATERIAL AND METHODS

The methodology to generate these pseudotyped particles has been published (20). Briefly, HEK293T cells are plated in a 100-mm tissue culture dishes and transfected the next day when they are about 75% confluent with a combination of the following plasmids: 9 µg of *pLV-eGFP* (a gift from Pantelis Tsoulfas (Addgene plasmid # 36083; http://n2t.net/ addgene:36083; RRID: Addgene _36083), 9 µg of *psPAX2* (a gift from Didier Trono (Addgene plasmid # 12260; http://n2t.net/ addgene:12260; RRID: Addgene _12260), and 3 µg of *pCAGGS-S (SARS-CoV-2)*(Catalog No. NR-52310: BEI Resources) or VSV-G (a gift from Tannishtha Reya (Addgene plasmid # 14888; http://n2t.net/addgene:14888; RRID:Addgene_14888) as control.

Polyethylenimine (PEI) reagent (Millipore Sigma, #408727) was used for transfection following manufacturer's protocols. Next day, the cells were checked for transfection efficiency under a fluorescent microscope, indicated by fluorescence generated from the integrated green fluorescent protein (GFP) in the lentivirus vector. The supernatants from cell culture at 24 h were harvested and stored at 4 °C and more (10 ml) complete media (DMEM + 10% FBS) was added to the plates. The supernatant from cell culture at 48 h was harvested and combined with the 24 h supernatant for each sample.

The combined supernatants were spun in a tabletop centrifuge for 5 min at 2000 g to pellet the residual cells and then passed through a 0.45 micron syringe filter. Aliquots were frozen at -80 °C. New 293T cells plated in 12 well tissue culture dish were infected with the harvested virus (supernatant) with a dilution range of 10^2 to 10^7. Virus titers were calculated by counting the GFP positive cells in the dilution with 20-100 GFP positive cells.

These particles have been useful not only in determining the titers of neutralizing antibodies in COVID-19 patient serum at the University of Mississippi Medical Center (20) but have helped tremendously with the screening of antivirals (21-23). They have also been utilized to test a novel and extremely sensitive virus detection method based on conjugated nanoparticles (24). In summary, the age old virology technique of pseudotyping that was developed to study virus tropism and entry has accelerated the research on a newly emerged virus and also helped clinical management and drug discovery in a time when the humankind is facing one of the biggest challenges of the 21st century.

REFERENCES

1. Polack FP, Thomas SJ, Kitchin N, Absalon J, Gurtman A, Lockhart S, Perez JL, Perez Marc G, Moreira ED, Zerbini C, Bailey R, Swanson KA, Roychoudhury S, Koury K, Li P, Kalina WV, Cooper D, Frenck RW, Jr., Hammitt LL, Tureci O, Nell H, Schaefer A, Unal S, Tresnan DB, Mather S, Dormitzer PR, Sahin U, Jansen KU, Gruber WC, Group CCT. 2020. Safety and Efficacy of the BNT162b2 mRNA Covid-19 Vaccine. N Engl J Med 383:2603-2615.
2. Baden LR, El Sahly HM, Essink B, Kotloff K, Frey S, Novak R, Diemert D, Spector SA, Rouphael N, Creech CB, McGettigan J, Khetan S, Segall N, Solis J, Brosz A, Fierro C, Schwartz H, Neuzil K, Corey L, Gilbert P, Janes H, Follmann D, Marovich M, Mascola J, Polakowski L, Ledgerwood J, Graham BS, Bennett H, Pajon R, Knightly C, Leav B, Deng W, Zhou H, Han S, Ivarsson M, Miller J, Zaks T, Group CS. 2021. Efficacy and Safety of the mRNA-1273 SARS-CoV-2 Vaccine. N Engl J Med 384:403-416.
3. Sadoff J, Le Gars M, Shukarev G, Heerwegh D, Truyers C, de Groot AM, Stoop J, Tete S, Van Damme W, Leroux-Roels I, Berghmans PJ, Kimmel M, Van Damme P, de Hoon J, Smith W, Stephenson KE, De Rosa SC, Cohen KW, McElrath MJ, Cormier E, Scheper G, Barouch DH, Hendriks J, Struyf F, Douoguih M, Van Hoof J, Schuitemaker H. 2021. Interim Results of a Phase 1-2a Trial of Ad26.COV2.S Covid-19 Vaccine. N Engl J Med doi:10.1056/NEJMoa2034201.
4. Knoll MD, Wonodi C. 2021. Oxford-AstraZeneca COVID-19 vaccine efficacy. Lancet 397:72-74.
5. Korber B, Fischer WM, Gnanakaran S, Yoon H, Theiler J, Abfalterer W, Hengartner N, Giorgi EE, Bhattacharya T, Foley B, Hastie KM, Parker MD, Partridge DG, Evans CM, Freeman TM, de Silva TI, Sheffield C-GG, McDanal C, Perez LG, Tang H, Moon-Walker A, Whelan SP, LaBranche CC, Saphire EO, Montefiori DC. 2020. Tracking Changes in SARS-CoV-2 Spike: Evidence that D614G Increases Infectivity of the COVID-19 Virus. Cell 182:812-827 e19.
6. Arif TB. 2021. The 501.V2 and B.1.1.7 variants of coronavirus disease 2019 (COVID-19): A new time-bomb in the making? Infect Control Hosp Epidemiol doi:10.1017/ice.2020.1434:1-2.
7. Duong D. 2021. What's important to know about the new COVID-19 variants? CMAJ 193:E141-E142.
8. Tang JW, Toovey OTR, Harvey KN, Hui DDS. 2021. Introduction of the South African SARS-CoV-2 variant 501Y.V2 into the UK. J Infect 82:e8-e10.
9. Annavajhala MK, Mohri H, Zucker JE, Sheng Z, Wang P, Gomez-Simmonds A, Ho DD, Uhlemann AC. 2021. A Novel SARS-CoV-2 Variant of Concern, B.1.526, Identified in New York. medRxiv doi:10.1101/2021.02.23.21252259.
10. Grubaugh ND, Hodcroft EB, Fauver JR, Phelan AL, Cevik M. 2021. Public health actions to control new SARS-CoV-2 variants. Cell 184:1127-1132.
11. Zhou D, Dejnirattisai W, Supasa P, Liu C, Mentzer AJ, Ginn HM, Zhao Y, Duyvesteyn HME, Tuekprakhon A, Nutalai R, Wang B, Paesen GC, Lopez-Camacho C, Slon-Campos J, Hallis B, Coombes N, Bewley K, Charlton S, Walter TS, Skelly D, Lumley SF, Dold C, Levin R, Dong T, Pollard AJ, Knight JC, Crook D, Lambe T, Clutterbuck E, Bibi S, Flaxman A, Bittaye M, Belij-Rammerstorfer S, Gilbert S, James W, Carroll MW, Klenerman P, Barnes E, Dunachie SJ, Fry EE, Mongkolsapaya J, Ren J, Stuart DI, Screaton GR. 2021. Evidence of escape of SARS-CoV-2 variant B.1.351 from natural and vaccine-induced sera. Cell doi:10.1016/ j.cell.2021.02.037.
12. Hou YJ, Chiba S, Halfmann P, Ehre C, Kuroda M, Dinnon KH, 3rd, Leist SR, Schafer A, Nakajima N, Takahashi K, Lee RE, Mascenik TM, Edwards CE, Tse LV, Boucher RC, Randell SH, Suzuki T, Gralinski LE, Kawaoka Y, Baric RS. 2020. SARS-CoV-2 D614G Variant Exhibits Enhanced Replication ex vivo and Earlier Transmission in vivo. bioRxiv doi:10.1101/2020.09.28.317685.
13. Liu Y, Liu J, Plante KS, Plante JA, Xie X, Zhang X, Ku Z, An Z, Scharton D, Schindewolf C, Menachery VD, Shi PY, Weaver SC. 2021. The N501Y spike substitution enhances SARS-CoV-2

transmission. bioRxiv doi:10.1101/2021.03.08.434499.

14. Hodcroft EB, Zuber M, Nadeau S, Crawford KHD, Bloom JD, Veesler D, Vaughan TG, Comas I, Candelas FG, Stadler T, Neher RA. 2020. Emergence and spread of a SARS-CoV-2 variant through Europe in the summer of 2020. med Rxiv doi:10.1101/2020.10.25.20219063.

15. Hou YJ, Chiba S, Halfmann P, Ehre C, Kuroda M, Dinnon KH, 3rd, Leist SR, Schafer A, Nakajima N, Takahashi K, Lee RE, Mascenik TM, Graham R, Edwards CE, Tse LV, Okuda K, Markmann AJ, Bartelt L, de Silva A, Margolis DM, Boucher RC, Randell SH, Suzuki T, Gralinski LE, Kawaoka Y, Baric RS. 2020. SARS-CoV-2 D614G variant exhibits efficient replication ex vivo and transmission in vivo. Science 370:1464-1468.

16. Hoffmann M, Kleine-Weber H, Schroeder S, Kruger N, Herrler T, Erichsen S, Schiergens TS, Herrler G, Wu NH, Nitsche A, Muller MA, Drosten C, Pohlmann S. 2020. SARS-CoV-2 Cell Entry Depends on ACE2 and TMPRSS2 and Is Blocked by a Clinically Proven Protease Inhibitor. Cell 181:271-280 e8.

17. Weisblum Y, Schmidt F, Zhang F, DaSilva J, Poston D, Lorenzi JC, Muecksch F, Rutkowska M, Hoffmann HH, Michailidis E, Gaebler C, Agudelo M, Cho A, Wang Z, Gazumyan A, Cipolla M, Luchsinger L, Hillyer CD, Caskey M, Robbiani DF, Rice CM, Nussenzweig MC, Hatziioannou T, Bieniasz PD. 2020. Escape from neutralizing antibodies by SARS-CoV-2 spike protein variants. Elife 9.

18. Salata C, Calistri A, Alvisi G, Celestino M, Parolin C, Palu G. 2019. Ebola Virus Entry: From Molecular Characterization to Drug Discovery. Viruses 11.

19. Chen Q, Tang K, Zhang X, Chen P, Guo Y. 2018. Establishment of pseudovirus infection mouse models for in vivo pharmacodynamics evaluation of filovirus entry inhibitors. Acta Pharm Sin B 8:200-208.

20. Tandon R, Mitra D, Sharma P, McCandless MG, Stray SJ, Bates JT, Marshall GD. 2020. Effective screening of SARS-CoV-2 neutralizing antibodies in patient serum using lentivirus particles pseudotyped with SARS-CoV-2 spike glycoprotein. Sci Rep 10:19076.

21. Tandon R, Sharp JS, Zhang F, Pomin VH, Ashpole NM, Mitra D, McCandless MG, Jin W, Liu H, Sharma P, Linhardt RJ. 2021. Effective Inhibition of SARS-CoV-2 Entry by Heparin and Enoxaparin Derivatives. J Virol 95.

22. Jin W, Zhang W, Mitra D, McCandless MG, Sharma P, Tandon R, Zhang F, Linhardt RJ. 2020. The structure-activity relationship of the interactions of SARS-CoV-2 spike glycoproteins with glucuronomannan and sulfated galactofucan from Saccharina japonica. Int J Biol Macromol 163:1649-1658.

23. Yan L, Song Y, Xia K, He P, Zhang F, Chen S, Pouliot R, Weiss DJ, Tandon R, Bates JT, Ederer DR, Mitra D, Sharma P, Davis A, Linhardt RJ. 2021. Heparan sulfates from bat and human lung and their binding to the spike protein of SARS-CoV-2 virus. Carbohydr Polym 260:117797.

24. Pramanik A, Gao Y, Patibandla S, Mitra D, McCandless MG, Fassero LA, Gates K, Tandon R, Ray PC. 2021. Aptamer Conjugated Gold Nanostar-Based Distance-Dependent Nanoparticle Surface Energy Transfer Spectroscopy for Ultrasensitive Detection and Inactivation of Corona Virus. J Phys Chem Lett 12:2166-2171.

Author Guidelines

Editorial Policy. The Editorial Board publishes articles on all aspects of science that are of general interest to the scientific community. General articles include short reviews of general interest, reports of recent advances in a particular area of science, current events of interest to researchers and science educators, etc. Research papers of sufficiently broad scope to be of interest to most Academy members are also considered. Articles of particular interest in Mississippi are especially encouraged.

Research papers are reports of original research. Submission of a manuscript implies that the paper has not been published and is currently at the time of submission being considered for publication elsewhere. At least one of the authors must be a member of the Academy, and all authors are encouraged to join.

Manuscripts. Submit the manuscript electronically to the Mississippi Academy of Sciences under your profile in the member location of the website. Please also provide a cover letter to the Editor of the Journal. The cover letter should authorize publication: give the full names, contact information, for all authors; and indicate to whom the proofs and correspondence should be sent. Please notify the Editor on any changes prior to publication.

Manuscripts must adhere to the following format:

- One inch margins on 8.5 x 11 inch paper;
- Text should be left-justified using twelve point type;
- Double spaced throughout, including the title and abstract;
- Arabic numerals should be used in preference to words when the number designates anything that can be counted or measured (7 samples, 43 species) with 2 exceptions:
- To begin a sentence (Twenty-one species were found in…)
- When 2 numeric expressions are adjacent in a sentence. The number easiest to express in words should be spelled out and the other left in numeric form (The sections were divided into eight 4-acre plots.).
- Measurements and physical symbols or units shall follow the International System of Units (SI *Le Système international d'unités*) with metric units stated first, optionally followed by United States units in parentheses. *E.g.*: xx grams (xx ounces); and
- Avoid personal pronouns.

Format

Abstract. In 500 or fewer words summarize any new methods or procedures critical to the results of the study and state the results and conclusions.

Introduction. Describe the knowledge and literature that gave rise to the question examined by, or the hypothesis posed for the research.

Materials and methods. This section should describe the research design, the methods and materials used in the research (subjects, their selection, equipment, laboratory or field procedures), and how the findings were analyzed.

Results. The text of the results should be a descriptive narrative of the main findings, of the reported study. This section should not list tabulated data in text form. Reference to tables and figures included in this section should be made parenthetically in the text.

Discussion. In this section compare and contrast the data collected in the study with that previously reported in the literature. Unless there are specific reasons to combine the two, as explained by the author in the letter of transmittal, Results and Discussion should be two separate sections.

Acknowledgments. Colleagues and/or sources of financial support to whom thanks are due for assistance rendered in completion of the research or preparation of the manuscript should be recognized in this section rather than in the body of the text.

Literature cited. List references alphabetically. Cite references in the text by author and year of publication (e.g., Smith, 1975; Black and Benghuzzi, 2011; Smith et al., 2010; Smith, 2011a, 2011b). The following examples illustrate the style to be used in the literature list.

Black DA, Lindley S, Tucci M, Lawyer T, Benghuzzi H. A new model for the repair of the Achilles tendon in the rat. J Invest Surg. 2011; 24(5): 217-221.

Pearson HA, Sahukhal GS, **Elasri** MO, Urban MW. Phage-bacterium war on polymeric surfaces: can surface-anchored bacteriophages eliminate microbial infections? Biomacromolecules. 2013 May 13;14(5):1257-61.

Bold, H.C., C.J. Alexopoulos, and T. Delevoryas. 1980. Morpholgy of plants and fungi, 4th ed. Harper and Row, New York. 819 pp

Web-page

- name of author(s) -if known
- title of the work - in quotes, if known
- title of the Web page - in italics, if applicable
- date of last revision
- URL
- Date accessed

Example:

Ackermann, Ernest. "Writing Your Own Web Pages." *Creating Web Pages.* 23 Oct. 1996. http://people.umw.edu/~ernie/writeweb/writeweb.html 10 Feb. 1997.

File available by anonymous FTP

- name of author(s) -if known
- title of the work - in quotes, if known
- date of last revision
- URL
- Date accessed

Example:
American Civil Liberties Union. "Briefing paper Number 5, Drug Testing in the Work Place." 19 Nov. 1992. ftp://ftp.eff.org/pub/Privacy/Medical/aclu_drug_testing_workplace.faq
13 Feb. 1997.

Please Tables and Figures at the end of the manuscript submitted.

Tables. Tables must be typed double spaced, one table to a page, numbered consecutively, and placed at the end of the manuscript. Since tables must be individually typeset, consolidation of data into the smallest number of tables is encouraged. A horizontal double underline should be made beneath the title of the table, and single underlines should be made the width of the table below the column headings and at the bottom of the table. Do not use vertical lines, and do not place horizontal lines in the interior of the table. Use footnotes, to clarify possible questions within the table, should be noted by asterisks, daggers, or other symbols to avoid confusion with numerical data. Tables should be referred to parenthetically in the text, for example (Table 1).

Figures and illustrations. Figures may be photographs, computer -generated drawings, or graphs and should be placed at the end of the manuscript and referenced in the appropriate place. All illustrations are referred to as "Figures" and must be numbered consecutively. Illustrations other than those generated by the author(s) must include permission for use and credit to the originator. Each figure must have a complete legend that is typed, double-spaced, on a separate sheet which precedes the figures in the manuscript. Figures should be referred to parenthetically in the text, for example (Fig. 1).

Footnotes. Text footnotes **should not be used**

Submission Preparation Checklist

As part of the submission process, authors are required to check off their submission's compliance with all of the following items, and submissions may be returned to authors that do not adhere to these guidelines.

1. The submission has not been previously published, nor is it before another journal for consideration (or an explanation has been provided in Comments to the Editor).
2. The text adheres to the stylistic and bibliographic requirements outlined in the Author Guidelines.
3. I acknowledge that if my manuscript is peer-reviewed and accepted for publication, there will be a paper charge fee of $150.00
4. The manuscript file is in Microsoft Word format.

Copyright Notice

Authors who publish with this journal agree to the following terms:

1. Authors retain copyright and grant the journal right of first publication
2. Authors are able to enter into separate, additional contractual arrangements for the non-exclusive distribution of the journal's published version of the work (e.g., post it to an institutional repository or publish it in a book), with an acknowledgement of its initial publication in this journal.
3. Authors are permitted and encouraged to post their work online (e.g., in institutional repositories or on their website) prior to and during the submission process, as it can lead to productive exchanges, as well as earlier and greater citation of published work.

Mississippi Academy of Sciences
Post Office Box 55907
Jackson, MS 39296-5907

Nonprofit Organization
U. S. Postage
PAID
Jackson, MS
39216
Permit No. 305

Coden: JMSS-A **ISSN 0076-9436**

Volume 67, Number 1 January 2022